Elucidation of Functional Roles of Heme-Propionate Side Chains in Hemoproteins

2008

Katsuyoshi Harada

Department of Applied Chemistry
Graduate School of Engineering
Osaka University

Elucidation of Functional Roles of Heme-Propionate Side Chains in Hemoproteins

(ヘム蛋白質におけるヘムプロピオン酸側鎖の機能的役割解明)

2008

Katsuyoshi Harada

Department of Applied Chemistry
Graduate School of Engineering
Osaka University

Contents

General Introduction

Heme–protein interactions

Hemoproteins have an iron-protoporphyrin complex (heme) in the active site of the proteins and these functions are widespread [1]. The functions contain reversible dioxygen binding (myoglobin, hemoglobin), oxidation (peroxidase, catalase, chloroperoxidase) and reduction (nitric oxide reductase) reactions, electron transfer (cytochromes), gas molecule sensing (CooA, HemAT), metabolism of dioxygen utilizing the redox reactions (cytochrome *c* oxidase), NO synthesis (nitric oxide synthase) and oxygenation reactions (cytochrome P450) [2]. Almost all hemoproteins have the similar prosthetic group, that is iron-protoporphyrin complex, but their functions are quite different. The main reason why the functions of hemoproteins are quite different though they have the same heme in their active sites is the difference of interactions between heme and protein matrix. The interactions between heme and protein matrix (Figure 1) are (i) the coordination of amino acid residues, such as His, Tyr, Cys, and Met to the heme iron, (ii) aromatic π-stacking between porphyrin and aromatic amino acid residues, such as Trp, Tyr, and Phe, (iii) hydrophobic interaction between porphyrin side chains such as methyl or vinyl group and aliphatic amino acid residues, such as Leu, Ile, and Val, (iv) CH-π interaction between porphyrin side chain or porphyrin ring and aromatic or aliphatic amino acid residues, (v) electrostatic or hydrogen bonding interactions between heme propionate side chains and basic amino acid residues, such as Arg, Lys, and His [3]. It is thought that the protein structures and the interactions between protein matrix and heme govern the functions of hemoproteins. Thus, the investigation on the structure-function relationship of hemoprotein is important to understand the nature of protein functions.

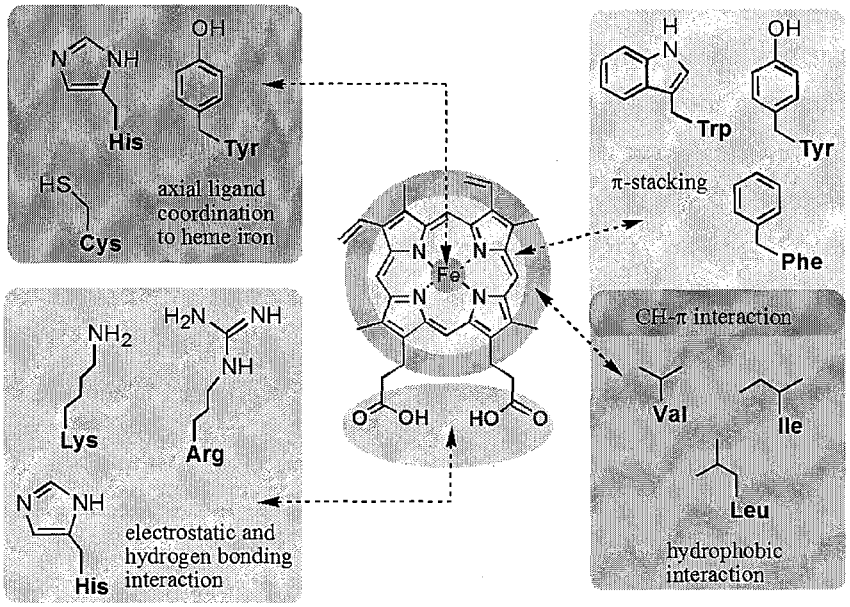

Figure 1. Heme–protein interactions in hemoproteins.

Strategy of the elucidation of role of heme–protein interactions

Heme is bound by noncovalent interactions with several amino acid residues in the protein matrix and the interactions are thought to have a significant influence on the hemoprotein functions. Therefore, it will become to be possible to evaluate the protein functions logically by investigating a number of interactions between heme and protein matrix in details. The strategy of the elucidation of role of heme–protein interactions is divided into at least two methods. One is the mutagenesis approach, and the other is the replacement of native heme with an artificial prosthetic group as shown in Figure 2. Over two decades, by the genetic engineering, there have been many mutants whose amino acid residues in the active site are selectively replaced with the other amino acids, in order to compare with that of the native protein. The technique has been a general method to elucidate the direct role of each amino acid on the functional roles of proteins.

On the other hand, there are a few researches on the heme–amino acid interactions from the view point of the heme. The heme prosthetic group of *b*-type (protoheme IX containing) hemoprotein, such as myoglobin and cytochrome P450cam, are attached to the protein matrix with several noncovalent heme–protein interactions and can be easily removed from the protein matrix. By introducing an artificially created prosthetic group into the heme pocket, we might compare the function of the hemoproteins.

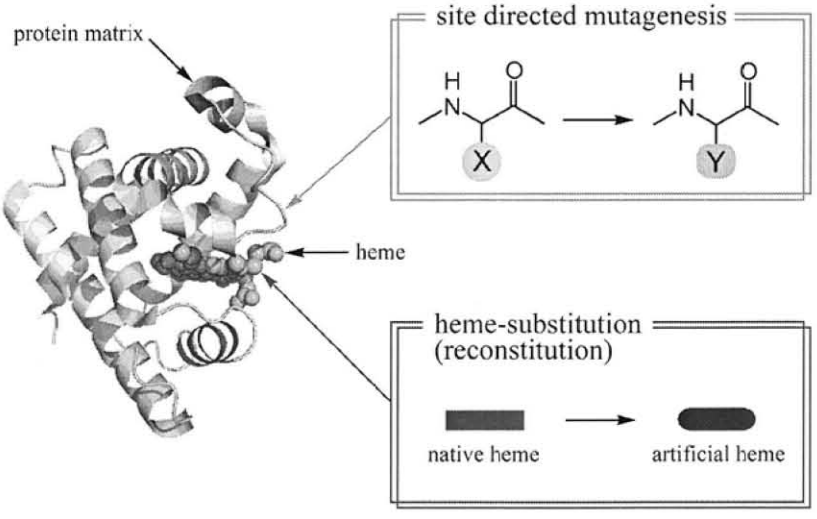

Figure 2. Strategy of evaluation of heme–protein interactions.

Myoglobin

Myoglobin is a well known hemoprotein which contains a protoporphyrin IX iron complex (protoheme IX) and a globular shaped protein which consists of eight α-helices (Figure 3) [4]. The function of myoglobin in biosphere is storage of dioxygen by picking up oxygen from the blood and passing it through muscle tissue to mitochondria. The dioxygen binds reversibly to the prosthetic heme iron which is in the state of ferrous heme. The heme is wedged between E and F helices by Fe–His (His93 (F9)) coordination, hydrophobic contact of the heme with several nonpolar aliphatic and aromatic amino acid residues, and the formation of a salt bridge between the heme propionate side chains and polar amino acid residues.

Since the 3D structures of myoglobin have been available, the important amino acid residues on the function of myoglobin have been discussed mainly by mutagenesis technique [5]. The His64 (E7) above the heme iron is crucial residue for the binding of dioxygen. The mutant of which His64 is replaced with Gln has the O_2 affinity of one tenth compared with that of the native myoglobin [6]. Furthermore, the mutant of which His64 is replaced with nonpolar residues such as Gly, Val, Leu, Met, or Phe shows the extremely lower O_2 affinity (1/100 ~ 1/1000 fold). Given that both of His and Gln have ability of hydrogen bonding donor and acceptor and other nonpolar residues don't have the ability, the hydrogen bonding between the residue 64 and the bound dioxygen is important for the stability of the oxymyoglobin. Thus, the dioxygen bound to the heme iron is hydrogen bonded to His64 and is maintained in the protein matrix stably.

The hydrophobic residues, such as Leu29 and Val68, in the heme distal site are important for inhibiting the autoxidation from the oxymyoglobin to metmyoglobin [7], which is incapable of binding oxygen and thus physiologically inactive. Olson et al. examined the effects of distal pocket size on the autoxidation reaction by preparing mutants of which Val68 was replaced with Ala, Ile, Leu, and Phe and Leu29 was replaced with Ala, Val and Phe in sperm whale myoglobin. An increase in the volume of the distal site due to the V68A substitution could increase the accessibility of water and other solvent nucleophiles to the iron atom. Moreover, the native 68 residue orients the dioxygen ligand for more efficient hydrogen bonding to His64. L29A mutant also showed increased autoxidation rate because of an increase in the size of the distal pocket and its accessibility to solvent. On the other hand, L29F mutant showed higher affinity toward dioxygen relative to the native protein because of inhibition of solvent access into the distal site and a direct interaction between the partially positive edge of the phenyl ring and the partial negative charge on the second atom of the bound dioxygen [8].

The presence of a proximal ligand has a critical influence of the reactivity of the heme iron. In the absence of a proximal fifth ligand, the equilibrium constant for CO binding is reduced several hundred-fold and reversible oxygen binding does not occur due to extremely rapid rates of autoxidation. The CO and O_2 affinity of myoglobin could be affected by the restraints on the proximal histidine bond and Fe deviation relative to the plane of the porphyrin ring [5]. The residues, Leu89, His97, Ile99, and Leu104 located on the proximal side of the heme pocket strongly influence the heme affinity and prevent hydration of the Fe–His93 bond by forming a barrier toward solvent penetration, minimizing the size of the proximal cavity, and maintaining a hydrophobic environment [9].

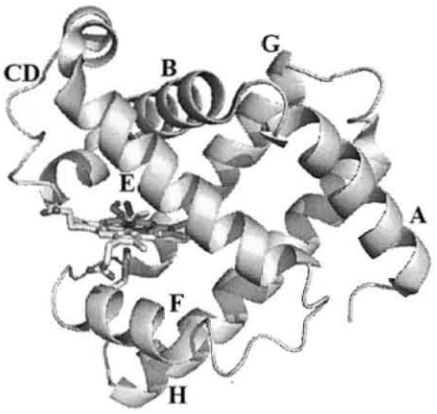

Figure 3. 3D structure of sperm whale myoglobin (PDB ID: 1MBO).

The interactions between heme-propionate side chains and protein matrix in myoglobin

Heme *b* has two propionate side chains at 6- and 7- positions and the two propionates in myoglobin interact with surrounding amino acid residues. The 6-propionate side chain in myoglobin interacts with Arg45 and the 7-propionate side chain interacts with Ser92 and His97, respectively. It is generally thought that two heme propionate side chains may be only anchors to fix the heme stably in the protein matrix. However, 6-propionate side chain in myoglobin constructs hydrogen bonding network with His64 which is essential amino acid for ligand binding property of myoglobin via Arg45 and water molecules as shown in Figure 4 [10]. In contrast, 7-propionate side chain of myoglobin participates in forming hydrogen bonding network with His93 which is a fifth ligand of heme via Ser92 (Figure 4). These hydrogen bonding networks seem to be essential to regulate the myoglobin function because the former network stabilizes the bound-O_2 and the latter may control the position of the imidazole ring as an axial ligand of His93. Thus, heme propionate side chains are expected to regulate the ligand binding property of myoglobin. Although it is unambiguous that each heme-propionate side chain is a part of the hydrogen bonding network, their contribution to the myoglobin function has not been completely determined.

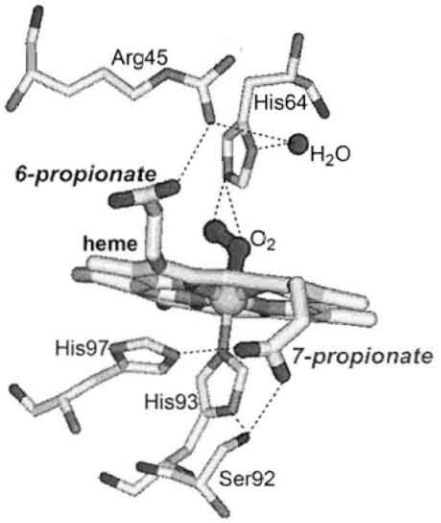

Figure 4. Hydrogen bonding network involving heme propionate side chains in sperm whale oxymyoglobin (PDB ID: 1MBO).

Elucidation of roles of heme-propionate side chains in myoglobin

Several research groups have devoted their efforts to evaluation of the role of the propionate–globin interaction to the protein function by a mutagenetic approach, in which the propionate-bound amino acid residues, such as Arg45 and Ser92, are replaced with a different type residue (Figure 5). For example, residue 45 is substituted with noncharged residues, such as Ser or Gly [11, 12]. The 3D structure of the aquomet K45S mutant for pig myoglobin reveals that the mutation produces only a small deviation in the α-carbon main chain from that of the native protein, but a more open pocket structure compared to the native myoglobin, although a significant change in the kinetic parameters for O_2 or CO binding has not been observed for these mutants. On the other hand, the replacement of Ser92 with Val or Leu for the pig myoglobin increased the ligand binding affinities, indicating that the removal of the Ser92–His93 hydrogen bond activates the heme iron for the ligand binding [13], whereas the S92A mutants for human and pig myoglobin showed approximately the same kinetic parameters with the corresponding native myoglobin [13, 14]. Furthermore, several groups have reported the structural data of position 92 mutants to elucidate the contribution of Ser92 to the myoglobin function [13−15]. However, it is still not clarified that the real role of the interaction between the 7-propionate and Ser92 has an influence on ligand binding. The mutation of Arg45 or Ser92 is an indirect method to elucidate the role of heme propionate.

Another strategy for evaluating the role of the two heme propionate side chains in ligand binding in myoglobin will be the removal of one of the propionates by chemical modification. Although a simple idea is the esterification of one of the heme propionate side chains to disrupt the hydrogen bonding network, it is difficult to selectively prepare the hemin monoester at the position 6 or 7 side chain by organic synthesis [11, 16]. Olson et al. reported the reconstituted myoglobin with hemin dimethylester, but they couldn't elucidate each role of heme propionate side chain.

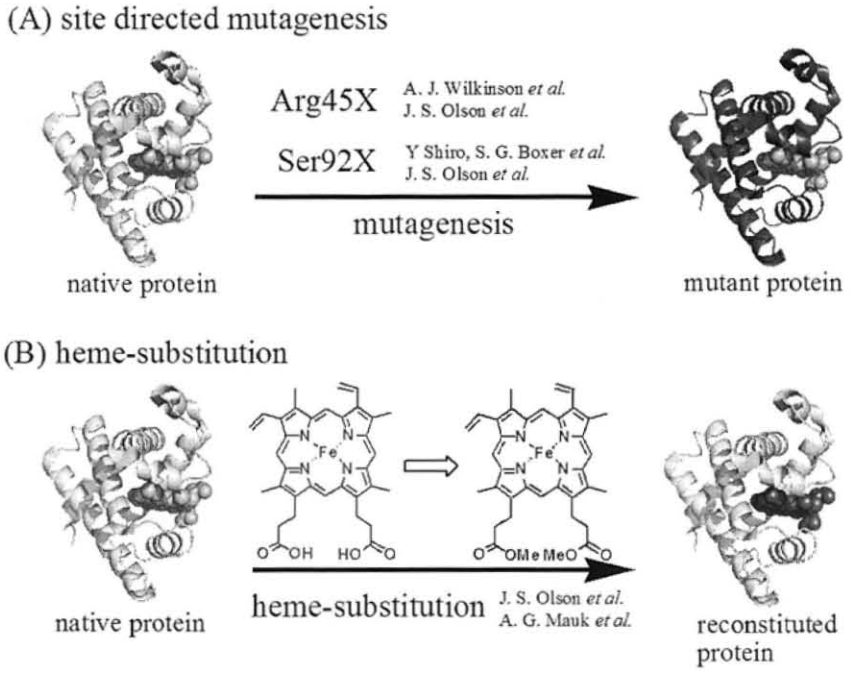

Figure 5. Previous reports to elucidate the roles of heme-propionate side chains in sperm whale myoglobin.

To overcome this problem, Hayashi et al. first prepared two "one-legged" mesohemin derivatives in which the 6- or 7-propionate side chain was replaced with a methyl group and then inserted them into the apomyoglobin [17]. The two proteins reconstituted with each mesoheme derivative exhibited kinetic parameters for ligand binding events different from those observed by the native protein. However, these reconstituted myoglobins were not appropriate for the exact evaluation of the role of each propionate side chain on the basis of the kinetic studies, because there are two heme orientations, forward and backward, in the asymmetric heme pocket with the ratio of 4–8. In contrast, La Mar, Smith, and their coworkers reported that two myoglobins, rMb(**1**) and rMb(**2**), reconstituted with the prototype one-legged protohemins, **1** and **2**, respectively, as shown in Figure 6, mainly give the forward hemin plane conformation in the heme pocket [18, 19]. According to their studies, the ratios of the forward and backward hemin planes in the sperm whale myoglobin were determined to be 20:1 and 18:1 for rMb(**1**) and rMb(**2**), respectively, by a ^{1}H NMR technique. Therefore, rMb(**1**) and rMb(**2**) will be suitable for understanding how each heme propionate influences the myoglobin function, although, to the best of the author's knowledge, the O_2 binding properties for rMb(**1**) and rMb(**2**) have never been reported in previous reports [20, 21].

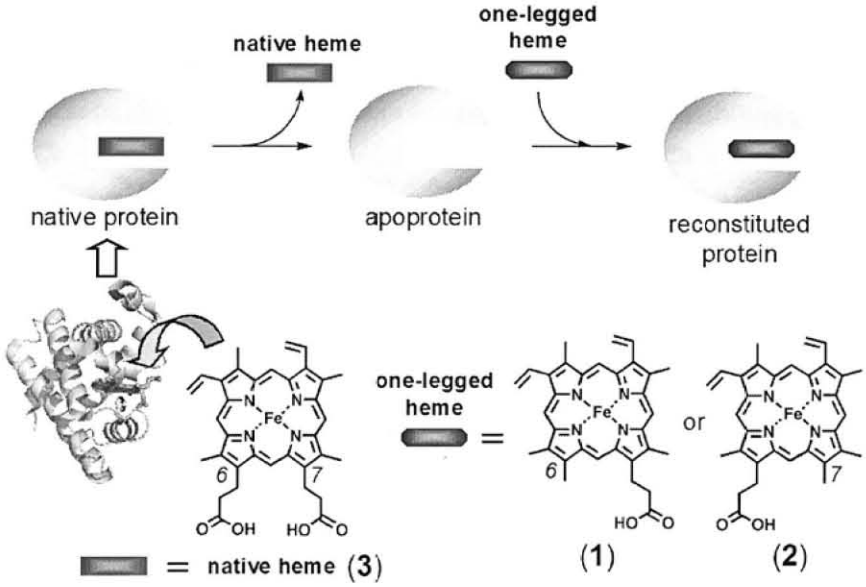

Figure 6. Reconstitution of myoglobin with one-legged hemes.

Cytochrome P450cam

Cytochrome P450 is a variety of hemoproteins in bacteria, fungi, plant, insect and vertebrate. The ferrous form of P450 binds carbonmonoxide (CO) and show the characteristic absorption centered around 450 nm. P450 enzymes are involved in numerous biological processes, biosynthesis of lipids, steroids, antibiotics, and the degradation of xenobiotics (Table 1). The P450 enzymes have been extensively examined in the field of medicine and pharmacy. Furthermore, the P450 family is involved in the biosynthesis of a variety of plant hormones in plants and the synthesis of hormones regulating metamorphosis and the expression of tolerance toward agricultural chemicals in insects. Therefore, they are also examining in the filed of agriculture. On the other hand, because P450 can catalyze regio- and stereo- selective hydroxylation of substrate under mild conditions such as normal temperature and pressure [22], it has been tried to apply its catalysis [23].

P450 species is ligated by thiolate of cysteine and its carbonmonoxide (CO) adduct shows characteristic absorption around 450 nm (Figure 7). On the other hand, P420 species which is the denatured state of P450 shows absorption around 420 nm when it binds CO. CO- ligated hemoglobin or myoglobin where the fifith ligand is imidazole of histidine also shows absorption maxima at 420 nm. It was proposed that the fifth ligand thiolate was replaced with imidazole of histidine or thiolate was protonated in P420 species. It is known that P420 species has no catalytic activity for substrate hydroxylation.

Table 1. Typical reactions catalyzed by cytochrome P450

hydroxylation	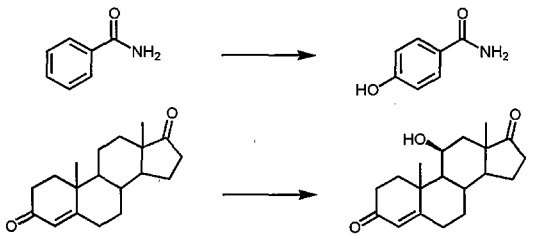
epoxidation	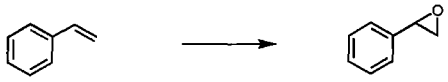
N-demethylation	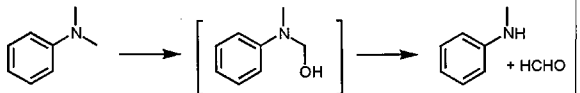
O-demethylation	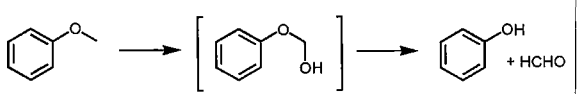
sulfoxidation	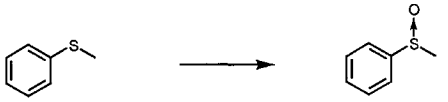
NO synthesis	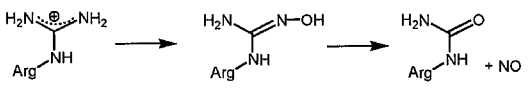

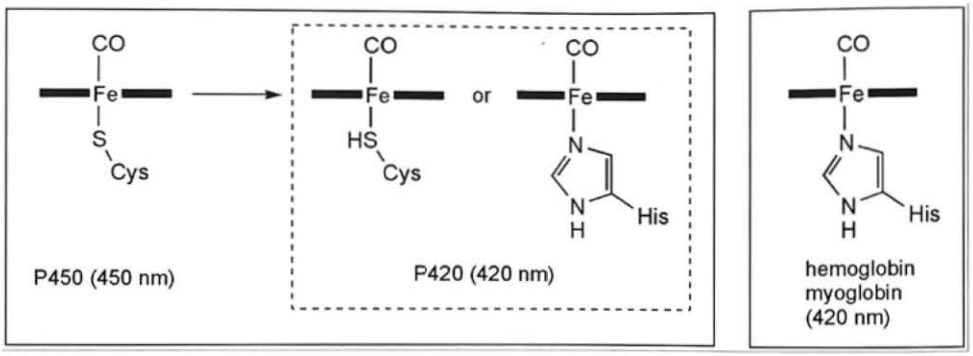

Figure 7. Heme ligation state of cytochrome P450, P420, hemoglobin, and myoglobin.

Poulos et al. reported the first X-ray crystal structure of a P450, the soluble bacterial cytochrome P450cam (Figure 8) [24]. The P450cam molecule consisting of 414 amino acid residues ($Mr \sim 45$ kDa) has a triangular shape with a side of 60 Å and a thickness of 30 Å including the active site heme plane nearly parallel to the plane of the triangle. The heme is deeply embedded in the hydrophobic interior with no significant exposure of the protein surface. The heme iron is ligated by the thiolate derived from Cys as a fifth ligand with the distance of 2.2−2.3 Å and the sulfur atom, the heme fifth ligand, was surrounding by the loop consisted of the amino acids continuing from the Cys to the side of C-terminus region. The three NH of main chains of the loop forms three hydrogen bondings with the sulfur atom and stabilize the Fe−S bond with the distances of 3.2−3.6 Å. The identity of the proximal heme iron ligand as a cysteine has been established based on earlier spectroscopic work by Dawson et al. [25]. Furthermore, it was confirmed that the specific cysteine was bound to heme iron by the crystal structure analysis reported by Poulos et al. [24]. The sixth ligand binding side is located opposite side of the fifth ligand relative to the heme plane, where various exogenous ligand (water molecule, gaseous molecule (O_2, CO, NO etc.), substrates, and inhibitors etc.) can be bound. The long I-helix exists above the heme binding side and the V-shaped F and G helices are above the I-helix.

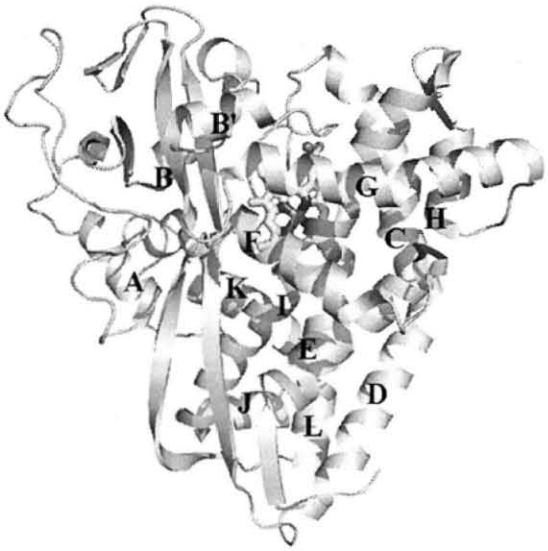

Figure 8. 3D structure of cytochrome P450cam (PDB ID: 2CPP).

Cytochrome P450cam catalyzes the stereo- and regio-specific hydroxylation of *d*-camphor at its 5-*exo* position (Scheme 1, Figure 9). The resting state of the enzyme is hexacoordinate low-spin ferric heme state with a coordinated water as a sixth ligand opposite to the proximal cysteine ligand. Substrate binding to the binding site of heme excludes the water molecule coordinated to heme iron leads to the generation of the pentacooridinated high-spin ferric heme state with a vacant coordination site which is available for dioxygen binding over the heme iron. The conversion of the ferric heme from low- to high-spin results in a significant increase of the redox potential of the heme iron from −330 to −170 mV (vs. NHE) [26]. This positive shift of the redox potential facilitates the electron transfer from reduced putidaredoxin (Pdx^{red}) ($E = -196$ mV vs. NHE [26(a)]), the redox partner of P450cam, to the ferric heme of P450cam. Subsequently, the first electron transfer occurs from Pdx to P450cam and the pentacoordinated high-spin ferrous P450cam is generated. The dioxygen molecule binds to the ferrous heme of P450cam to generate the oxygenated intermediate. The second electron from reduced Pdx reduces oxygenated enzyme to a ferric peroxy species. The protonation of the distal oxygen in the peroxo-iron complex produces a hydroperoxo species, and the subsequent protonation leads to heterolytic O–O cleavage releasing a water molecule to form the oxyferryl species. Oxygen atom transfer from an iron-oxo complex to the substrate, presumably by an oxygen rebound mechanism [27], yields the oxidized product and regenerates the resting state of enzyme. The electrons necessary to the reaction catalyzed by P450 is transferred from biological reducing agent, NADH, where its electrons are mediated by the biological redox partner putidaredoxin and putidaredoxin reductase [28]. Electrons from NADH are delivered to the putidaredoxin reductase, which contains a FAD (Flavine adenine dinucleotide) (Mr = 45.6 kDa). The putidaredoxin (Mr = 11.6 kDa), the [2Fe–2S] serves as a one-electron shuttle between NADH-dependent putidaredoxin reductase and the terminal oxygenase cytochrome P450cam.

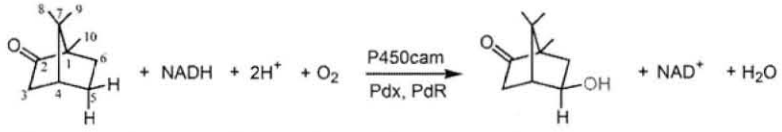

Scheme 1. Hydroxylation of *d*-camphor catalyzed by cytochrome P450cam.

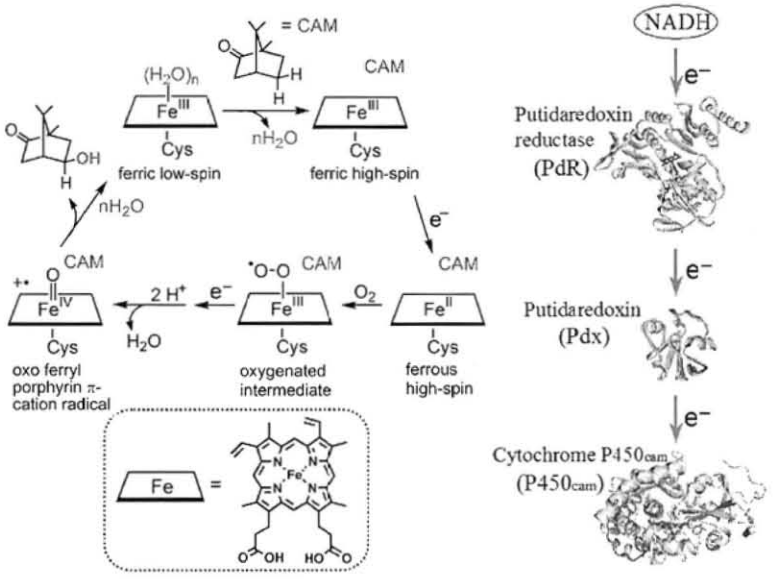

Figure 9. Catalytic cycle of *d*-camphor hydroxylation by P450cam.

The catalytic mechanism of the reaction by the cytochrome P450cam was mainly elucidated by site-directed mutagenesis technique. The heme-substitution methods have been applied to the researches on the cytochrome P450cam, too. Wagner et al. reported the ^{57}Fe- and ^{54}Fe-substituted heme were incorporated into the apoP450cam successfully and the reconstituted proteins retain enzymatic activities and regio- and stereo- specific hydroxylation ability, absorption spectra and EPR spectra compared to the native enzyme [29]. Therefore, it was confirmed that the heme-substitution method could be applicable to cytochrome P450cam as in the case of myoglobin. Wagner et al. also reported the cobalt-substituted cytochrome P450cam [30(a)]. The ESR measurements of the cobalt-substituted P450cam confirmed that in the ferrous cobaltous protein endogenous axial ligand other than a nitrogenous base and in the oxygenated cobaltous enzyme a thiolate ligand was indicated. By analogy, it was suggested that the native ferrous and oxygenated P450cam retains a thiolate axial ligand. Manganese- [30(b), 30(c)] and zinc- [30(d)] substituted cytochrome P450cam obtained by the reconstitutional method were also reported. Further, X-ray crystal structure of manganese-substituted P450cam has been reported [30(c)]. On the other hand, the incorporation of side chains substituted heme into apoP450cam is quite limited [31(a), 31(b)]. Makino et al. prepared diacetyl-, monoacetyl-, deutero-, and meso- heme substituted P450cam and examined the correlation between π-electron density and the catalytic activity [31(a)]. To the best of the author's knowledge, propionate side chain modified heme has never incorporated into apoP450cam. Therefore, it is thought that the incorporation of propionate side chain modified heme into apoP450cam is a challenging trial.

Elucidation of the roles of heme-propionate side chains in P450cam

The two propionates in the cytochrome P450cam interact with the surrounding amino acid residues as shown in Figure 10. It is generally thought that the two heme propionate side chains are anchors to fix heme stably in the protein matrix. The 6-propionate side chain interacts with Thr101, Gln108, Arg112 and His355. One of the features of P450cam is in the point that dioxygen is activated reductively by the binding of Pdx and electron flowing into the heme. There is still room to discuss which route electron is transferred to heme iron. It is thought that Arg112 is a Pdx binding site based on the fact that binding affinity of Pdx is decreased and electron transfer rate and catalytic reaction rate are decelerated remarkably in Arg112 mutant synthesized by site-mutagenesis. Arg112 in P450cam is one of the most conserved amino acid residues in the P450 family [32]. Arg112 is located in the molecular surface region of P450cam, and it is well known that Arg112 is essential in the electron transfer event from reduced putidaredoxin. According to the X-ray structure, Arg112 is hydrogen bonded with the heme-6-propionate side chain and the carbonyl oxygen of Leu356 which is neighbored to Cys357 ligated to heme iron [24(c)]. From the kinetic measurement using mutants at Arg112, it had been concluded that Arg112 is a major factor governing the affinity of putidaredoxin to the ferric and/or the oxy-P450cam and the electron transfer rate within the P450cam–putidaredoxin complex [33]. Furthermore, Lys mutant at a position of 112, which is basic amino acid similar to Arg, showed the similar enzymatic property with wild-type protein. Therefore,

it was concluded that positive charge was important on the role of Arg112 [33]. From these facts, it is hypothesized that the 6-propionate side chain participates in electron transfer event from Pdx to the heme of P450cam.

On the other hand, 7-propionate side chain of P450cam interacts with Asp297 and Arg299 (Figure 10). A theoretical study reported by Oprea et al. postulated that the water molecules in the substrate binding side could be expelled through a space transiently formed by a cleavage of the 7-propionate–Arg299 salt-bridge due to a metastable rotamer of the Arg299 residue [34], although any experimental evidences for the rotamer of Arg299 have never been provided and any investigations on the Arg299 or Asp297 mutants have never been reported.

To elucidate the role of heme propionate side chain in the cytochrome P450cam, the author prepared reconstituted P450cam with "one-legged heme" **1** or **2** and investigated their structures and reactivity.

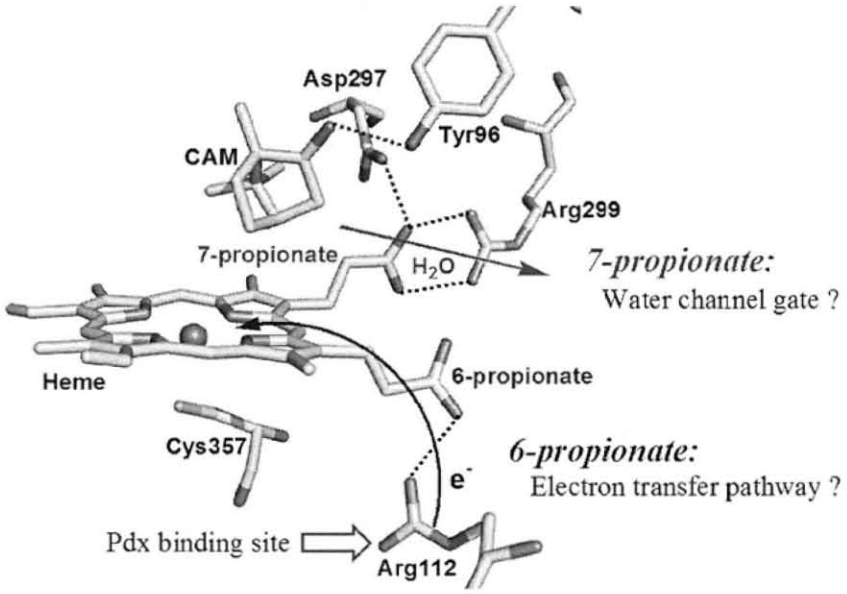

Figure 10. Proposed roles of each propionate side chain in P450cam.

One-legged hemes as probes for the elucidation of the roles of heme-propionate side chains in hemoprotein functions

The simple strategy to evaluate the role of each heme propionate side chains is the esterification of one of the heme propionate side chain to disrupt hydrogen bonding with the surrounding amino acid residues. However, it is difficult to selectively isolate the heme monoesters at the position 6 or 7 side chain even if they could be generated by organic synthesis. Even when the heme where both propionic groups were methylesterized could be inserted into apoproteins, it is impossible to define which propionate would contribute the function.

The one-legged hemes, 6-depropionated-6-methylated protoheme IX and 7-depropionated-7-methylated protoheme IX (Iron(III)-7-(2-carboxyethyl)-1,3,5,6,8-pentamethyl-2,4-divinylporphyrin and Iron(III) -6-(2-carboxylethyl)-1,3,5,7,8-pentamethyl-2,4-divinylporphyrin, respectively) had been first synthesized previously by K. M. Smith et al. [35]. K. M. Smith, G. N. La Mar and their coworkers inserted these hemes into apomyoglobin to investigate the structural properties, electronic structure and the orientation of heme in the protein matrix of myoglobin by utilizing NMR spectroscopic techniques [18, 36] and circular dichroism [19]. However, they didn't focus on the role of heme propionate side chains in myoglobin function, that is, ligand binding properties.

In this thesis, the author will focus on the structure-function relationship of hemoproteins and wish to elucidate the role of heme propionate side chain in ligand binding function of myoglobin. Further, the author will discuss the role of heme propionate side chains in cytochrome P450cam enzymatic function. The author believes that the one-legged hemes are exact probes for elucidating the functional roles of heme propionate side chains in hemoproteins, myoglobin and cytochrome P450cam.

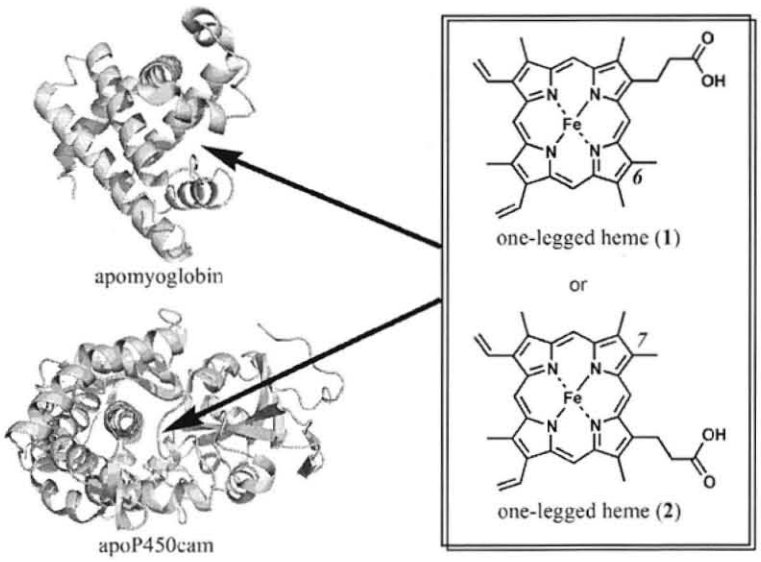

Figure 11. Reconstitution of myoglobin and cytochrome P450cam with one-legged heme (**1**) and (**2**).

Outline of This Thesis

Chapter 1

The binding behavior of the two heme propionate side chains in the sperm whale myoglobins was evaluated using artificially created hemins, 6-depropionated-6-methylated- and 7-depropionated-7-methylated -protohemin IX. From the thermodynamic study of the hemin binding to apomyoglobin, it was found that the two heme propionates clearly contribute to the stabilization of the hemin in the protein matrix. Furthermore, the synthetic routes of one-legged hemins are also described in this chapter.

Chapter 2

The two heme propionate side chains, which are attached at the 6 and 7 positions of the heme framework, are linked with Arg45 and Ser92, respectively, in sperm whale myoglobin. To evaluate the role of each propionate, two kinds of one-legged hemins, 6-depropionated and 7-depropionated protohemins, were prepared and inserted into the apomyoglobin to yield two reconstituted proteins. Structural data of the reconstituted myoglobins were obtained via an X-ray crystallographic analysis at a resolution of 1.1–1.4 Å and resonance Raman spectroscopy. It was found that the lack of the 6-propionate reduced the number of hydrogen bonds in the distal site and clearly changed the position of Arg45 residue with disrupting Arg45–Asp60 interaction. In contrast, the removal of the 7-propionate does not cause a significant structural change in the residues of the distal and proximal sites. However, the resonance Raman studies suggested that the coordination bond strength of His93–Fe bond for the protein with the 7-depropionated protoheme slightly increases compared to that for the protein with the native heme. The O_2 and CO ligand binding studies for the reconstituted proteins with the one-legged hemes provide an important insight into the functional role of each propionate. The lack of the 6-propionate accelerates the O_2 dissociation by ca. 3-fold compared to those of the other reconstituted and native proteins. The lack of the 7-propionate enhances the CO affinity by 2-fold compared to that of the protein with the native heme. These results indicate that the 6-propionate clearly contributes to the stabilization of the bound O_2, whereas the 7-propionate plays an important role in the regulation of the Fe–His bond.

Chapter 3

Cytochrome P450cam (P450cam) binds a protoheme IX as a prosthetic group via noncovalent interactions. Heme-6-propionate, one of the two heme-propionate side chains, forms hydrogen bonding interactions with Arg112 and other hydrophilic amino acid residues. Here, the author demonstrates the

structural and functional roles of the 6-propionate side chain in P450cam using a reconstituted protein with 6-depropionate-6-methylated protoheme IX (one-legged heme). The spectroscopic data and the enzymatic activities reveal that removal of the 6-propionate does not significantly have an influence on the enzyme property. In constant, its removal decreased the affinity of putidaredoxin (Pdx) by 3.5-fold supporting the proposed role of Arg112 as the essential constituent of the Pdx binding site. However, the rate of electron transfer from Pdx to ferric P450cam was not significantly changed. Resonance Raman experiments indicate that removal of the 6-propionate weakens the Fe–S bond strength and produces an inactive P420 species. The X-ray structure of the reconstituted protein at 1.55 Å resolution, which is highly superimposable with that of the wild-type protein, suggests the bulk water is accessible to the Cys357 heme ligand relative to the wild-type protein. Lengthening of the Fe–S bond and the water accessibility could facilitate protonation of thiolate anion to thiol, resulting in readily formation of the inactive P420 species. Therefore, the *d*-camphor hydroxylation reaction requires a 6-propionate–protein matrix interaction to maintain an active P450 species.

Chapter 4

Water must be expelled from the active site of monooxygenase cytochrome P450cam to allow the substrate (*d*-camphor) binding induced enzyme activation. To understand this mechanism, the author reconstituted the enzyme with an artificial one-legged heme where the heme-7-propionate is replaced with a methyl group. Although the reconstituted enzyme exhibited a normal ferrous-CO UV–vis spectrum, the monooxygenase activity decreased dramatically due to slow electron transfer from reduced putidaredoxin to the ferric enzyme. The ferric form of the reconstituted enzyme was found to predominantly remain in the 6-coordinated low-spin state in the presence of *d*-camphor, because *d*-camphor binding affinity decreased by a thousand-fold relative to that of the wild-type enzyme. X-ray structural analysis of the reconstituted enzyme at a 1.8 Å resolution revealed two structures, *d*-camphor-bound and unbound structures, with a novel water array extending from the active site to bulk water through the position occupied by the 7-propionate with a minimum change in the protein structure except for Asp297, which undergoes significant conformational changes to interact with the water array via hydrogen bond. The water array appears to prevent displacement of waters bound to the *d*-camphor binding site, thereby inhibiting *d*-camphor binding. The present findings suggests a water exclusion mechanism in the wild-type enzyme whereby 7-propionate side chain forms a gate with Arg299 and Asp297 residues through which water is expelled upon disruption of 7-propionate–Arg299 bond (gate opening) by transient flipping of Asp297 side chain driven by water displacement upon *d*-camphor binding.

References

1. Kadish, K. M., Smith, K. M., and Guilard, R., Eds. (2000) in *The Porphyrin Handbook*, Vol. 4, Academic Press, San Diego.
2. Turano, P., and Lu, Y. (2001) in *Handbook on Metalloproteins* (Bertini, I., Sigel, A., and Sigel, H., Eds.) Chap. 9, pp 269–356, Marcel Dekker, New York.
3. Schneider, S., Marles-Wright, J., Sharp, K. H., and Paoli, M. (2007) Diversity and conservation of interactions for binding heme in b-type heme proteins, *Nat. Prod. Rep. 24*, 621–630.
4. Philips, G. N., Jr. (2001) in *Handbook of Metalloproteins* (Messerschmidt, A., Huber, R., Poulos, T., and Wieghardt, K., Eds.) Vol. 1, pp 5–15, John Wiley & Sons, Chichester, U. K.
5. Springer, B. A., Sligar, S. G., Olson, J. S., and Phillips, G. N., Jr. (1994) Mechanisms of ligand recognition in myoglobin, *Chem. Rev. 94*, 699–714.
6. Rohlfs, R. J., Mathews, A. J., Carver, T. E., Olson, J. S., Springer, B. A., Egeberg, K. D., and Sligar, S. G. (1990) The effects of amino acid substitution at position E7 (residue 64) on the kinetics of ligand binding to sperm whale myoglobin, *J. Biol. Chem. 265*, 3168–3176.
7. Brantley, R. E., Jr., Smerdon, S. J., Wilkinson, A. J., Singleton, E. W., and Olson, J. S. (1993) The mechanism of autoxidation of myoglobin, *J. Biol. Chem. 268*, 6995–7010.
8. Carver, T. E., Brantley, R. E., Jr., Singleton, E. W., Arduini, R. M., Quillin, M. L., Phillips, G. N., Jr., and Olson, J. S. (1992) A novel site-directed mutant of myoglobin with an unusually high O_2 affinity and low autoxidation rate, *J. Biol. Chem. 267*, 14443–14450.
9. Liong, E. C., Dou, Y., Scott, E. E., Olson, J. S., and Phillips, G. N., Jr. (2001) Waterproofing the heme pocket, *J. Biol. Chem. 276*, 9093–9100.
10. Phillips, S. E. V. (1980) Structure and refinement of oxymyoglobin at 1.6 Å resolution, *J. Mol. Biol. 142*, 531–554.
11. Carver, T. E., Olson, J. S., Smerdon, S. J., Krzywda, S., Wilkinson, A. J., Gibson, Q. H., Blackmore, R. S., Ropp, J. D., and Sligar, S. G. (1991) Contributions of residues 45(CD3) and heme-6-propionate to the bimolecular and geminate recombination reactions of myoglobin, *Biochemistry 30*, 4697–4705.
12. Oldfield, T. J., Smerdon, S. J., Dauter, Z., Petratos, K., Wilson, K. S., and Wilkinson A. J. (1992) High-resolution X-ray structures of pig metmyoglobin and two CD3 mutants: Mb(Lys^{45}→Arg) and Mb(Lys^{45}→Ser), *Biochemistry 31*, 8732–8739.
13. Smerdon, S. J., Krzywda, S., Wilkinson, A. J., Brantley, R. E., Jr., Carver, T. E., Hargrove, M. S., and Olson, J. S. (1993) $Serine^{92}$(F7) contributes to the control of heme reactivity and stability in myoglobin, *Biochemistry 32*, 5132–5138.
14. Shiro, Y., Iizuka, T., Marubayashi, K., Ogura, T., Kitagawa, T., Balasubramanian, S., and Boxer, S. G. (1994) Spectroscopic study of Ser92 mutants of human myoglobin: Hydrogen bonding effect of Ser92 to proximal His93 on structure and property of myoglobin, *Biochemistry 33*, 14986–14992.
15. Lloyd, E., Burk, D. L., Ferrer, J. C., Maurus, R., Doran, J., Carey, P. R., Brayer, G. D., and Mauk, A. G. (1996) Electrostatic modification of the active site of myoglobin: Characterization of the proximal Ser92Asp variant, *Biochemistry 35*, 11901–11912.

16. Lim, A. R., Sishta, B. P., and Mauk, A. G. (2006) Contribution of the heme propionate groups to the electron transfer and electrostatic properties of myoglobin, *J. Inorg. Biochem. 100*, 2017–2023.
17. Hayashi, T., Matsuo, T., Hitomi, Y., Okawa, K., Suzuki, A., Shiro, Y., Iizuka, T., Hisaeda, Y., and Ogoshi, H. (2002) Contribution of heme-propionate side chains to structure and function of myoglobin: Chemical approach by artificially created prosthetic groups, *J. Inorg. Biochem. 91*, 94–100.
18. La Mar, G. N., Pande, U., Hauksson, J. B., Pandey, R. K., and Smith, K. M. (1989) Proton nuclear magnetic resonance investigation of the mechanism of the reconstitution of myoglobin that leads to metastable heme orientational disorder, *J. Am. Chem. Soc. 111*, 485–491.
19. Santucci, R., Ascoli, F., La Mar, G. N., Pandey, R. K., and Smith, K. M. (1993) Reconstitution of horse heart myoglobin with hemins methylated at 6- or 7-positions: A circular dichroism study, *Biochim. Biophys. Acta 1164*, 133–137.
20. Gao, Y., El-Mashtoly, S. F., Pal, B., Hayashi, T., Harada, K., and Kitagawa, T. (2006) Pathway of information transmission from heme to protein upon ligand binding/dissociation in myoglobin revealed by UV resonance Raman spectroscopy, *J. Biol. Chem. 281*, 24637–24646.
21. Gao, Y., Koyama, M., El-Mashtoly, S. F., Hayashi, T., Harada, K., Mizutani, Y., and Kitagawa, T. (2006) Time-resolved Raman evidence for energy 'funneling' through propionate side chains in heme 'cooling' upon photolysis of carbonmonoxy myoglobin, *Chem. Phys. Lett. 429*, 239–243.
22. Sono, M., Roach, M. P., Coulter, E. D., and Dawson, J. H. (1996) Heme-containing oxygenases, *Chem. Rev. 96*, 2841–2887.
23. (a) Joo, H., Lin, Z., and Arnold, F. H. (1999) Laboratory evolution of peroxidase-mediated cytochrome P450 hydroxylation, *Nature 399*, 670–673. (b) French, K. J., Rock, D. A., Rock, D. A., Manchester, J. I., Goldstein, B. M., and Jones, J. P. (2002) Active site mutations of cytochrome P450cam alter the binding, coupling, and oxidation of the foreign substrates *(R)*- and *(S)*-2-ethylhexanol, *Arch. Biochem. Biophys. 398*, 188–197. (c) Appel, D., Lutz-Wahl, S., Fischer, P., Schwaneberg, U., and Schmid, R. D. (2001) A P450 BM-3 mutant hydroxylates alkanes, cycloalkanes, arenes and heteroarenes, *J. Biotechnol. 88*, 167–171. (d) Li, Q.-S., Schwaneberg, U., Fischer, M. Schmitt, J. Pleiss, J., Lutz-Wahl, S., and Schmid, R. D. (2001) Rational evolution of a medium chain-specific cytochrome *P*-450 BM-3 variant, *Biochim. Biophys. Acta 1545*, 114–121. (e) Filipovic, D., Paulsen, M. D., Loida, P. J., Sligar, S. G., and Ornstein, R. L. (1992) Ethylbenzene hydroxylation by cytochrome P450cam, *Biochem. Biophys. Res. Commun. 189*, 488–495. (f) Loida, P. J., and Sligar, S. G. (1993) Engineering cytochrome P-450_{cam} to increase the stereospecificity and coupling of aliphatic hydroxylation, *Protein Eng. 6*, 207–212. (g) Bell, S. G., Chen, X., Sowden, R. J., Xu, F., Williams, J. N., Wong, L.-L., and Rao, Z. (2003) Molecular recognition in (+)-α-pinene oxidation by cytochrome $P450_{cam}$, *J. Am. Chem. Soc. 125*, 705–714.
24. (a) Poulos, T. L., Perez, M., and Wagner, G. C. (1982) Preliminary crystallographic data on cytochrome P-450_{CAM}, *J. Biol. Chem. 257,* 10427–10429. (b) Poulos, T. L., Finzel, B. C., Gunsalus, I. C., Wagner, G. C., and Kraut, J. (1985) The 2.6 Å crystal structure of *Pseudomonas putida* cytochrome

P-450, *J. Biol. Chem. 260*, 16122–16130. (c) Poulos, T. L., Finzel, B. C., and Howard, A. J. (1987) High-resolution crystal structure of cytochrome P450cam, *J. Mol. Biol. 195*, 687–700.

25. Dawson, J. H., and Sono, M. (1987) Cytochrome P-450 and chloroperoxidase: Thiolate-ligated heme enzymes. Spectroscopic determination of their active site structures and mechanistic implications of thiolate ligation, *Chem. Rev. 87*, 1255–1276.
26. (a) Sligar, S. G., and Gunsalus, I. C. (1976) A thermodynamic model of regulation: Modulation of redox equilibria in camphor monoxygenase, *Proc. Natl. Acad. Sci. USA 73*, 1078–1082. (b) Sligar, S. G. (1976) Coupling of spin, substrate, and redox equilibria in cytochrome P450, *Biochemistry 15*, 5399–5406. (c) Fisher, M. T., and Sligar, S. G. (1985) Control of heme protein redox potential and reduction rate: Linear free energy relation between potential and ferric spin state equilibrium, *J. Am. Chem. Soc. 107*, 5018–5019. (d) Reipa, V., Mayhew, M. P., Holden, M. J., and Vilker, V. L. (2002) Redox control of the P450cam catalytic cycle: effects of Y96F active site mutation and binding of a non-natural substrate, *Chem. Commun.* 318–319.
27. Groves, J. T., and McClusky, G. A. (1976) Aliphatic hydroxylation via oxygen rebound. Oxygen transfer catalyzed by iron, *J. Am. Chem. Soc. 98*, 859–861.
28. (a) Li, H. (2001) Cytochrome P450 in *Handbook of metalloproteins* (Messerschmidt, A., Huber, R., Poulos, T., and Wieghardt, K., Eds.) Vol. 1, pp 267–282, John Wiley & Sons, Chichester, U.K. (b) Pylypenko, O., and Schlichting, I. (2004) Structural aspects of ligand binding to and electron transfer in bacterial and fungal P450s, *Annu. Rev. Biochem. 73*, 991–1018.
29. Wagner, G. C., Perez, M., Toscano, W. A., Jr., and Gunsalus, I. C. (1981) Apoprotein formation and heme reconstitution of cytochrome P-450$_{cam}$, *J. Biol. Chem. 256*, 6262–6265.
30. (a) Wagner, G. C., Gunsalus, I. C., Wang, M.-Y. R., and Hoffman, B. M. (1981) Cobalt-substituted cytochrome P-450$_{cam}$, *J. Biol. Chem. 256*, 6266–6273. (b) Gelb, M. H., Toscano, W. A., Jr., and Sligar, S. G. (1982) Chemical mechanisms for cytochrome P-450 oxidation: Spectral and catalytic properties of a manganese-substituted protein, *Proc. Natl. Acad. Sci. USA 79*, 5758–5762. (c) Makris, T. M., Koenig, K., Schlichting, I., and Sligar, S. G. (2006) The status of high-valent metal oxo complexes in the P450 cytochromes, *J. Inorg. Biochem. 100*, 507–518. (d) Furukawa, Y., Ishimori, K., and Morishima, I. (2000) Electron transfer reactions in Zn-substituted cytochrome P450cam, *Biochemistry 39*, 10996–11004.
31. (a) Makino, R., Iizuka, T., Sakaguchi, K., and Ishimura, Y. (1982) Effects of heme substitution on the activity of heme-containing oxygenases, in *Oxygenase and oxygen metabolism* (Nozaki, M., Yamamoto. S., Ishimura, Y., Coon, M. J., and Ernster, L., Eds) pp 467–477, Academic Press, New York. (b) Kobayashi, K., Amano, M., Kanbara, Y., and Hayashi, K. (1987) One-electron reduction of the oxyform of 2,4-diacetyldeuterocytochrome P-450$_{cam}$, *J. Biol. Chem. 262*, 5445–5447.
32. (a) Goto, O., and Fujii-Kuriyama, Y. (1989) in *Frontier in Biotransformation* (Ruckpaul, K., and Rein, H., Eds.) pp 195–243, Adacemie-Verlag, Berlin. (b) Nelson, D. R., and Strobel, H. W. (1988) On the membrane topology of vertebrate cytochrome P-450 proteins *J. Biol. Chem. 263*, 6038–6050.
33. (a) Nagano, S., Shimada, H., Tarumi, A., Hishiki, T., Kimata-Ariga, Y., Egawa, T., Suematsu, M., Park,

S.-Y., Adachi, S., Shiro, Y., and Ishimura, Y. (2003) Infrared spectroscopic and mutational studies on putidaredoxin-induced conformational changes in ferrous CO-P450cam, *Biochemistry 42*, 14507–14514. (b) Koga, H., Sagara, Y., Yaoi, T., Tsujimura, M., Nakamura, K., Sekimizu, K., Makino, R., Shimada, H., Ishimura, Y., Yura, K., Go, M., Ikeguchi, M., and Horiuchi, T. (1993) Essential role of the Arg112 residue of cytochrome P450cam for electron transfer from reduced putidaredoxin, *FEBS Lett. 331*, 109–113. (c) Unno, M., Shimada, H., Toba, Y., Makino, R., and Ishimura, Y. (1996) Role of Arg^{112} of cytochrome $P450_{cam}$ in the electron transfer from reduced putidaredoxin, *J. Biol. Chem. 271*, 17869–17874.

34. Oprea, T. I., Hummer, G., and García, A. E. (1997) Identification of a functional water channel in cytochrome P450 enzymes, *Proc. Natl. Acad. Sci. USA 94*, 2133–2138.
35. Smith, K. M., and Craig, G. W. (1983) Porphyrin synthesis through tripyrrins: An alternate approach, *J. Org. Chem. 48*, 4302–4306.
36. (a) Smith, K. M. (1979) Protoporphyrin IX: Some recent research, *Acc. Chem. Res. 12*, 374–381. (b) La Mar., G. N., Emerson, S. D., Lecomte, J. T. J., Pande, U., Smith, K. M., Craig, G. W., and Kehres, L. A. (1986) Influence of propionate side chains on the equilibrium heme orientation in sperm whale myoglobin. Heme resonance assignments and structure determination by nuclear Overhauser effect measurement, *J. Am. Chem. Soc. 108*, 5568–5573. (c) La Mar, G. N., Budd, D. L., Viscio, D. B., Smith, K. M., and Langry, K. C. (1978) Proton nuclear magnetic resonance characterization of heme disorder in hemoprotein, *Proc. Natl. Acad. Sci. USA 75*, 5755–5759.

Chapter 1

Chemical Properties of Sperm Whale Myoglobins Reconstituted with Monodepropionated Hemins

1-1. Introduction

Protoheme IX is one of the most popular prosthetic groups in a series of hemoproteins [1]. The heme is bound in the heme pocket via multiple noncovalent interactions such as coordination, hydrophobic contact, hydrogen bonding and so on. In particular, two propionate side chains linked at the 6- and 7-positions of the heme framework exhibit unique hydrogen bonding networks with polar amino acid residues in the protein matrix. In the case of sperm whale myoglobin, two propionates interact with Arg45 and Ser92/His97 [2]. Over the past four decades since the elucidation of the 3D structure of myoglobin [3], the role of each heme-propionate in myoglobin has been discussed using site-directed mutagenesis or replacement of the native heme with a modified one. The latter procedure, modification of the heme-propionates, however, remains limited [4]. Hayashi et al. prepared two monodepropionate-mesohemins as artificial hemins in order to obtain an important insight into the relationship between the physiological function and heme-propionate side chains [5]. Nevertheless, mesohemin was not an appropriate prosthetic group for the structural and electronic model of the native protohemin. Therefore, the author prepared monodepropionated protoporphyrin IX iron complexes **1** and **2** as an exact model of the prosthetic groups for myoglobin as described by Smith et al. [6] with minor modifications. Although the reconstituted myoglobins with **1** and **2** have been reported by La Mar et al., only the NMR spectra of these proteins were discussed in their paper [4, 7]. In this chapter, the author reports the synthesis of the two hemins, **1** and **2** (Scheme 1-1 and Scheme 1-2), and the chemical properties of myoglobins reconstituted with them, particularly, a quantitative analysis of the heme-propionate–globin interaction in the protein matrix.

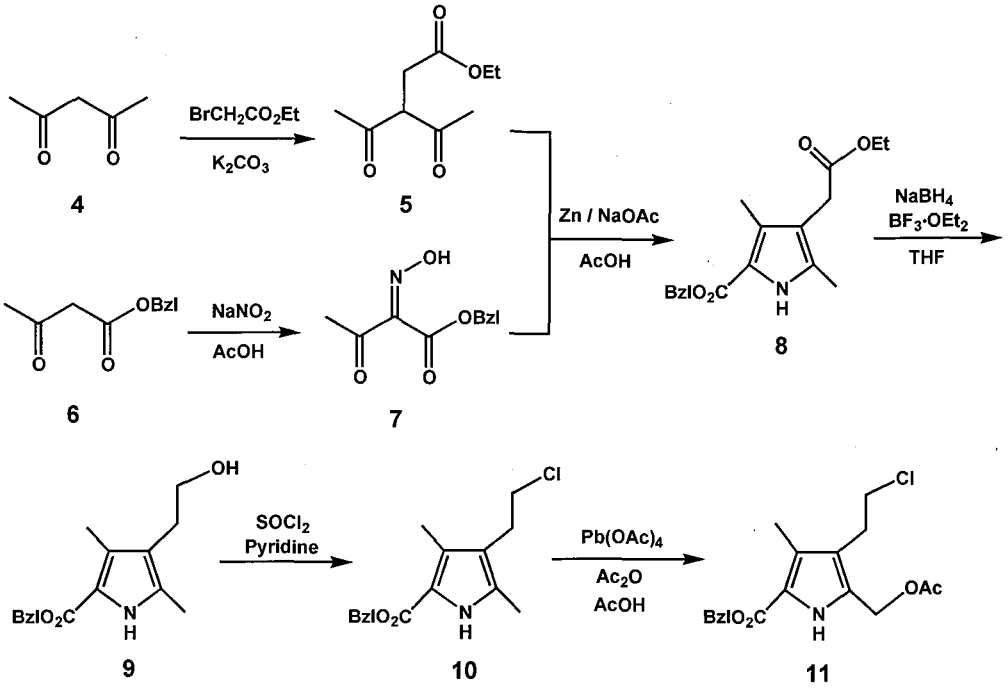

Scheme 1-1A.

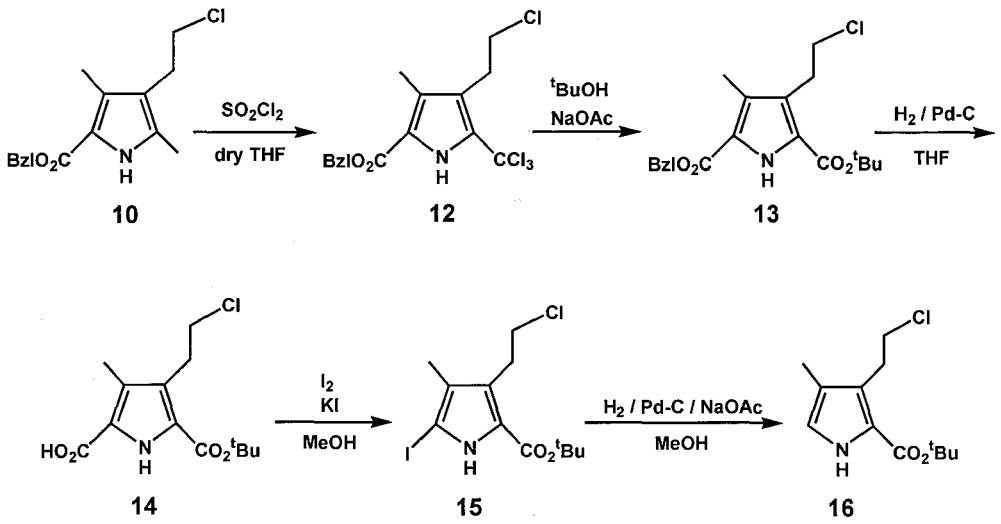

Scheme 1-1B.

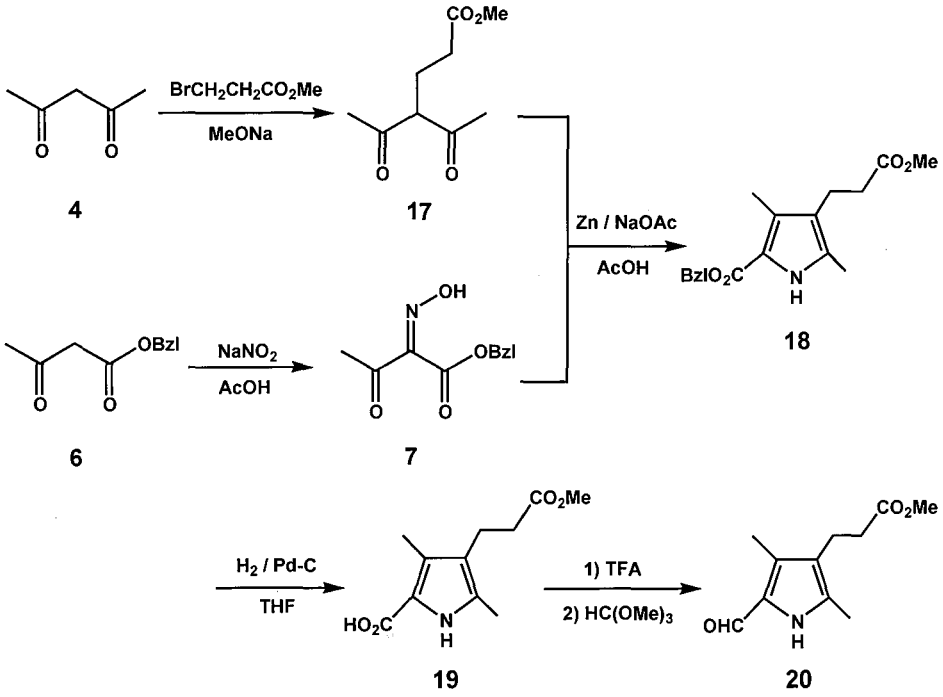

Scheme 1-1C.

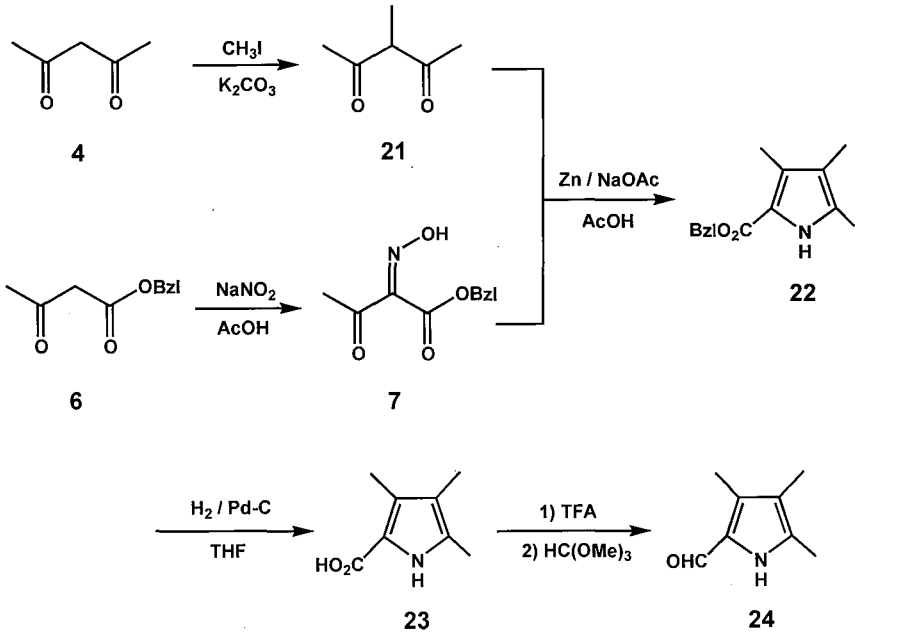

Scheme 1-1D.

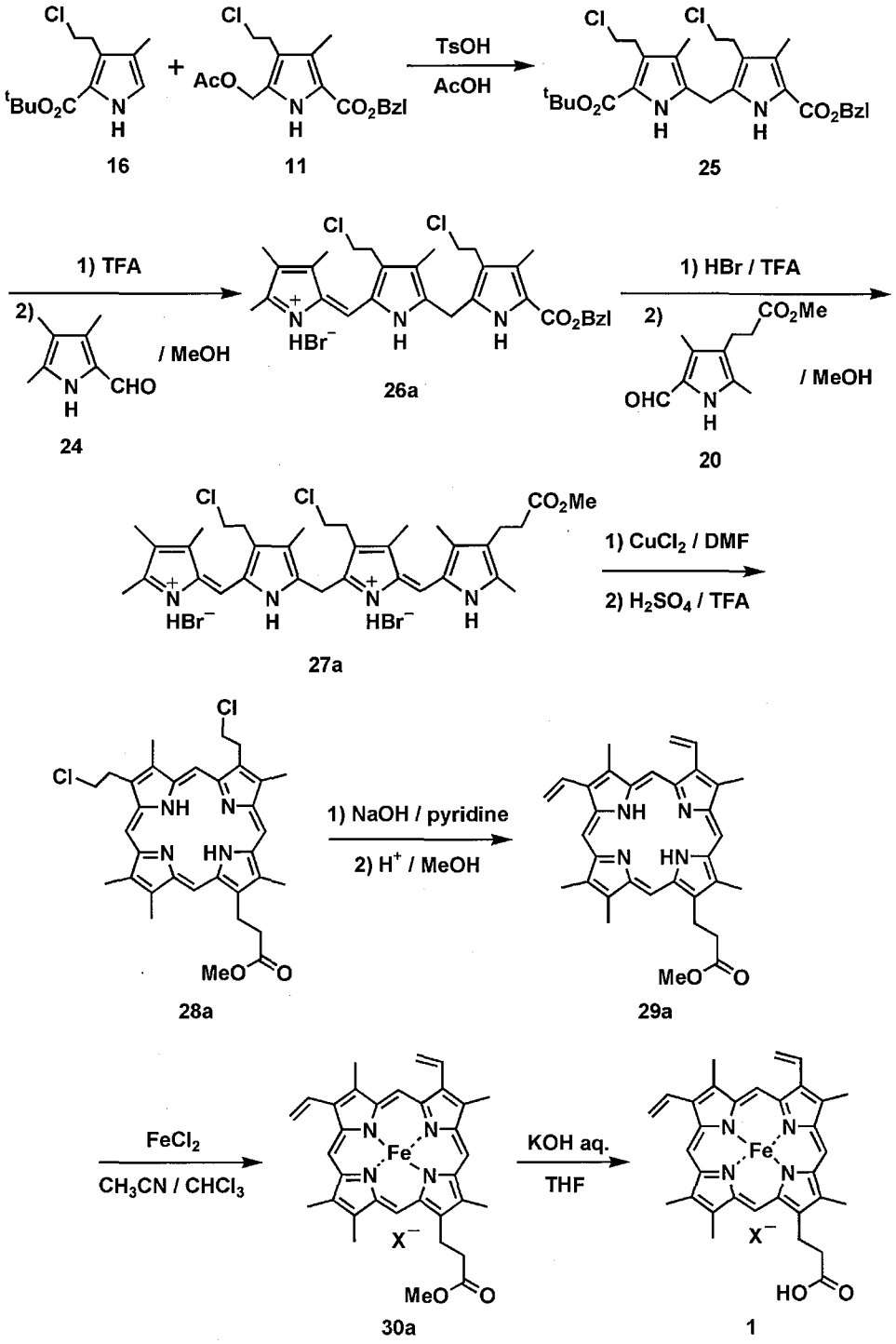
TsOH
AcOH
16
11
25
1) TFA
2)
/ MeOH
24
26a
1) HBr / TFA
2)
/ MeOH
20
1) CuCl2 / DMF
2) H2SO4 / TFA
27a
1) NaOH / pyridine
2) H+ / MeOH
28a
29a
FeCl2
CH3CN / CHCl3
KOH aq.
THF
30a
1

Scheme 1-2A.

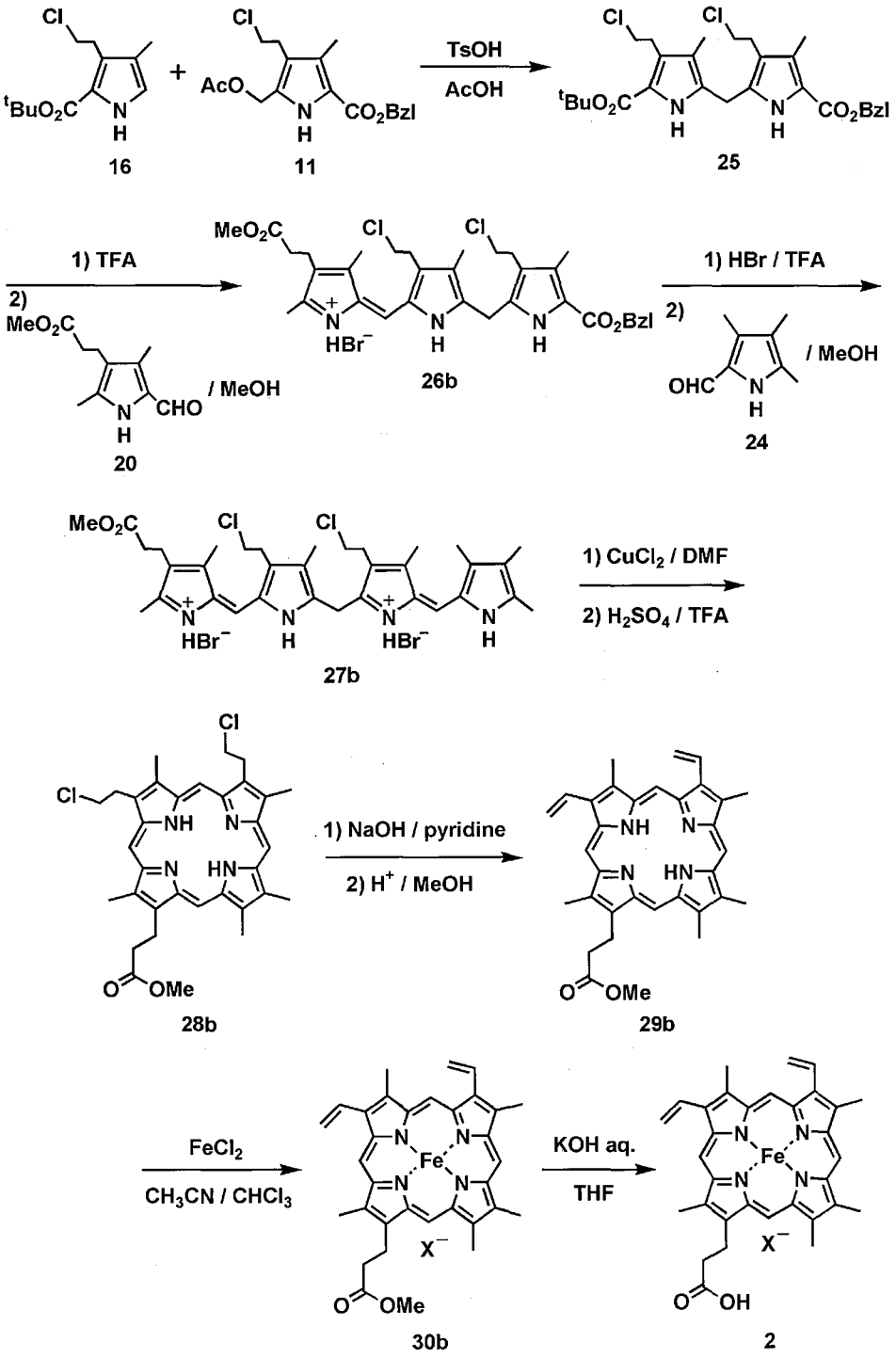
Cl
tBuO2C
N
H
16
+
AcO
CO2Bzl
11
TsOH
AcOH
25
1) TFA
2)
MeO2C
CHO
/ MeOH
20
HBr−
26b
1) HBr / TFA
2)
OHC
24
1) CuCl2 / DMF
2) H2SO4 / TFA
27b
NH
HN
OMe
28b
1) NaOH / pyridine
2) H+ / MeOH
29b
FeCl2
CH3CN / CHCl3
Fe
X−
30b
KOH aq.
THF
OH
2

Scheme 1-2B.

1-2. Experimental Section

1-2-1. Instruments

The UV–visible spectral measurements were conducted using a Shimadzu UV-3150 double beam spectrophotometer equipped with a thermostated cell holder with a 0.1 °C deviation. The mass analysis was carried out using a TOF mass spectrometer equipped with electrospray ionization on an Applied Biosystems Mariner API-TOF workstation. ^{1}H NMR spectra were collected on a Bruker AVANCE500 (500 MHz) NMR spectrometer. ^{1}H NMR chemical shift values are indicated in ppm relative to the residual solvent resonance. The pH values were monitored by a Beckman Φ71 pH meter.

1-2-2. Materials

All reagents of the highest guaranteed grade available were obtained from commercial sources and were used as received unless otherwise indicated. Organic solvents were dried and distilled under N_2 immediately before use. The native sperm whale myoglobin was purchased from Biozyme Laboratories, Ltd. and purified by passing through a CM-52 (Whatman) column. Distilled water was demineralized by a Millipore Milli-Q Academic A10 apparatus. The proteins were purified by column chromatography through a CM-52 (Whatman) and Sephadex G-25 (Amersham Biosciences). The native protohemin IX (**3**) was purchased from Tokyo Chemical Industry Co., Ltd.

1-2-3. Syntheses

Benzyl 5'-t-butoxycarbonyl-3,4'-bis(2-chloroethyl)-3',4-dimethylpyrromethane-5-carboxylate (**25**)

Benzyl 5-Acetoxymethyl-4-(2'-chloroethyl)-3-methylpyrrole-2-carboxylate (**11**) (2.67 g, 7.65 mmol), *t*-Butyl 3-(2'-Chloroethyl)-4-methylpyrrole-2-carboxylate (**16**) (1.86 g, 7.65 mmol), and *p*-toluenesulfonic acid (60 mg) were dissolved in glacial acetic acid (135 mL) and stirred at 40 °C for 4 h under nitrogen. After cooling to the room temperature, chloroform was then added, and the solution was poured into water. The aqueous layer was extracted with more chloroform and the organic extracts were combined, washed successively with saturated aqueous sodium hydrogen carbonate and water, and dried (Na_2SO_4). After filtration of the drying agent and removal of the solvent, the red oil was obtained. After the oil was dried with a vacuum pump, the dipyrromethane was obtained as a pink solid form.

^{1}H NMR ($CDCl_3$): δ (ppm) 9.50 , 9.18 (NH , each s , each 1H), 7.25 ~ 7.31 (ArH , m , 5H), 5.25 ($ArCH_2$, s, 2H), 3.85 (CH_2 , s , 2H), 3.59 , 3.38 , 3.13 , 2.83 (CH_2CH_2Cl , each t , each 2H , J = 8.1 , 7.7 , 7.8 , 7.6), 2.27 (CH_3 , s , 3H), 2.00 (CH_3 , s , 3H), 1.52 (^{t}Bu , s , 9H)

Benzyl 3,5-Bis(2-chloroethyl)-1,1',2,4,6-pentamethyl tripyrrin-a-6'-carboxylate Hydrobromide (**26a**)

Benzyl 5'-*t*-butoxycarbonyl-3,4'-bis(2-chloroethyl)-3',4-dimethylpyrromethane-5-carboxylate (**25**) (4.07 g, 7.65 mmol) was dissolved in trifluoroacetic acid (TFA) (35 mL) and stirred at room temperature for 20 min. Then, 2-formyl-3,4,5-trimethylpyrrole (**24**) (1.05 g, 7.65 mmol) dissolved in methanol (85 mL) was dropwise added to the solution. After stirring for 90 min at room temperature, 25% HBr in acetic acid solution 12 mL was added on ice. Diethyl ether was added, the precipitate appeared. After filtration of the precipitate, the orange powder was obtained (2.38 g, 3.77 mmol) in 49% yield (from **11** and **16**).
^{1}H NMR ($CDCl_3$): δ (ppm) 13.22 , 13.12 , 10.65 (NH , each s , each 1H), 7.49 ~ 7.50 (*o*-ArH , d , 2H, J = 7.0), 7.25 ~ 7.33 (*m* , *p*-ArH , m , 3H), 7.09 (−CH= , s , 1H), 5.31 ($ArCH_2$, s , 2H), 4.34 (CH_2 , s , 2H), 3.62 ~ 3.60 (CH_2CH_2Cl , t , 2H , J = 6.8), 3.39 ~ 3.37 (CH_2CH_2Cl , t , 2H , J = 6.7), 3.11 ~ 3.09 (CH_2CH_2Cl , t , 2H , J = 6.9), 2.94 ~ 2.90 (CH_2CH_2Cl , t , 2H , J = 7.9), 2.66 , 2.27 , 2.26 , 2.09 , 2.00 (Me , each s , each 3H)

Benzyl 3,5-Bis(2-chloroethyl)-1-(2-methoxycarbonylethyl)-1',2,4,6-tetramethyl-tripyrrin-a-6'-carboxylate Hydrobromide (**26b**)

Benzyl 5'-*t*-butoxycarbonyl-3,4'-bis(2-chloroethyl)-3',4-dimethylpyrromethane-5-carboxylate (**25**) (5.63 g, 10.8 mmol) was dissolved in trifluoroacetic acid (TFA) (50 mL) and stirred at room temperature for 20 min. Then, 2-formyl-4-(2-methoxoycarbonylethyl)-3,5-dimethylpyrrole (**20**) dissolved in methanol (120 mL) was dropwise added to the solution. After stirring for 90 min, 25% HBr in acetic acid solution 15 mL was added on ice. Diethyl ether was added, the precipitate appeared. After filtration of the precipitate, the orange powder was obtained (2.97 g, 4.21 mmol) in 39% yield (from **11** and **16**).
^{1}H NMR ($CDCl_3$): δ (ppm) 13.23 , 13.20 , 10.65 (NH , each s , each 1H), 7.47 ~ 7.48 (*o*-ArH , d , 2H , J = 7.3), 7.24 ~ 7.31 (*m* , *p*-ArH , m , 3H), 7.09 (−CH= , s , 1H), 5.29 ($ArCH_2$, s , 2H), 4.33 (CH_2 , s , 2H), 3.65 (CO_2Me , s , 3H), 3.60 ~ 3.58 (CH_2CH_2Cl , t , 2H , J = 6.8), 3.38 ~ 3.34 (CH_2CH_2Cl , t , 2H , J = 7.9), 3.09 ~ 3.06 (CH_2CH_2Cl , t , 2H , J = 6.8), 2.92 ~ 2.89 (CH_2CH_2Cl , t , 2H , J = 7.9), 2.76 ~ 2.73 ($CH_2CH_2CO_2Me$, t , 2H , J = 7.5), 2.47 ~ 2.44 ($CH_2CH_2CO_2Me$, t , 2H , J = 7.4), 2.68 , 2.29 , 2.24 , 2.07 (Me , each s , each 3H)

3,5-Bis(2-chloroethyl)-8-(2-methoxycarbonylethyl)-1,1',2,4,6,7,8'-heptamethyl-a,c-biladiene Dihydrobromide (**27a**)

Benzyl 3,5-Bis(2-chloroethyl)-1,1',2,4,6-pentamethyl tripyrrin-*a*-6'-carboxylate Hydrobromide (**26a**) (2.24 g, 3.55 mmol) was dissolved in 25% HBr in acetic acid solution (21 mL) and TFA (63 mL). After stirring for 6 h at room temperature with $CaCl_2$ tube, 2-formyl-4-(2-methoxycarbonylethyl)-3,5-dimethylpyrrole (**20**) (742 mg, 3.55 mmol) dissolved in methanol (140 mL) was dropwise added. After stirring for 1.5 h, diethyl ether was added and the precipitate was filtered to obtain dark red powder (1.64 g, 2.14 mmol) in 60% yield.

^{1}H NMR ($CDCl_3$): δ(ppm) 13.45 , 13.41 , 13.33 , 13.32 (NH , each s , each 1H), 7.15 , 7.12 (−CH= , each s , each 1H), 5.24 (CH_2 , s , 2H), 3.68 (CO_2Me , s , 3H), 3.60 ~ 3.57 ($CH_2CH_2CO_2Me$, t , 2H , J = 6.7), 3.05 ~ 3.02 (2 CH_2CH_2Cl , m , 4H), 3.10 ~ 3.08 (CH_2CH_2Cl , t , 2H , J = 6.7), 2.80 ~ 2.77 (CH_2CH_2Cl , t , 2H , J = 7.5), 2.74 (Me , s , 3H), 2.71 (Me , s , 3H), 2.50 ~ 2.49 ($CH_2CH_2CO_2Me$, t , 2H , J = 7.5), 2.34 , 2.30 , 2.30 , 2.02 , 2.00 (Me , each s , each 3H)

3,5-Bis(2-chloroethyl)-1-(2-methoxycarbonylethyl)-1',2,4,6,7,8,8'-heptamethyl-a,c-biladiene Dihydrobromide (**27b**)

Benzyl 3,5-Bis(2-chloroethyl)-1-(2-methoxycarbonylethyl)-1',2,4,6-tetramethyl-tripyrrin-*a*-6'-carboxylate Hydrobromide (**26b**) (1.50 g, 2.13 mmol) was dissolved in 25% HBr in acetic acid solution (13 mL) and TFA (39 mL). After stirring for 6 h at room temperature with $CaCl_2$ tube, 2-formyl-3,4,5-trimethylpyrrole (**24**) (292 mg, 2.13 mmol) dissolved in methanol (85 mL) was dropwise added. After stirring for 1.5 h, diethyl ether was added and the precipitate was filtered to obtain dark red powder (1.02 g, 1.32 mmol) in 62% yield.

^{1}H NMR ($CDCl_3$): δ(ppm) 13.53 , 13.37 , 13.35 , 13.30 (NH , each s , each 1H), 7.15 , 7.14 (−CH= , each s , each 1H), 5.25 (CH_2 , s , 2H), 3.69 (CO_2Me , s , 3H), 3.58 ~ 3.61 ($CH_2CH_2CO_2Me$, 2H , t , J = 6.7), 3.07 ~ 3.10 (2 CH_2CH_2Cl , m , 4H), 3.00 ~ 3.02 (CH_2CH_2Cl , 2H , t , J = 7.1), 2.77 ~ 2.80 (CH_2CH_2Cl , t , 2H , J = 7.5), 2.75 (Me , s , 3H), 2.71 (Me , s , 3H), 2.49 ~ 2.52 ($CH_2CH_2CO_2Me$, t , 2H , J = 7.5), 2.35 , 2.31 , 2.30 , 2.02 , 2.01 (Me , each s , each 3H)

2,4-Bis(2-chloroethyl)-7-(2-methoxycarbonylethyl)-1,3,5,6,8-pentamethylporphyrin (**28a**)

The *a,c*-biladiene dihydrobromide (**27a**) (200 mg, 0.26 mmol) was dissolved in dry DMF (100 mL) containing copper(II) chloride (600 mg). The solution was stirred for 2 h at room temperature under a stream of nitrogen. The reaction mixture was then diluted with chloroform and washed with water three times. The organic layer was dried over anhydrous Na_2SO_4 and evaporated to dryness. The residue was dissolved in 15% sulfuric acid in TFA (10 mL) and stirred for 45 min at room temperature. The solution was poured into cold water and extracted with chloroform. The organic layer was washed with aqueous sodium bicarbonate, then water, and dried over anhydrous Na_2SO_4. Filtration and evaporation of the solvent gave a crude product which was purified by chromatography (SiO_2, $CHCl_3$ / MeOH = 40:1). The appropriate eluates were evaporated to give the desired porphyrin (100 mg, 0.17 mmol) in 65% yield.

^{1}H NMR ($CDCl_3$): δ (ppm) 10.06 , 10.01 , 9.98 , 9.95 (meso , each s , each 1H), 4.52 ~ 4.47 ($CH_2CH_2CO_2Me$, CH_2CH_2Cl , m , 4H), 4.38 ~ 4.35 (CH_2CH_2Cl , t , 2H , J = 7.8), 4.31 ~ 4.27 (2 CH_2CH_2Cl , m , 4H), 3.66 , 3.64 , 3.63 , 3.60 , 3.60 , 3.59 (Me , CO_2Me , each s , each 3H), 3.26 ~ 3.23 ($CH_2CH_2CO_2Me$, t , 2H , J = 7.9), −3.79 (NH , s , 2H)

UV−vis ($CHCl_3$): λ_{max} (relative intensity) 401 nm (1.0), 499 (0.080), 533 (0.056), 568 (0.039), 622(0.027)

2,4-Bis(2-chloroethyl)6-(2-methoxycarbonylethyl)-1,3,5,7,8-pentamethylporphyrin (**28b**)

The *a,c*-biladiene dihydrobromide (**27b**) (83.2 mg, 0.108 mmol) was dissolved in dry DMF (40 mL) containing copper(II) chloride (244 mg). The solution was stirred for 2 h at room temperature under a stream of nitrogen. The reaction mixture was then diluted with chloroform and washed with water three times. The organic layer was dried over anhydrous Na_2SO_4 and evaporated to dryness. The residue was dissolved in 15% sulfuric acid in TFA (10 mL) and stirred for 45 min at room temperature. The solution was poured into cold water and extracted with chloroform. The organic layer was washed with aqueous sodium bicarbonate, then water, and dried over anhydrous Na_2SO_4. Filtration and evaporation of the solvent gave a crude product which was purified by chromatography (SiO_2, $CHCl_3$ / MeOH = 40:1). The appropriate eluates were evaporated to give the desired porphyrin (43.0 mg, 0.073 mmol) in 67% yield.

^{1}H NMR ($CDCl_3$): δ (ppm) 9.93 , 9.92 , 9.89 , 9.86 (meso , each s , each 1H), 4.43 ~ 4.46 ($CH_2CH_2CO_2Me$, t , 2H , J = 7.8), 4.37 ~ 4.40 (CH_2CH_2Cl , t , 2H , J = 7.8), 4.31 ~ 4.34 (CH_2CH_2Cl , t , 2H , J = 8.0), 4.22 ~ 4.28 (2 CH_2CH_2Cl , m , 4H), 3.68 , 3.58 , 3.57 , 3.53 , 3.52 (Me , each s , each 3H), 3.52 (CO_2Me , s , 3H), 3.21 ~ 3.24 ($CH_2CH_2CO_2Me$, t , 2H , J = 7.8), −3.98 (NH , s , 2H)

UV−vis ($CHCl_3$): λ_{max} (relative intensity) 401 nm (1.0), 499 (0.068), 534 (0.052), 568 (0.040), 622(0.021)

7-(2-methoxycarbonylethyl)-1,3,5,6,8-pentamethyl-2,4-divinylporphyrin (**29a**)

The porphyrin (**28a**) (100 mg, 0.17 mmol) was dissolved in degassed pyridine (20 mL) containing 3% aqueous sodium hydroxide (20 mL). The mixture was refluxed and stirred for 3 h under a stream of nitrogen. The cooled mixture was treated with dilute aqueous acetic acid and extracted with chloroform and washed with water 3 times. The organic layer was dried over anhydrous Na_2SO_4 and evaporated to dryness. The residue was dissolved in 5% sulfuric acid in methanol (150 mL) and set aside overnight in the dark. The mixture was poured into cold water and extracted with chloroform. The organic layer was washed with aqueous sodium bicarbonate, then water and dried. Evaporation gave a residue which was chromatographed on silica gel ($CHCl_3$ / MeOH = 40:1), and the appropriate eluates were evaporated to give the desired product (53 mg, 0.10 mmol) in 61% yield after recrystallization from dichloromethane / *n*-hexane.

^{1}H NMR ($CDCl_3$): δ (ppm) 10.22 , 10.13 , 10.07 , 9.96 (meso , each s , each 1H), 8.33 ~ 8.24 (vinyl H , m , 2H), 6.40 ~ 6.33 (vinyl H , m , 2H), 6.20 ~ 6.15 (vinyl H , m , 2H), 4.38 ~ 4.35 ($CH_2CH_2CO_2Me$, t , 2H , J = 7.9), 3.72 , 3.69 , 3.67 , 3.60 , 3.58 , 3.57 (Me and CO_2Me , each s , each 3H), 3.26 ~ 3.23 ($CH_2CH_2CO_2Me$, t , 2H , J = 7.9), −3.69 (NH , s , 2H)

UV−vis ($CHCl_3$): λ_{max} (relative intensity) 407 nm (1.0), 506 (0.084), 541 (0.070), 576 (0.041), 630(0.031)

6-(2-methoxycarbonylethyl)-1,3,5,7,8-pentamethyl-2,4-divinylporphyrin (**29b**)

The porphyrin (**28b**) (43.0 mg, 0.073 mmol) was dissolved in degassed pyridine (5 mL) containing 3% aqueous sodium hydroxide (5 mL). The mixture was refluxed and stirred for 3 h under a stream of nitrogen. The cooled mixture was treated with dilute aqueous acetic acid and extracted with chloroform and washed with water 3 times. The organic layer was dried over anhydrous Na_2SO_4 and evaporated to dryness. The residue was dissolved in 5% sulfuric acid in methanol (30 mL) and set aside overnight in the dark. The mixture was poured into cold water and extracted with chloroform. The organic layer was washed with aqueous sodium bicarbonate, then water and dried. Evaporation gave a residue which was chromatographed on silica gel ($CHCl_3$ / MeOH = 40:1), and the appropriate eluates were evaporated to give the desired product (18 mg, 0.034 mmol) in 47% yield after recrystallization from dichloromethane / *n*-hexane.

^{1}H NMR ($CDCl_3$): δ (ppm) 10.26 , 10.20 , 10.09 , 10.01 (meso , each s , each 1H), 8.29 ~ 8.33 (vinyl H , m , 2H), 6.37 ~ 6.43 (vinyl H , m , 2H), 6.19 ~ 6.22 (vinyl H , m , 2H), 4.38 ~ 4.41 ($CH_2CH_2CO_2Me$, t , 2H , J = 7.9), 3.75 , 3.73 , 3.70 , 3.66 , 3.60 , 3.50 (Me and CO_2Me , each s , each 3H), 3.26 ~ 3.29 ($CH_2CH_2CO_2Me$, t , 2H , J = 7.9), −3.65 (NH , s , 2H)

UV−vis ($CHCl_3$): λ_{max} (relative intensity) 407 nm (1.0), 506 (0.082), 541 (0.070), 576 (0.042), 630(0.032)

Iron(III)-7-(2-methoxycarbonylethyl)-1,3,5,6,8-pentamethyl-2,4-divinylporphyrin (**30a**)

To the solution of ferrous chloride hydrate (400 mg) in dry acetonitrile (20 mL), a solution of the porphyrin (**29a**) (53 mg, 0.10 mmol) in nitrogen-purged $CHCl_3$ (20 mL) was dropwise added with stirring at 55 °C under a stream of nitrogen. After complete addition, the mixture was stirred for 1 h under nitrogen. The cooled mixture was exposed to air and stirred for 25 min at room temperature. The resulting brown solution was then diluted with chloroform and washed with 0.1 M HCl aq. and then with brine. The organic layer was dried over anhydrous Na_2SO_4. Filtration and evaporation of the solvent gave a brown residue which was purified by chromatography (SiO_2, $CHCl_3$ / MeOH = 20:1) and the desired product was obtained quantitatively.

MS(ESI TOF) calculated for $[M-Cl]^+$ $C_{33}H_{32}N_4O_2Fe^+$, 572.19; found 572.25

UV–vis ($CHCl_3$): λ_{max} (relative intensity) 387 nm (1.0), 509 (0.11), 541 (0.10), 642(0.051)

Iron(III)-6-(2-methoxycarbonylethyl)-1,3,5,7,8-pentamethyl-2,4-divinylporphyrin (**30b**)

To the solution of ferrous chloride hydrate (500 mg) in dry acetonitrile (20 mL), a solution of the porphyrin (**29b**) (50 mg, 0.096 mmol) in nitrogen-purged $CHCl_3$ (20 mL) was dropwise added with stirring at 55 °C under a stream of nitrogen. After complete addition, the mixture was stirred for 1 h under nitrogen. The cooled mixture was exposed to air and stirred for 25 min at room temperature. The resulting brown solution was then diluted with chloroform and washed with 0.1 M HCl aq. and then with brine. The organic layer was dried over anhydrous Na_2SO_4. Filtration and evaporation of the solvent gave a brown residue which was purified by chromatography (SiO_2, $CHCl_3$ / MeOH = 20:1) and the desired product was obtained quantitatively.

MS(ESI TOF) calculated for $[M-Cl]^+$ $C_{33}H_{32}N_4O_2Fe^+$, 572.19; found 572.21

UV–vis ($CHCl_3$): λ_{max} (relative intensity) 389 nm (1.0), 513 (0.11), 541 (0.10), 642(0.044)

Iron(III)-7-(2-carboxyethyl)-1,3,5,6,8-pentamethyl-2,4-divinylporphyrin (**1**)

The iron porphyrin methyl ester (**30a**) (80 mg, 0.14 mmol) was dissolved in THF (20 mL) containing 0.2 M aqueous potassium hydroxide (20 mL). The solution was stirred for 5 h at room temperature. The mixture was diluted with chloroform and was treated with 1 M HCl aq. to adjust to pH 3. The organic layer was washed with 0.1 M HCl aq., then brine and dried. Filtration and evaporation of the solvent gave the desired product.

MS(ESI TOF) calculated for $[M-Cl]^+$ $C_{32}H_{30}N_4O_2Fe^+$, 558.17; found 558.18

UV–vis (CH_2Cl_2): λ_{max} (relative intensity) 386 nm (1.0), 510 (0.10), 543 (0.098), 641(0.051)

Iron(III)-6-(2-carboxylethyl)-1,3,5,7,8-pentamethyl-2,4-divinylporphyrin (**2**)

The iron porphyrin methyl ester (**30b**) (80 mg, 0.14 mmol) was dissolved in THF (20 mL) containing 0.2 M aqueous potassium hydroxide (20 mL). The solution was stirred for 5 h at room temperature. The mixture was diluted with chloroform and was treated with 1 M HCl aq. to adjust to pH 3. The organic layer was washed with 0.1 M HCl aq., then brine and dried. Filtration and evaporation of the solvent gave the desired product.

MS(ESI TOF) calculated for $[M-Cl]^+$ $C_{32}H_{30}N_4O_2Fe^+$, 558.17; found 558.16

UV–vis (CH_2Cl_2): λ_{max} (relative intensity) 386 nm (1.0), 511 (0.11), 539 (0.10), 641(0.049)

1-2-4. Methods

Protein reconstitution with one-legged hemin. The sperm whale apomyoglobin was prepared from the native metmyoglobin by Teale's 2-butanone method [8]. A solution of the apomyoglobin was prepared by dissolving lyophilized powder (8.6 mg) in chilled 100 mM potassium phosphate buffer (pH 7.0). A 1.2-equivalent amount of the one-legged hemin was dissolved in pyridine (400 μL), and the mixture was dropwise added to the solution of apomyoglobin (ca. 40 mL). After being shaken for 1.5 h at 4 °C, the solution was dialyzed against 1 L of 100 mM potassium phosphate buffer (pH 7.0) for 12 h at 4 °C. After the mixture was centrifuged (3000 rpm for 20 min at 4 °C) and concentrated (ca. 0.5 mL), the solution was passed through a Sephadex G-25 column (Φ 1.5 cm × 30 cm) equilibrated with 100 mM potassium phosphate buffer (pH 7.0). The solution of a purified reconstituted myoglobin was concentrated (ca. 1 mM) and maintained at 4 °C.

Determination of pKa value of the water coordinated to the heme iron. Electronic absorption spectra of metmyoglobin (ca. 3 mL, 5 μM) in an aqueous solution of 100 mM KCl were monitored at 25 °C under various pH conditions adjusted by incremental additions of aqueous solution of 0.1 M KOH (< 2 μL). The pH values of the solutions were recorded before and after measurements of the electronic absorption spectra. The data were fitted to Henderson-Hasselbach equation for one proton process (eq. 1-1) [9],

$$Z = [A_{\text{neutral}} + A_{\text{base}} \times 10^{(\text{pH-p}Ka)}] / [1 + 10^{(\text{pH-p}Ka)}] \quad (1\text{-}1)$$

where Z is absorbance at a certain pH; A_{neutral} and A_{base} are absorbances of neutral and basic forms, respectively.

Determination of $pK_{1/2}$ value. Electronic absorption spectra of metmyoglobin (ca. 3 mL, 5 μM) in an aqueous solution of 100 mM KCl were monitored at 25 °C under various pH conditions adjusted by incremental additions of aqueous solution of 0.1 M HCl (< 2 μL). The pH values of the solutions were recorded before and after measurements of the electronic absorption spectra. The data were fitted to Henderson-Hasselbach equation for one proton process (eq. 1-2) [9],

$$Z = [A_{\text{acid}} + A_{\text{neutral}} \times 10^{c(\text{pH-p}K1/2)}] / [1 + 10^{c(\text{pH-p}K1/2)}] \quad (1\text{-}2)$$

where Z is absorbance at a certain pH; A_{neutral} and A_{acid} are absorbances of neutral and acidic forms, respectively; c is an arbitrary constant.

Determination of the apparent hemin affinity for apomyoglobin. To evaluate the apparent hemin affinity for apomyoglobin, titrimetric measurements were carried out by monitoring the spectral changes of the hemins upon the addition of the apoprotein in 100 mM potassium phosphate buffer solutions containing 5% pyridine at 25 °C. Each spectrum was obtained after equilibrium of the hemin insertion into the

apoprotein occurred (over 30 min). From the spectral changes of the Soret maxima to the 408 nm red-shift with several clear isosbestic points, the apparent free energy changes of the hemin binding for the apoprotein were determined.

1-3. Results

Synthesis of one-legged hemins. Monodepropionated hemins were prepared by the slightly modified Smith's method [6]. In the synthetic scheme of **1** and **2**, cyclization of the *a,c*-biladiene salt **27a** and **27b** to give the corresponding porphyrins **28a** and **28b**, respectively, is one of the key steps. The yield of **28a** and **28b** from **27a** and **27b**, respectively, was less than 30% under the literature conditions at 145 °C [6]. In contrast, the author found that lowering the reaction temperature and dilution of the reaction mixture with DMF prevented the byproduct formation and enhanced the yield to 65−70% [10].

The four kinds of pyrroles were synthesized as previously reported [11]. Unsymmetrically substituted dipyrromethane **25** could be prepared by condensation of 2-acetoxymethylpyrrole **11** with 2-unsubstituted pyrrole **16** in acetic acid containing a catalytic amount of toluene *p*-sulfonic acid in glacial acetic acid at 40 °C for 4 h under nitrogen atmosphere.

Synthesis of the 6-methyl-6-depropionated protoporphyrin isomer **29a** involved deprotection of the pyrromethane **25** with TFA at room temperature for 20 min followed by condensation of the formylpyrrole **24** in methanol at room temperature for 90 min. Crystallization from diethyl ether gave the desired tripyrrin hydrobromide **26a** in 49% yield (from **11** and **16**). Treatment of this tripyrrin with TFA at room temperature for 6 h followed by addition of the formylpyrrole **20**, afforded the *a,c*-biladiene **27a** in 60% yield. Cyclization of **27a** with copper(II) chloride in dimethylformamide (DMF) for 2 h at room temperature afforded a good yield of the copper(II) porphyrin. Demetalation with 15% sulfuric acid in TFA gave the porphyrin **28a** in 65% yield. Dehydrochlorination in pyridine and sodium hydroxide under an inert atmosphere led to the divinylporphyrin isomer **29a** in 61% yield following reesterification with 5% sulfuric acid-methanol at room temperature overnight in the dark. In a similar manner, the pyrromethane **25** was deprotected with TFA and condensed with the formylpyrrole **20** to give the tripyrrin hydrobromide **26b** in 39% yield (from **11** and **16**). Deprotection of the benzyl ester with 25% HBr in acetic acid and TFA, followed by condensation with the formylpyrrole **24** afforded the *a,c*-biladiene **27b** in 62% yield. Cyclization of **27b** with copper(II) chloride in dimethylformamide afforded the copper(II) porphyrin. Demetalation with 15% sulfuric acid in TFA afforded the porphyrin **28b** in 67% yield. Dehydrochlorination gave the 7-methyl-7-depropionated protoporphyrin isomer **29b** in 47% yield. The free base porphyrins **29a** and **29b** were converted into the corresponding hemin monomethyl esters (**30a** and **30b**, respectively) by using iron insertion with ferrous chloride in acetonitrile/chloroform. These esters were hydrolyzed to afford the corresponding hemins, **1** and **2**, by using 0.1 M KOH in aqueous THF.

Preparation and characterization of reconstituted myoglobins. Insertion of hemins **1**–**3** into the sperm whale apomyoglobin was carried out by a conventional method. The author used the myoglobin rMb(**3**) reconstituted with the native prosthetic group, protohemin IX (**3**), as the reference protein instead of the native myoglobin, because of the reducing experimental artifacts. The ESI-TOF mass spectroscopy measurement of the reconstituted ferric proteins showed the corresponding desired mass numbers of 17,760.8 and 17,760.3 for rMb(**1**) and rMb(**2**), respectively (Figure 1-1).

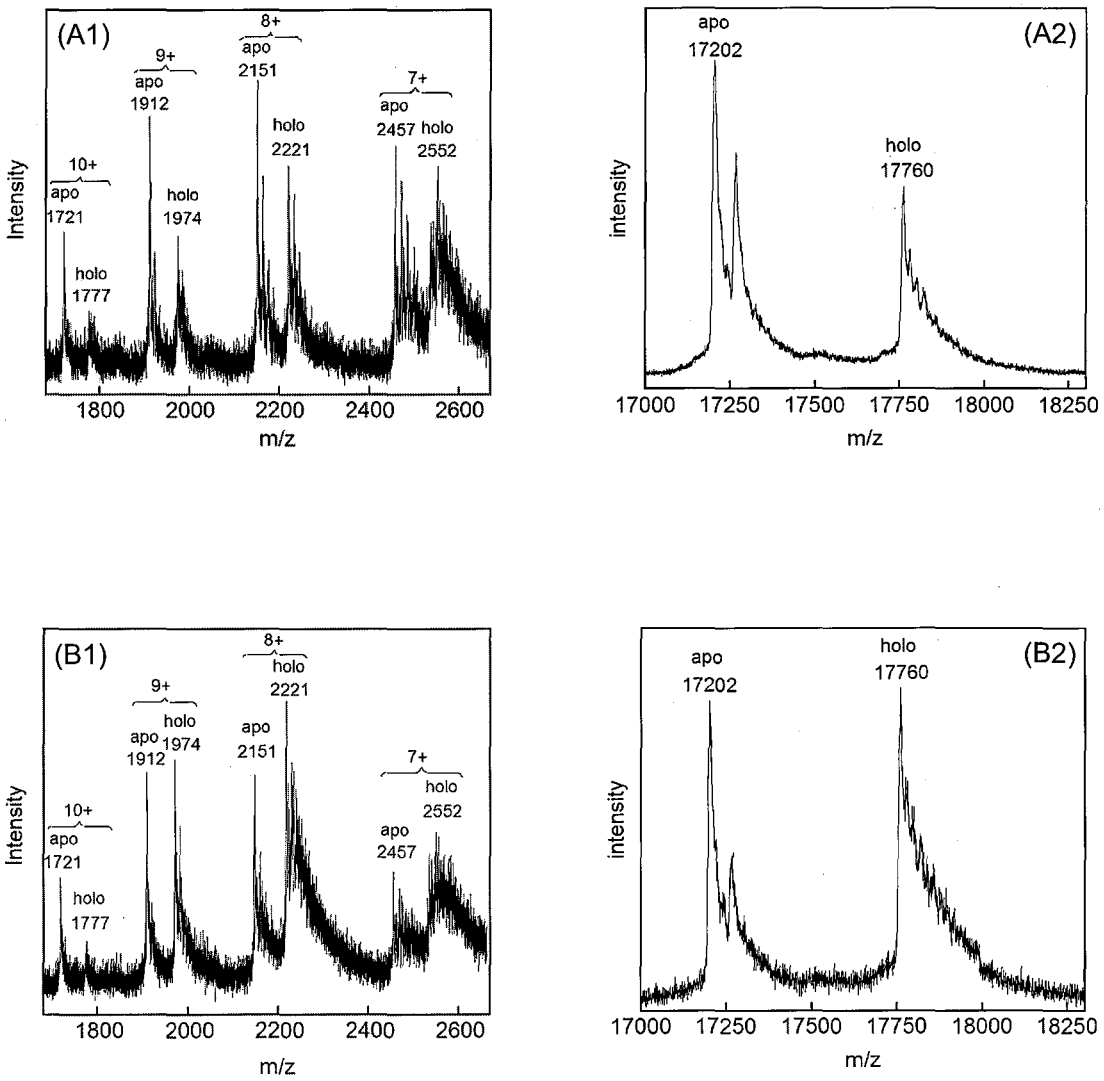

Figure 1-1. ESI-TOF mass spectra of met-rMb in 10 mM ammonium acetate buffer containing 50% methanol and 0.1% formic acid. (A1) rMb(**1**), (B1) rMb(**2**), deconvoluted mass spectra of met-rMb (A2) rMb(**1**), (B2) rMb(**2**). The nozzle potential was 160 V for rMb(**1**) and 90 V for rMb(**2**).

The spectra of met-rMb(**1**) and met-rMb(**2**) are almost the same as those for the native myoglobin and rMb(**3**) as shown in Figure 1-2.

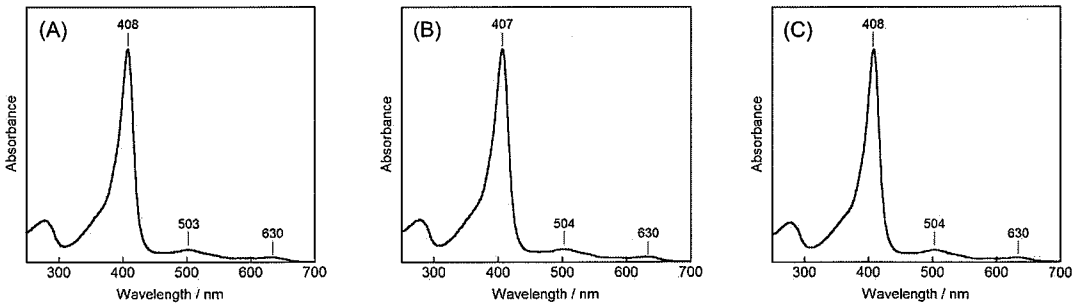

Figure 1-2. UV–vis spectra of (A) rMb(**1**), (B) rMb(**2**), and (C)rMb(**3**) in 100 mM KPi(pH 7.0) buffer at 25 °C.

The $pK_{1/2}$ value. From the titration curve generated from the absorbance changes at 408 nm, $pK_{1/2}$ which correspond to the pH value upon release of the 50% hemin from the protein matrix. The Soret band at 408 nm was replaced with a broad band at 380–385 nm below pH 4 with several isosbestic points, and the latter spectrum is characteristic of the free hemin. From the pH titration curves as shown in Figure 1-3, the $pK_{1/2}$ values, which correspond to the pH value for 50% hemin dissociation, were determined. Table 1-1 demonstrates that **1** and **2** are released from the protein matrix at ca. pH 4.3–4.4 which is 0.2 units higher than that observed for the native myoglobin.

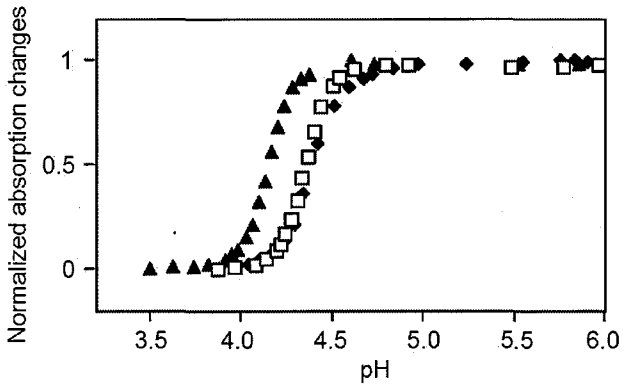

Figure 1-3. pH titration of myoglobins in the lower pH region: rMb(**1**) (□), rMb(**2**) (◆), and rMb(**3**) (▲). The Soret maxima at 408 nm were monitored at 25 °C in 100 mM KCl.

The pK_a value of the water coordinated to the heme iron. The pK_a values, which demonstrate the acid–alkaline equilibrium constants for rMb(**1**) and rMb(**2**), are clearly shifted in the acid direction by approximately 0.25 pH units compared to that observed for rMb(**3**) as shown in Table 1-1.

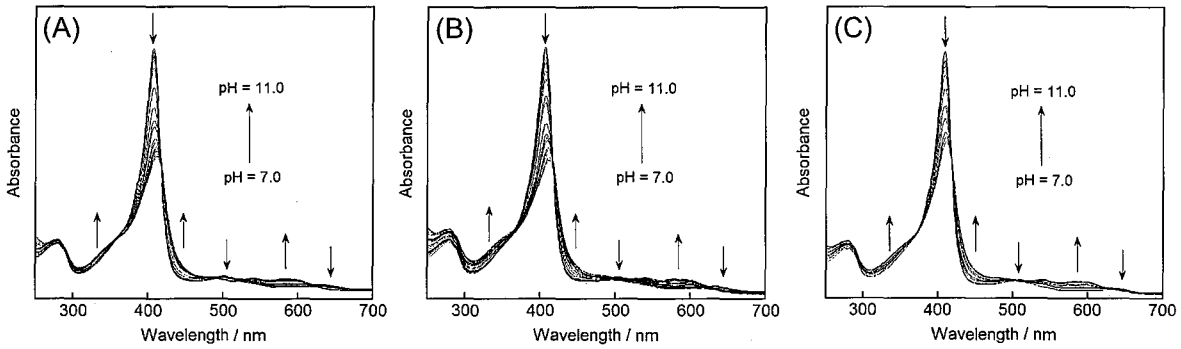

Figure 1-4. UV–vis spectra of Mbs at various pH during the alkaline titration in 100 mM KCl at 25 °C. (A) rMb(**1**), (B) rMb(**2**), and (C) rMb(**3**)

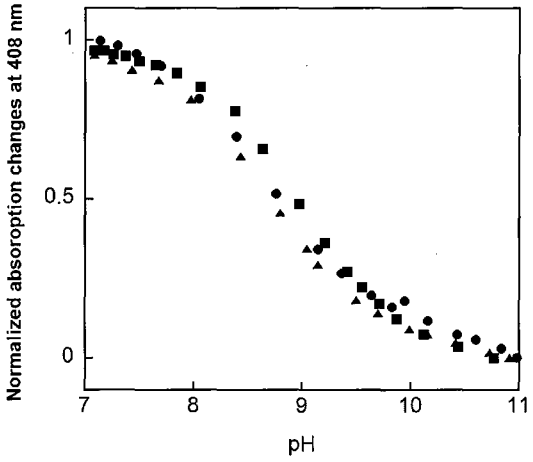

Figure 1-5. pH titration of myoglobins in the higher pH region: rMb(**1**) (▲), rMb(**2**) (●), rMb(**3**) (■). The Soret maxima at 408 nm were monitored at 25 °C in 100 mM KCl.

Table 1-1. pK_a and $pK_{1/2}$ values for native and reconstituted sperm whale myoglobins at 25 °C[a,b]

protein	pK_a[c]	$pK_{1/2}$[d]
rMb(**1**)	8.67	4.34
rMb(**2**)	8.73	4.38
rMb(**3**)	8.95	4.16

[a] 100 mM KCl. [b] Standard deviations in pK_a and $pK_{1/2}$ are all within 0.03. [c] For acid–alkaline equilibrium of aquomet form. [d] pH value upon 50% hemin dissociation from the protein matrix.

1-4. Discussion

Iron complex of protoporphyrin IX, that is heme, is the prosthetic group in the oxygen transport and storage proteins hemoglobin and myoglobin [12]. Either heme or a peripherally modified form is the center of action in the cytochromes [13] and in the peroxidase [14] and catalase [15] enzymes. The structures of these heme compounds in the enzymes are unsymmetrical. For example, symmetrically substituted porphyrin compounds such as octaethylporphyrin are most efficiently synthesized by polymerization of a suitable monopyrrole. On the other hand, without exquisite biosynthetic machinery, there is no way to synthesize unsymmetrical porphyrins by monopyrrole self-condensation. If laborious separations of mixtures are to be avoided, totally unsymmetrical porphyrins must usually be synthesized by cyclization of a preformed open chain tetrapyrrole such as an *a,c*-biladiene. For unsymmetrical porphyrins synthesis, it is important to describe the synthesis of monopyrroles [11], and like wise describe methods for fashioning these into acyclic oligopyrroles (dipyrromethanes, tripyrrins, and *a,c*-biladienes). Unsymmetrically substituted dipyrromethanes can be prepared by condensation of 2-acetoxymethylpyrroles with 2-unsubstituted pyrroles in acetic acid containing a catalytic amount of toluene *p*-sulfonic acid. Deprotection of the pyrromethane with TFA followed by condensation of the formylpyrrole in methanol leads to the formation of the tripyrrin which bears benzyl ester as protected group. Cleavage of the benzyl ester with HBr/TFA followed by addition of formylpyrrole affords the *a,c*-biladiene salt. Cyclization of the 1',8'-dimethyl-*a,c*-biladiene salt in dimethylformamide using copper(II) chloride gives the copper(II) porphyrin and demetalation of this compound with 15% sulfulic acid in TFA gives the unsymmetrical porphyrin. Smith, La Mar and their coworkers had been interested in the structural properties, electronic structure and the orientation of heme in hemoprotein matrix which could be obtained by NMR spectroscopy [4, 16]. Therefore, they synthesized various symmetrical, unsymmetrical, deuterium- and carbon-13-labeled derivatives of protoporphyrin IX [10, 11(d), 17] and inserted them as iron complexes into hemoproteins. Because the author has been interested in the functional role of heme propionate side chains in hemoproteins, the author prepared monodepropionated protoporphyrin IX iron complexes as described by Smith et al. [6] with minor modifications.

The insertion of the obtained **1** and **2** into apomyoglobin from the sperm whale was carried out using a conventional method [18, 19]. The characterization of the reconstituted proteins, rMb(**1**) and rMb(**2**), were carried out by not only ^{1}H NMR but also ESI-TOF mass spectroscopy (Figure 1-1). In addition, the UV−vis spectra of rMb(**1**) and rMb(**2**) were almost completely consistent with that observed for the native myoglobin and rMb(**3**) at pH 7.0 (Figure 1-2).

The pK_a values, which demonstrate the acid−alkaline equilibrium constants for rMb(**1**) and rMb(**2**), are clearly shifted in the acid direction by approximately 0.25 pH units compared to that observed for the native protein. It is known that the esterification of the two heme-propionate side chains with methyl groups in myoglobin gives smaller pK_a values than that for native protein, thus, the low pK_as for the distal water ligand in rMb(**1**) and rMb(**2**) results from the same effect observed in the previous studies [20]. Next, the hemin dissociation from the protein matrix was monitored in the lower pH region. The Soret band at 408 nm was replaced with a broad band at 380−385 nm below pH 4 with several isosbestic points,

and the latter spectrum is characteristic of the free hemin. From the pH titration curves as shown in Figure 1-3, the $pK_{1/2}$ values, which correspond to the pH value for 50% hemin dissociation, were determined. Table 1-1 demonstrates that **1** and **2** are released from the protein matrix at ca. pH 4.3–4.4 which is 0.2 units higher than that observed for the native myoglobin. This finding suggests that the lack of the one of the propionates decreases the hemin stability in the heme pocket. In general, the hemin is mainly stabilized by Fe^{3+}–His93 coordination and hydrophobic contact between the hemin and apolar amino acid residues [21]. In addition, Olson and his coworkers suggested that the propionates were not tightly bound to the polar part of the heme pocket, because the hemin dissociation property for myoglobin reconstituted with the protohemin IX-dimethyl ester was very similar to that observed for the native protein [22]. However, in the case of rMb(**1**) and rMb(**2**), the author can clearly show that the ionic interaction, i.e., propionate binding to the polar residues, partially stabilizes the hemin in the protein matrix, whereas there is no significant difference in the $pK_{1/2}$ values between rMb(**1**) and rMb(**2**).

To evaluate the apparent hemin affinity for apomyoglobin, titrimetric measurements were carried out by monitoring the spectral changes of the hemins upon the addition of the apoprotein in 100 mM potassium phosphate buffer solutions containing 5% pyridine at 25 °C. Each spectrum was obtained after equilibrium of the hemin insertion into the apoprotein occurred (over 30 min). From the spectral changes of the Soret maxima to the 408 nm red-shift with several clear isosbestic points, the apparent free energy changes of the hemin binding for the apoprotein were determined. The ΔG°_{app} values for **1** and **2** are −7.2 ± 0.2 and −7.5 ± 0.2 kcal/mol, respectively, indicating that the replacement of one of the two heme-propionates with a methyl group leads to an unfavorable positive shift of ΔG°_{app} within $\Delta\Delta G^{\circ}$ = 1.1 and 0.8 kcal/mol. Based on these results, the author can roughly estimate that two heme-propionate side chains contribute a factor of 10–15% to the overall binding affinity of the native hemin for the protein matrix [23–25].

1-5. Summary

The study presented in this chapter is the first experimental evidence for clearly demonstrating the contribution of two propionates to the stabilization of the hemin in myoglobin. In contrast, no significant difference in the binding property between the 6- and 7-propionates with the corresponding amino acid residues can be detected.

References

1. Turano, P., and Lu, Y. (2001) in *Handbook on Metalloproteins* (Bertini, I., Sigel, A., and Sigel, H., Eds.) Chap. 9, pp 269–356, Marcel Dekker, New York.
2. Takano, T. (1977) Structure of myoglobin refined at 2.0 Å resolution: I. Crystallographic refinement of metmyoglobin from sperm whale, *J. Mol. Biol. 110*, 537–568.
3. Kendrew, J. C., Bodo, G., Dintzis, H. M., Parrish, R. G., Wyckoff, H., and Phillips, D. C. (1958) A three-dimensional model of the myoglobin molecule obtained by X-ray analysis, *Nature 181*, 662–666.
4. (a) La Mar, G. N., Pande, U., Hauksson, J. B., Pandey, R. K., and Smith, K. M. (1989) Proton nuclear magnetic resonance investigation of the mechanism of the reconstitution of myoglobin that leads to metastable heme orientational disorder, *J. Am. Chem. Soc. 111*, 485–491. (b) Hauksson, J. B., La Mar, G. N., Pandey, R. K., Rezzano, I. N., and Smith, K. M. (1990) Proton NMR study of the role of individual heme propionates in modulating structural and dynamic properties of the heme pocket in myoglobin, *J. Am. Chem. Soc. 112*, 6198–6205.
5. Hayashi, T., Matsuo, T., Hitomi, Y., Okawa, K., Suzuki, A., Shiro, Y., Iizuka, T., Hisaeda, Y., and Ogoshi, H. (2002) Contribution of heme-propionate side chains to structure and function of myoglobin: Chemical approach by artificially created prosthetic groups, *J. Inorg. Biochem. 91*, 94–100.
6. Smith, K. M., and Craig, G. W. (1983) Porphyrin synthesis through tripyrrins: An alternate approach, *J. Org. Chem. 48*, 4302–4306.
7. The ratio of two different heme orientations at equilibrium in the heme pocket were determined to be approximately 20:1 for both reconstituted myoglobins [4].
8. Teale, F. W. J. (1959) Cleavage of the haem-protein link by acid methylethylketone, *Biochim. Biophys. Acta 35*, 543.
9. Lloyd, E., Burk, D. L., Ferrer, J. C., Maurus, R., Doran, J., Carey, P. R., Brayer, G. D., and Mauk, A. G. (1996) Electrostatic modification of the active site of myoglobin: Characterization of the proximal Ser92Asp variant, *Biochemistry 35*, 11901–11912.
10. Smith, K. M., and Minnetian, O. M. (1986) Cyclization of 1',8'-dimethyl-*a,c*-biladiene salts to give porphyrins: A study with various oxidizing agents, *J. Chem. Soc. PERKIN TRANS. 1* 277–280.
11. (a) Clewlow, P. J., and Jackson, A. H. (1990) Synthesis and characterisation of the C_{30}-de-ethylaetioporphyrin present in petroleum, *J. Chem. Soc. PERKIN TRANS. 1* 1925–1936. (b) Cavaleiro, J. A. S., Gonsalves, A. M. d'A. R., Kenner, G. W., and Smith, K. M. (1973) Pyrroles and related compounds. Part XXII. Syntheses of pyrromethanes and tripyrrane, *J. Chem. Soc. PERKIN TRANS. 1* 2471–2485. (c) Cavaleiro, J. A. S., Gonsalves, A. M. d'A. R., Kenner, G. W., and Smith, K. M. (1974) Pyrroles and related compounds. Part XXIII. Total syntheses of deuteriated Derivatives of protoporphyrin-IX for nuclear magnetic resonance studies of haemoproteins, *J. Chem. Soc. PERKIN TRANS. 1* 1771–1781. (d) Baptista de Almeida, J. A. P., Kenner, G. W., Rimmer, J., and Smith, K. M. (1976) Pyrroles and related compounds–XXXV. A stepwise, general synthesis of unsymmetrically

substituted porphyrins, *Tetrahedron 32*, 1793–1799.

12. Antonini, E., and Brunori, M. (1971) "*Hemoglobin and Myoglobin in Their Reactions with Ligands*", North-Holland, Amsterdam.
13. Lemberg, R., and Barrett, J. (1973) "*Cytochromes*", Academic Press, London.
14. Gajhede, M. (2001) in *Handbook of Metalloproteins* (Messerschmidt, A., Huber, R., Poulos, T., and Weighardt, K., Eds.) Vol. 1, pp 195–210, John Wiley & Sons, Chichester, U.K.
15. Nichols, P., Fita, I., and Loewen, P. C. (2001) Enzymology and Structure of Catalases. in *Advances in Inorganic Chemistry* (Sykes, A. G., and Mauk, G., Eds.) Vol. 51, pp 51–106, Academic Press, New York.
16. (a) Smith, K. M. (1979) Protoporphyrin IX: Some recent research, *Acc. Chem. Res. 12*, 374–381. (b) La Mar., G. N., Emerson, S. D., Lecomte, J. T. J., Pande, U., Smith, K. M., Craig, G. W., and Kehres, L. A. (1986) Influence of propionate side chains on the equilibrium heme orientation in sperm whale myoglobin. Heme resonance assignments and structure determination by nuclear Overhauser effect measurement, *J. Am. Chem. Soc. 108*, 5568–5573. (c) La Mar, G. N., Budd, D. L., Viscio, D. B., Smith, K. M., and Langry, K. C. (1978) Proton nuclear magnetic resonance characterization of heme disorder in hemoprotein, *Proc. Natl. Acad. Sci. USA 75*, 5755–5759.
17. (a) Smith, K. M., Eivazi, F., Langry, K. C., Baptista de Almeida, J. A. P., and Kenner, G. W. (1979) New Syntheses of Deuterated Protoporphyrin-IX Derivatives for Heme Protein nmr Studies, *Bioorg. Chem. 8*, 485–495. (b) Smith, K. M., and Minnetian, O. M. (1985) Novel porphyrins from copper(II)-mediated cyclizations of 1',8'-dimethyl-a,c-biladiene salts: Mechanism of the cyclization reaction, *J. Org. Chem. 50*, 2073–2080. (c) Smith, K. M., and Pandey, R. K. (1985) Syntheses of isomers of protoporphyrin-IX with permuted propionic side-chains, *J. Heterocyclic Chem. 22*, 1041–1044. (d) Smith, K. M., and Pandey, R. K. (1983) New efficient total syntheses of derivatives of protoporphyrin-IX bearing deuteriated methyl groups, *J. Heterocyclic Chem. 20*, 1383–1388. (e) Smith, K. M., Fujinari, E. M., Langry, K. C., Parish, D. W., and Tabba, H. D. (1983) Manipulation of vinyl groups in protoporphyrin IX: Introduction of deuterium and carbon-13 labels for spectroscopic studies, *J. Am. Chem. Soc. 105*, 6638–6646.
18. Rossi-Fanelli, A., and Antonini, E. (1957) Reversible splitting of human myoglobin. Physico-chemical properties and oxygen equilibrium of reconstituted proto- and deuteromyoglobin, *Arch. Biochem. Biophys. 72*, 243–246.
19. Hayashi, T., and Hisaeda, Y. (2002) New functionalization of myoglobin by chemical modification of heme-propionates, *Acc. Chem. Res. 35*, 35–43.
20. (a) Tsukaraha, K., Okazawa, T., Takahashi, H., and Yamamoto, Y. (1986) Kinetics of reduction of metmyoglobins by ascorbate. Effect of the modification of the heme distal side, heme propionates, and 2,4-substituents of deuterohemin, *Inorg. Chem. 25*, 4756–4760. (b) Tamura, M., Woodrow, G. V., and Yonetani, T. (1973) Heme-modification studies of myoglobin : II. Ligand binding characteristics of ferric and ferrous myoglobins containing unnatural hemes, *Biochim. Biophys. Acta 317*, 34–49.
21. Hargrove, M. S., Barrick, D., and Olson, J. S. (1996) The association rate constant for heme binding to

globin is independent of protein structure, *Biochemistry 35*, 11293–11299.

22. Hargrove, M. S., Wilkinson, A. J., and Olson, J. S. (1996) Structural factors governing hemin dissociation from metmyoglobin, *Biochemistry 35*, 11300–11309.
23. It is known that the real affinity of the hemin for apomyoglobin is greater than 10^{10} M^{-1} ($\Delta G° < -13$ kcal/mol). In the present study, the hemin was dissolved in pyridine/buffer solution, because of the hemin solubility. Thus, the apparent binding constants would involve the dissociation factor of the coordinated pyridine from the hemin. However, assuming that the pyridine binding to **1** and **2** are the same as that of the native hemin, the difference in the free energy changes between the native and reconstituted myoglobins can be discussed.
24. La Mar and coworkers have reported that the 6-propionate interaction with Arg45 is stronger by ca. 0.4 kcal/mol than the 7-propionate interaction with Ser92 and His97 [4(b)].
25. Santucci, R., Ascoli, F., La Mar, G. N., Pandey, R. K., and Smith, K. M. (1993) Reconstitution of horse heart myoglobin with hemins methylated at 6- or 7-positions: A circular dichroism study, *Biochim. Biophys. Acta. 1164*, 133–137.

Chapter 2

Structure and Ligand Binding Properties of Myoglobins Reconstituted with Monodepropionated Heme: Functional Role of Each Heme Propionate Side Chain

2-1. Introduction

Protoheme IX (heme *b*), one of the prosthetic groups in a series of hemoproteins, is tightly bound in the protein matrix by multiple noncovalent interactions. For the O_2-binding hemoproteins, such as myoglobin and hemoglobin, the heme is stabilized by Fe–His coordination, hydrophobic contact of the heme with several nonpolar aliphatic and aromatic amino acid residues, and the formation of a salt bridge between the heme propionate side chains and polar amino acid residues near the entrance of the heme pocket [1]. Structures of the proteins determined by an X-ray crystallographic analysis and an NMR spectroscopic study of the myoglobin clearly showed the heme–globin interaction. In addition, the kinetic and thermodynamic studies of the heme binding to the apoprotein have provided important insight into understanding of the contribution of each interaction to the stabilization of the heme–globin complex [2]. It is known that the overall binding affinity of apomyoglobin for hemin is approximately 10^{12}–10^{14} M^{-1}, and the propionate–amino acid residue interactions contribute a factor of 10^2–10^4 M^{-1} to the overall affinity. In particular, the previous kinetic studies of the dissociation of heme from horse heart myoglobin suggest that the interactions between the two heme propionate side chains and polar amino acids such as Lys45, Ser92 and His97 contribute to the stabilization of the heme molecule in the globin [3]. My next subject has been to elucidate the relationship between the heme–globin interaction and its physiological function [4 and references cited therein].

The three-dimensional (3D) structural analysis of sperm whale myoglobin indicates that the two propionate side chains linked at the 6 and 7 positions of the heme framework interact with Arg45 and Ser92/His97, respectively. According to the crystal structure of oxymyoglobin as shown in Figure 2-1, it displays two unique networks [5, 6]. One is the distal site network of the 6-propionate–Arg45–H_2O–His64–bound O_2. The other is the proximal site network of 7-propionate–Ser92–His93. These hydrogen bonding networks seem to be essential to regulation of the myoglobin function, because the former network stabilizes the bound O_2 and the latter may control the position of the imidazole ring as an axial ligand of His93. Although it is unambiguous that each heme propionate side chain is a part of the hydrogen bonding networks, their contribution to the myoglobin function has not been completely determined.

As described in chapter 1 of this thesis, the author prepared the prototype one-legged protohemins, **1** and **2** (Figure 2-2) by the modified Smith's synthetic method [7]. The structures of the reconstituted proteins, rMb(**1**) and rMb(**2**), reconstituted with the prototype one-legged protohemins, **1** and **2**, respectively, were evaluated by a Raman spectroscopic method and an X-ray crystallographic analysis. Moreover, the kinetic parameters of the O_2 and CO binding for the two reconstituted myoglobins were compared to those of the myoglobin rMb(**3**) with the native protoheme IX (**3**). On the basis of these results, it was found that

the 6-propionate side chain is crucial for stabilization of the O_2 complex, whereas the CO binding is affected by the removal of the 7-propionate side chain. In this chapter, the author summarizes the structure and physicochemical properties of the myoglobins reconstituted with the one-legged hemes and discuss the role of each heme propionate side chain in ligand binding events.

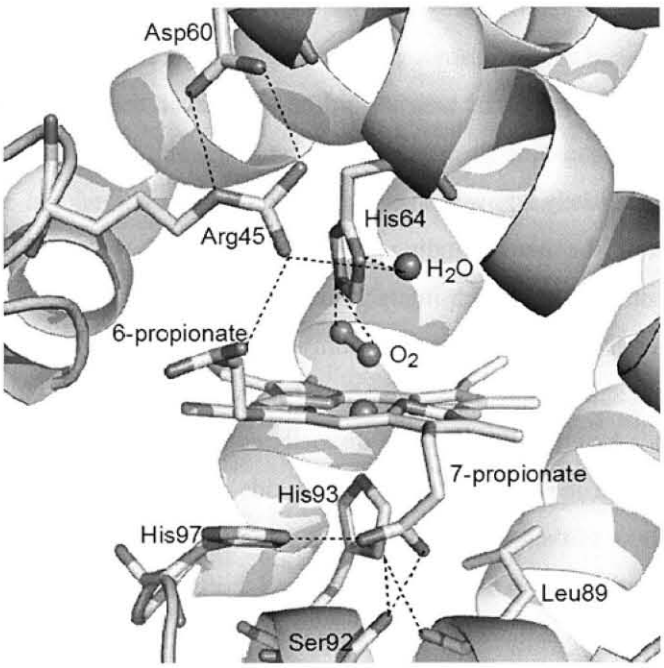

Figure 2-1. Hydrogen bonding network in the proximal and distal sites of sperm whale oxymyoglobin (PDB ID: 1MBO)

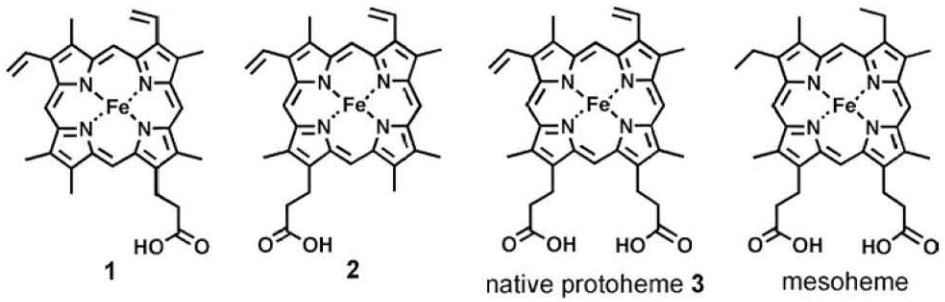

Figure 2-2. Structures of one-legged hemes **1** and **2**, protoheme IX **3**, and mesoheme.

2-2. Experimental Section

2-2-1. Instruments

The UV–visible experiments were conducted using a Shimadzu UV-3150 double beam spectrophotometer equipped with a thermostated cell holder with a 0.1 °C deviation. Purification of the proteins was performed with an Amersham Biosciences ÄKTA FPLC system with a Frac-920 fraction collector at 4 °C. The mass analysis of the myoglobins was carried out using a TOF mass spectrometer equipped with electrospray ionization on an Applied Biosystems Mariner API-TOF workstation. The spectroelectrochemical measurement was performed by regulating the potentials using a Hokuto Denko HA-305 potentiostat/galvanostat. The IR spectra of the CO-ligated Mbs were recorded using a JASCO FT/IR-620 spectrometer. The equipment for resonance Raman spectroscopy and X-ray crystallographic analysis is described bellow. Kinetic measurements of O_2 and CO binding were carried out using a stopped-flow/laser-flash photolysis system constructed by Unisoku, Co., Ltd. (Osaka, Japan). A Xe arc lamp was employed as the source of the probe light to follow the spectral changes. For laser-flash photolysis, a sample was excited with 5 ns pulses (532 nm) from a Q-switched Nd:YAG laser (Surelite I, Continuum). The pH values were monitored with a Beckman Φ71 pH meter.

2-2-2. Materials

The native sperm whale myoglobin was purchased from Biozyme Laboratories, Ltd and purified by passing through a CM-52 (Whatman) column. All reagents of the highest guaranteed grade available were obtained from commercial sources and were used as received unless otherwise indicated. Distilled water was demineralized with a Millipore Milli-Q Academic A10 apparatus. The proteins were purified by column chromatography through a CM-52 (Whatman), Sephadex G-25 (Amersham Biosciences), Hi-Trap Desalting (Amersham Biosciences), and/or Superdex 75 (Amersham Biosciences) column. The one-legged hemins **1** and **2** were synthesized by the method described in chapter 1 of this thesis [7]. The native protohemin IX (**3**) was purchased from Tokyo Chemical Industry Co., Ltd. The reconstituted myoglobins, rMb(**1**), rMb(**2**) and rMb(**3**) were prepared by the method described in chapter 1 of this thesis.

2-2-3. Methods

Determination of Fe^{2+}/Fe^{3+} redox potentials. The spectroelectrochemical measurements were carried out at 25 °C under an N_2 atmosphere using an optically transparent thin-layer electrode cell (optical path length of 0.6 mm). A working electrode and a counter electrode made of Pt mesh were used along with an Ag/AgCl reference electrode. The potentials of these electrodes were controlled and measured with a Hokuto Denko HA-305 potentiostat/galvanostat. A solution of metmyoglobin (50 μM) was prepared in 100 mM potassium phosphate buffer (pH 7.0) containing $Ru(NH_3)_6Cl_3$ (100 μM, E = 51 mV vs. NHE) as an electron mediator. A typical increment of 25 mV was applied to the system, and at each applied

potential, the electronic absorption spectra were monitored until no change was detected due to the establishment of equilibrium. The spectra of the fully reduced and fully oxidized myoglobins were obtained by applying the potentials of −500 and +200 mV versus Ag/AgCl. The data were fitted to the Nernst equation, and the resulting midpoint of the redox potential was referenced to the normal hydrogen electrode (NHE).

^{1}H NMR spectra of deoxymyoglobins. A small amount (5 vol.%) of deuterated 10 mM potassium phosphate buffer (pD 7.4) containing $Na_2S_2O_4$ (1 M) was added to a solution of metmyoglobin (1 mM) in 10 mM potassium phosphate buffer (pH 7.0). The solution was put into a 5 mm tube (SHIGEMI Co. Ltd.) with blowing N_2. The measurement of ^{1}H NMR spectra were carried out at 298 K with a Brucker 500 MHz NMR spectrometer (AMX 500) equipped with a 5 mm BBI probe (^{1}H-BB XYZ-GRD 8375/45). The ^{1}H NMR chemical shift values are indicated in ppm relative to 2,2'-dimethyl-2-silapentane-5-sulfonate (DSS). The residual water signal was suppressed by using a H_2O presaturation pulse program. NMR spectrometer conditions were as follows: pulse program is zgpr, window function is arranged by qsim mode, acquisition time 0.13 s, pulse delay time 0.10 s.

Measurement of resonance Raman spectroscopy. A 25 μL solution of 0.4 mM metmyoglobin in 100 mM potassium phosphate buffer (pH 7.0) was transferred to an airtight spinning cell. The solution was diluted with 65 μL of 100 mM potassium phosphate buffer (pH 7.0), and three repeated evacuations of the gas inside the cell were followed by the introduction of N_2. A small amount of N_2-saturated dithionite solution (10 mM, 10 μL) was added to prepare the deoxymyoglobin. The CO adduct of the myoglobin (CO-myoglobin) was formed through two repeated evacuations of the gas inside the cell followed by the introduction of N_2 and finally the incorporation of $^{12}C^{16}O$ (or $^{13}C^{18}O$) before a small amount (10 mM, 10 μL) of N_2-saturated dithionite solution was added. The Raman scattering was excited at 441.6 nm (12 mW) by a He/Cd laser for the deoxymyoglobin and at 413.1 nm (10 mW) by a Kr^+ laser for the CO-myoglobin. The Raman shifts were calibrated with toluene and CH_2Cl_2.

Measurement of IR spectroscopy. The IR spectra of the CO-myoglobins were recorded with a JASCO FT/IR-620 spectrometer with a 1.0 cm^{-1} resolution for the frequency shift at room temperature. A cell using CaF_2 windows with a 0.1 mm optical path length was used. The background spectrum was collected for the corresponding deoxymyoglobins. The observed spectra were deconvoluted into two components with a half-width of 6 cm^{-1}.

Crystallization and structure determination. The purified protein in 10 mM phosphate buffer (pH 7.0) was concentrated by centrifugation to 36 and 18 mg/mL for the met-rMb(**1**) and met-rMb(**2**) crystallizations, respectively. Crystals of the ferric form were grown using the sitting-drop vapor-diffusion method. A 1 μL protein solution was added to a 1 μL reservoir solution and equilibrated against a 100 μL reservoir solution. A crystal of met-rMb(**1**) was obtained in 3.0 M ammonium sulfate

and 0.1 M Bis-Tris-propane at pH 6.4 and 4 °C. The crystal of met-rMb(**2**) was obtained in 3.1 M ammonium sulfate and 0.1 M Bis-Tris-propane at pH 6.4 and 17 °C. The crystals were soaked in cryoprotectant solution (10% glucose and 10% xylitol in reservoir solution) and flash-frozen in liquid nitrogen. The X-ray diffraction data were collected at BL44B2 or BL45XU in SPring-8, Hyogo, Japan. The data were integrated and merged using the program HKL2000 [8]. The data collection and refinement statistics are listed in Table 2-1. The initial phases of the rMb(**1**) and rMb(**2**) crystals were obtained by the molecular replacement method using the native myoglobin (PDB entry 1JW8 or 1A6K) as a search model. The 5% randomly selected reflections were selected as test reflections for use in the free *R* cross-validation method throughout the refinement [9]. The initial model was refined by simulated annealing using CNS [10]. The multiple rounds of manual model rebuilding and positional and individual *B*-factor refinements allowed placement of the water molecules and assignment of some alternate side chain conformations. The solvent molecules were included, if they had a good stereochemistry and reasonable density in the F_o-F_c and $2F_o-F_c$ map. Subsequent refinement was performed with SHELXL [11]. All the hydrogen atoms were added according to the geometrical criteria. After introduction of anisotropic *B*-factors, further alternate conformations and water molecules could be modeled. The initial run of SHELX was performed using the parameter of the heme group of 1A6K for the protoheme of rMb(**1**) or rMb(**2**). The restraints on the protoheme were gradually removed, and the final stages of refinement restrained only the bond length and bond angles of the propionate as previously described [6]. The root-mean-square deviations in the superposition were calculated for 140 pairs of Cα atoms of residues 2–116 and 124–148 using the program LSQKAB [12], because the structures of the N- and C-terminal residues are flexible and the structure of residues 117–123 (GH corner) has a high pH dependency, as reported by Yang et al. [13]. The figures were created with Pymol, Molscript, and Raster3D [14–16]. The atomic coordinates and structure factors have been deposited in the Protein Data Bank (entries 2EKT and 2EKU for aquometmyoglobins reconstituted with 6-depropionated and 7-depropionated protohemin IX species, respectively).

Table 2-1. Data collection and refinement statistics

	rMb(**1**)	rMb(**2**)
Data collection		
X-ray source	SPring-8 BL44B2	SPring-8 BL45XU
Detector	ADSC Quantum 210	RIGAKU R-axis V
Wavelength (Å)	0.78	1.0
Resolution (Å)	50–1.10 (1.14–1.10)	50–1.40 (1.45–1.40)
Space group	*P*6	$P2_1$
Unit cell parameters (Å)	$a = b = 90.2$, $c = 45.3$	$a = 63.8$, $b = 30.5$, $c = 34.4$, $\beta = 105.5°$
Number of observations	2005844	167220
Number of unique reflections	85421	25369
Completeness (%)	100 (100)	100 (99.7)
R_{sym} (%)	6.2 (34.9)	5.2 (32.0)
$I/\sigma(I)$	38.7 (6.8)	25.6 (6.8)
Refinement		
Resolution (Å)	10–1.1	10–1.4
Total reflections	81016	24010
Number of non-H atoms		
Protein	1264	1246
Water	303	204
Other	59	54
R_{cryst} (%)	13.3	12.7
R_{free} (%)	15.8	19.5
R.m.s.d. from target		
Bond lengths (Å)	0.014	0.014
Angle distances (Å)	0.030	0.030
Mean isotropic equivalent *B*-factor (Å^2)		
All protein atoms	12.8	14.6
Main chain atoms	10.3	11.7
Side chain atoms	15.4	17.4
Water molecules	26.9	27.6
Protoheme	8.6	10.0
Sulfate ions	29.0	17.6

O_2 binding of myoglobins. The oxymyoglobins were prepared by exposure of the deoxy form to air. The formation of the oxygenated form was confirmed by the UV–vis spectral changes. The association of O_2 was observed by the absorbance change at 435 nm after flash photolysis of the oxy form under 1 atm of O_2 at 25 °C. The time course of the absorbance was analyzed by single-phase kinetics to give the pseudo-first-order rate constant. By dividing this value by the O_2 concentration ($[O_2] = 2.64 \times 10^{-4}$ M), the association rate constant was obtained. The dissociation of O_2 was assessed by following the UV–vis spectral changes after rapidly mixing the oxygenated form with excess $K_3[Fe(CN)_6]$ using a stopped-flow apparatus. The O_2 affinity was calculated from the ratio of the association and dissociation rates. The O_2 dissociation measurements of oxymyoglobins were performed by $K_3[Fe(CN)_6]$-mediated oxidation method and the reaction is expressed in eq. 2-1.

$$MbO_2 \underset{k^{O2}_{on}}{\overset{k^{O2}_{off}}{\rightleftharpoons}} O_2 + \text{deoxy-Mb} + K_3[Fe(CN)_6] \xrightarrow{k_{ox}} \text{met-Mb} \qquad (2\text{-}1)$$

where k^{O2}_{on} is association rate constant for binding of O_2; k^{O2}_{off} is corresponding dissociation rate constant; k_{ox} is oxidation rate constant of deoxymyoglobin to metmyoglobin. Under a steady-state assumption, the reaction will follow first order kinetics and the observed rate constant (k_{obs}) is written by eq. 2-2.

$$k_{obs} = \frac{k^{O2}_{off}\, k_{ox}[K_3[Fe(CN)_6]]}{k_{ox}[K_3[Fe(CN)_6]] + k^{O2}_{on}[O_2]} = \frac{k^{O2}_{off}}{1 + k^{O2}_{on}[O_2] / k_{ox}[K_3[Fe(CN)_6]]} \qquad (2\text{-}2)$$

If $k_{ox}[K_3[Fe(CN)_6]] >> k^{O2}_{on}[O_2]$, eq. 2-2 converts to eq. 2-3.

$$k_{obs} = k^{O2}_{off} \qquad (2\text{-}3)$$

CO binding of myoglobins. The CO-myoglobins were obtained by reduction with a slight excess of sodium dithionite under a CO atmosphere. The formation of the CO-bound form was confirmed by the UV–vis spectral changes. The associations of CO were observed by the absorbance change at 423 nm after flash photolysis of the CO form under 1 atm of CO at 25 °C. The time course of the absorbance was analyzed by single-phase kinetics to give the pseudo-first-order rate constant. By dividing this value by the CO concentration ([CO] = 9.85×10^{-4} M), the association rate constant was obtained. The extents of dissociation of CO from the CO-bound myoglobins were measured by displacement with NO. A solution of the CO-bound myoglobins was mixed with the NO-saturated buffer by a stopped-flow apparatus, and the decrease in absorbance at 423 nm was monitored at 25 °C. The CO dissociation measurement of carbonmonoxymyoglobin was performed by NO-displacing method and the reaction is expressed in eq. 2-4.

$$\text{MbCO} \underset{k^{\text{CO}}_{\text{on}}}{\overset{k^{\text{CO}}_{\text{off}}}{\rightleftharpoons}} \text{CO} + \text{deoxy-Mb} + \text{NO} \underset{k^{\text{NO}}_{\text{off}}}{\overset{k^{\text{NO}}_{\text{on}}}{\rightleftharpoons}} \text{MbNO} \qquad (2\text{-}4)$$

where $k^{\text{CO}}_{\text{on}}$ and $k^{\text{NO}}_{\text{on}}$ are association rate constants for the binding of CO and NO, respectively; $k^{\text{CO}}_{\text{off}}$ and $k^{\text{NO}}_{\text{off}}$ are corresponding dissociation rate constants, respectively. Under a steady-state assumption, the reaction will follow first order kinetics and the observed rate constant (k_{obs}) is written by eq. 2-5.

$$k_{\text{obs}} = \frac{k^{\text{CO}}_{\text{off}} k^{\text{NO}}_{\text{on}}[\text{NO}] + k^{\text{NO}}_{\text{off}} k^{\text{CO}}_{\text{on}}[\text{CO}] + k^{\text{CO}}_{\text{off}} k^{\text{NO}}_{\text{off}}}{k^{\text{NO}}_{\text{on}}[\text{NO}] + k^{\text{CO}}_{\text{on}}[\text{CO}] + k^{\text{NO}}_{\text{off}}} \qquad (2\text{-}5)$$

In the case of myoglobins, NO exhibits much smaller dissociation rate and higher affinity than originally bound CO. Thus, $k^{\text{CO}}_{\text{off}} >> k^{\text{NO}}_{\text{off}} \approx 0$ and eq. 2-5 converts to eq. 2-6.

$$k_{\text{obs}} = \frac{k^{\text{CO}}_{\text{off}} k^{\text{NO}}_{\text{on}}[\text{NO}]}{k^{\text{NO}}_{\text{on}}[\text{NO}] + k^{\text{CO}}_{\text{on}}[\text{CO}]} = \frac{k^{\text{CO}}_{\text{off}}}{1 + k^{\text{CO}}_{\text{on}}[\text{CO}] / k^{\text{NO}}_{\text{on}}[\text{NO}]} \qquad (2\text{-}6)$$

If $k^{\text{NO}}_{\text{on}}[\text{NO}] >> k^{\text{CO}}_{\text{on}}[\text{CO}]$, eq. 2-6 converts to eq. 2-7.

$$k_{\text{obs}} = k^{\text{CO}}_{\text{off}} \qquad (2\text{-}7)$$

Autoxidation for oxygenated myoglobins. Although the mechanism of the autoxidation reaction from oxymyoglobin to metmyoglobin has never been completely clear, both the unimolecular HO_2 dissociation mechanism and bimolecular reaction mechanism are proposed, and each pathway depends on the O_2 concentration. In air equilibrated buffer at 37 °C, the proposed dominant mechanism is unimolecular HO_2 dissociation. In general, in spite of the multiple step reaction, the spectral changes in the autoxidation process exhibit several isosbestic points, that is, the oxy and met forms are only observed by electronic absorption spectroscopic studies. Therefore, the observed time course can be represented by a simple first order process, and the autoxidation rate constant is obtained by linear fitting to eq. 2-8.

$$\ln(\Delta A) = -k_{auto}t \qquad (2\text{-}8)$$

where ΔA is difference in absorbance from met form; k_{auto} is autoxidation rate constant; t is reaction time. Autoxidations for the oxygenated myoglobins were monitored by absorbance changes in the range of 500−700 nm every 8 min for oxygenated rMb(**1**) and every 40 min for the oxygenated rMb(**2**) and rMb(**3**) at 37 °C under aerobic conditions. The time course of the absorbance at 580 nm was analyzed by first-order kinetics to afford the autoxidation rate.

2-3. Results

Preparation and characterization of reconstituted myoglobins. Insertion of hemins **1**–**3** into the sperm whale apomyoglobin was carried out by a conventional method as described in chapter 1 of this thesis. In a series of these studies except for the X-ray crystallographic analysis, the author used the myoglobin rMb(**3**) reconstituted with the native prosthetic group, protohemin IX (**3**), as the reference protein instead of the native myoglobin, because of the reducing experimental artifacts.

The reconstituted ferrous myoglobins were obtained by dithionite reduction. The reversibility of the O_2 and CO bindings for the deoxymyoglobins is similar to those observed in the native myoglobin and rMb(**3**). The spectra of a series of rMb(**1**)s are exactly the same as those for the native myoglobin and rMb(**3**). In contrast, the Soret bands of met-rMb(**2**), deoxy-rMb(**2**), and CO-rMb(**2**) were always shifted by 1 nm compared to those of the native myoglobin and rMb(**3**) with a good reproducibility, suggesting that the removal of the 7-propionate side chain slightly perturbs the electronic structure of the heme plane. The absorption maxima for the various species of the myoglobins are summarized in Table 2-2.

Table 2-2. Absorption maxima for myoglobins[a]

	λ_{max} (nm)			
protein	met-Mb	deoxy-Mb	oxy-Mb	CO-Mb
rMb(**1**)	408, 503, 630	432, 557	417, 543, 581	422, 541, 577
rMb(**2**)	407, 504, 630	431, 557	417, 542, 580	421, 541, 576
rMb(**3**)	408, 504, 630	432, 557	417, 543, 581	422, 541, 577

[a] pH 7.0 (100 mM potassium phosphate buffer) and 25 °C.

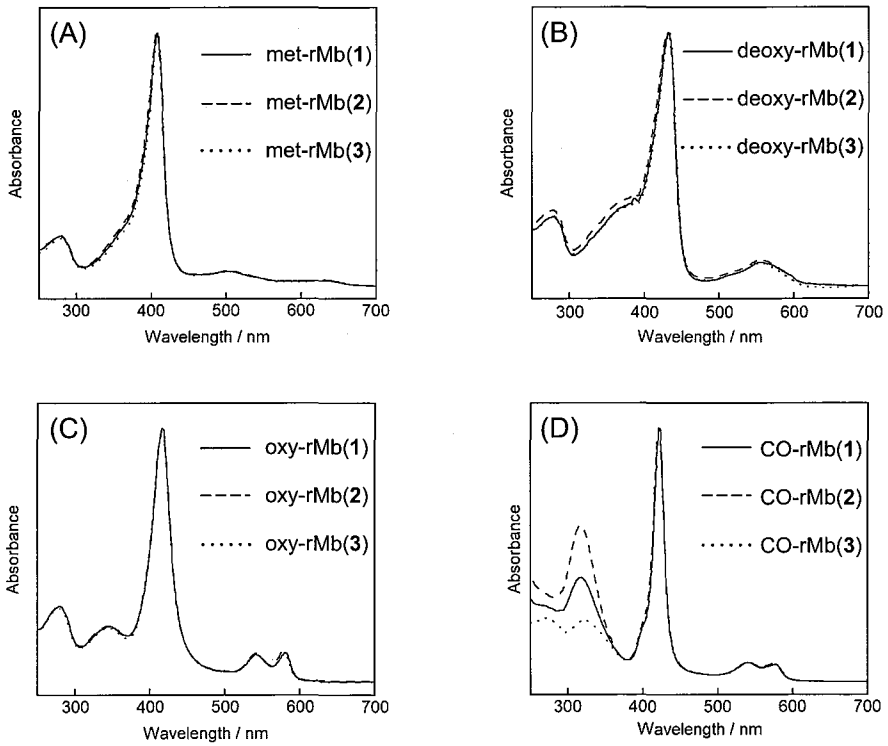

Figure 2-3. Absorption spectra of myoglobins in 100 mM potassium phosphate buffer (pH 7.0) at 25 °C. (A) met-Mbs, (B) deoxy-Mbs, (C) oxy-Mbs, (D) CO-Mbs.

Fe^{2+}/Fe^{3+} redox potentials. Figure 2-4 shows the results of the spectroelectrochemical measurements using the thin-layer cell with Pt mesh in the presence of $Ru(NH_3)_6Cl_3$ as an electron mediator. The potentiometric titrations for rMb(**1**) and rMb(**2**) gave similar spectral changes from the ferrous to ferric states to the reference protein rMb(**3**). All proteins exhibited an electrochemically reversible behavior as observed for the native protein between +422 and –278 mV (vs NHE). Table 2-3 summarizes the Fe(II)/Fe(III) redox potentials which were determined by the linear Nernst plots as shown in Figure 2-5. On the basis of the results, it is clear that the removal of the propionates positively shifts the values. One of the main reasons is due to the removal of one negative charge at the terminus of the propionate side chain [17]. In particular, the redox potential of rMb(**1**) is positively shifted by 22 mV compared to that of rMb(**3**), indicating that the lack of the 6-propionate side chain enhances the electron acceptability of the heme iron.

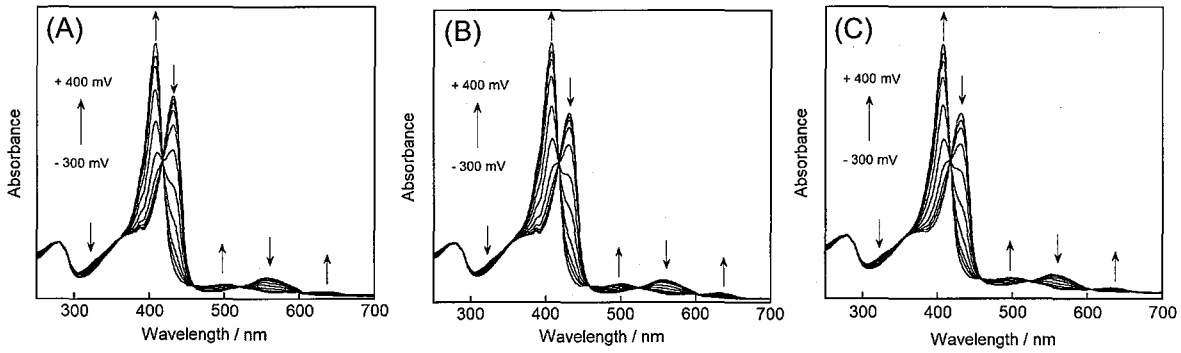

Figure 2-4. UV–vis spectra of Mbs at various applied potentials (vs NHE) during the spectroelectrochemical titration in 100 mM potassium phosphate buffer (pH 7.0) at 25 °C under N_2. (A) rMb(**1**), (B) rMb(**2**), and (C) rMb(**3**)

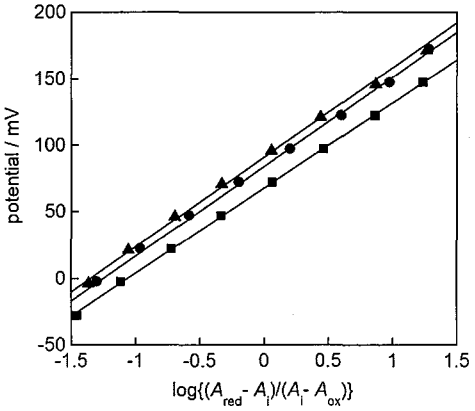

Figure 2-5. Nernst plot obtained from the spectral changes at 433 nm of rMb(**1**) (▲), rMb(**2**) (●), and rMb(**3**) (■).

Table 2-3. Physicochemical parameters for metmyoglobins

protein	pK_a[a]	$E_{1/2}$(mV, vs NHE)[b]
rMb(**1**)	8.67 ± 0.03	91.7 ± 1.0
rMb(**2**)	8.73 ± 0.03	84.6 ± 1.0
rMb(**3**)	8.95 ± 0.03	70.0 ± 0.4

[a] Acid–alkaline equilibrium constants of a heme-bound water molecule, in 100 mM KCl at 25 °C. [b] Redox potentials, Fe(II)/Fe(III). At pH 7.0 and 25 °C.

Resonance Raman spectra of deoxymyoglobins. The heme in myoglobin is attached to the polypeptide chain only through the coordination between His93 and the heme iron. Thus, the nature of the Fe–His93 bond provides valuable information about the reactivity of the heme. In particular, it is well-known that the resonance Raman (RR) spectroscopy is a useful technique for evaluating the coordination property of the heme iron [18]. Figure 2-6 displays the RR spectra in the 180–330 cm^{-1} region for the reconstituted deoxymyoglobins with a 0.25 cm^{-1} resolution for the frequency shift at room temperature [18, 19]. The RR spectrum of rMb(**1**) is definitely close to that of the reference protein rMb(**3**), whereas the ν(Fe–His) Raman band at 221 cm^{-1} for rMb(**2**) is slightly shifted to a higher wavenumber by 1 cm^{-1} compared to that of rMb(**3**). This finding suggests that the lack of the 7-propionate side chain has a slight influence on strengthening the coordination between the heme iron and the imidazole ring of His93.

^{1}H NMR spectra of deoxymyoglobins. Figure 2-7 displays the ^{1}H NMR spectra in the 72–83 ppm region for the reconstituted deoxymyoglobins at 25 °C. A signal with the intensity of one proton was observed at 79.7, 75.8, and 77.4 ppm for rMb(**1**), rMb(**2**), and rMb(**3**), respectively. These signals are assigned to the exchangeable $N^{\varepsilon}H$ proton of His93 [20].

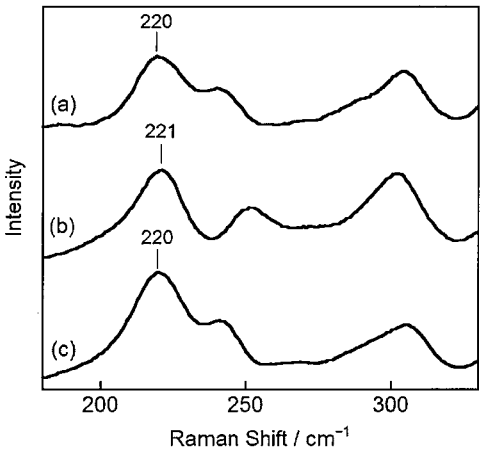

Figure 2-6. Resonance Raman spectra of deoxymyoglobins in the 180–330 cm^{-1} region in 100 mM potassium phosphate buffer (pH 7.0) at room temperature: (a) rMb(**1**), (b) rMb(**2**), (c) rMb(**3**). The excitation wavelength was 441.6 nm and a laser power was 12 mW.

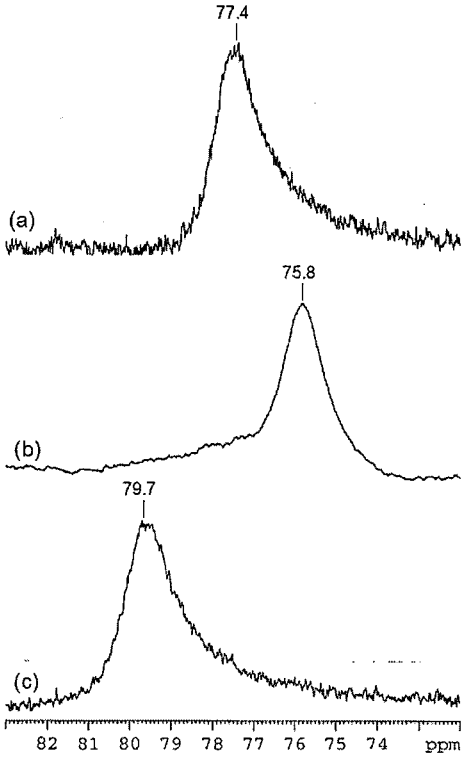

Figure 2-7. ^{1}H NMR spectra of deoxymyoglobins in the 72–83 ppm region in 10 mM potassium phosphate buffer (H_2O/D_2O = 95/5, pH 7.0) at 298 K: (a) rMb(**3**), (b) rMb(**2**), (c) rMb(**1**). The sample concentration was about 1 mM.

Crystal structure of reconstituted myoglobins. The X-ray crystal structures of the hexagonal form of met-rMb(**1**) and the monoclinic form of met-rMb(**2**) have been determined at resolutions of 1.1 and 1.4 Å, respectively. They were crystallized in the aquomet form. The coordinate errors of the structure of rMb(**1**) and rMb(**2**) are estimated from the Luzzati plot to be 0.06 and 0.08 Å, respectively [21]. Figure 2-8 shows that the imidazole of His93 is linked to the Fe(III) atom of protohemin as a fifth ligand, and the water molecule is bound as a sixth ligand, as observed in the aquomet form of the native myoglobin. The electron density maps for the protohemin derivatives did not display an expanded shape of the methyl groups at the 1 and 3 positions of pyrrolic β-carbons. The density of the vinyl groups is very clear to show the peaks for the hydrogen atom in the $F_o - F_c$ map (not shown). These findings suggest the homogeneity of the protohemin orientation. The orientation and the position of the protohemin derivatives and the torsion angles of the remaining propionate side chain are also conserved.

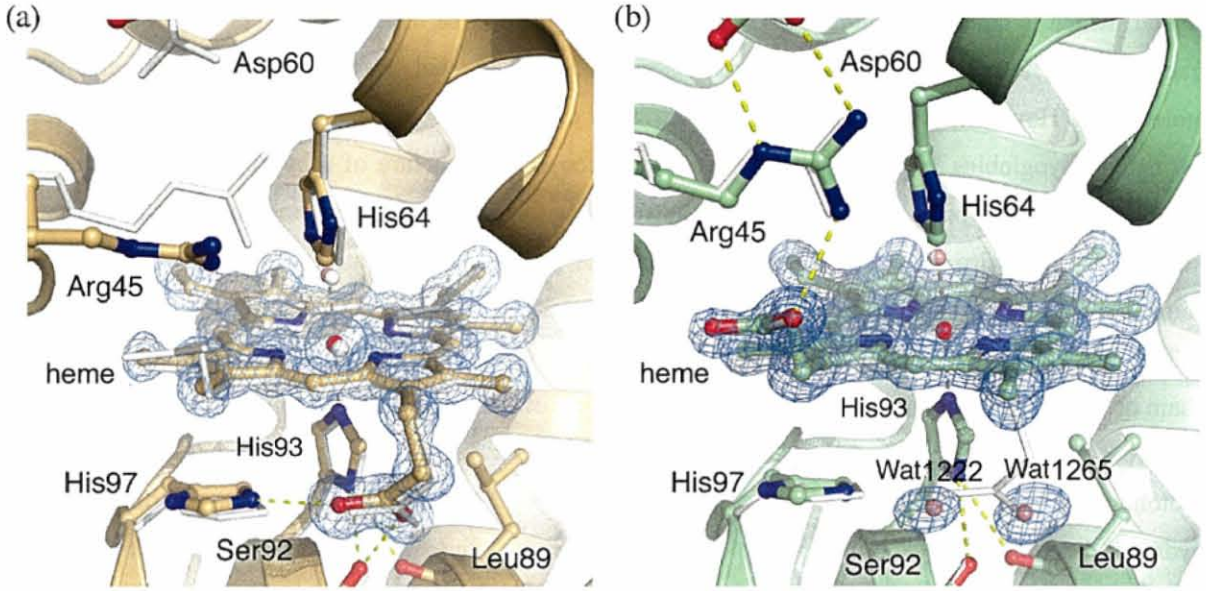

Figure 2-8. Crystal structure of two reconstituted myoglobins. The $2F_{obs}-F_{calc}$ electron density (1.0σ contours) around the one-legged hemin is also shown. (a) Superposition of rMb(**1**) (brown) and native protein (white; 1A6K) structures. (b) Superposition of rMb(**2**) (green) and native protein (white; 1A6K) structures.

Table 2-4. Geometry of one-legged hemins

	rMb(**1**)	rMb(**2**)	wild-type (1A6K)
sample	aquomet	aquomet	aquomet
space group	*P*6	$P2_1$	$P2_1$
resolution (Å)	1.1	1.4	1.1
program	SHELXL	SHELXL	SHELXL
pH of crystal	6.4	6.4	7.0
rmsd of Cα atoms (Å)	0.38 (1A6K)	0.15 (1A6K)	
distance			
His64 Nε–Fe (Å)	4.38	4.37	4.30
Wat O–Fe (Å)	2.06	2.12	2.13
His93 Nε–Fe (Å)	2.03	2.05	2.14
Ser92 Oγ–His93 Nε (Å)	2.94	2.96	2.90
Leu89 O–His93 (Å)	3.05	3.08	2.97

In a detailed comparison, when the structure of rMb(**1**) was superimposed on that of the native myoglobin (1A6K) of the monoclinic crystal using the 140 Cα atoms, the root-mean-square deviation (rmsd) is 0.38 Å [6]. Because rMb(**1**) was crystallized in a hexagonal system, the rmsd value falls to 0.25 Å in the superposition onto the hexagonal (recombinant) native myoglobin (2MBW) [22]. After the structure superposition, the plane of the 6-depropionated protohemin of rMb(**1**) and hemin of the native myoglobin (1A6K) is nearly parallel, and the deviation of the coordinate of the iron atom is 0.23 Å (Figure 2-8(a)). The other geometric parameters of **1** are summarized in Table 2-4. It should be noted that, among the number of sperm whale myoglobin structures in the Proten Data Bank, the hexagonal crystals have been obtained only for the recombinant myoglobin which was expressed in *Escherichia coli.* Since the hexagonal crystal has a large solvent fraction of 59%, the structure of the polypeptide seems to be sensitive to the changes in the pH or temperature of the solvent [13]. On the other hand, the monoclinic crystal, which is commonly obtained for the native protein form of the sperm whale, has a small solvent fraction of 33% and its polypeptide structure seems to be affected by the contact of the neighboring molecules. However, even though they have different crystal packings and different pHs, the structures of the native myoglobins in both crystal forms have a conserved structure of a hydrogen bonding network involving the heme propionate side chains, surrounding residues, and water molecules. Therefore, in Figure 2-9, the hydrogen bonding network around the protohemin derivatives of rMb(**1**) and rMb(**2**) is compared to that of the native protein (1A6K).

The distal hydrogen bonding network of rMb(**1**) has a significant change, since the 6-propionate side chain of the native protein is directed to the distal site to create the salt bridge with the side chains of Arg45 (Figure 2-9(a)). Lack of the 6-propionate side chain causes a 2 Å shift in Arg45 so that it is close to the protohemin plane and disrupts the bridge between Arg45 and Asp60 (Figure 2-9(b)). Furthermore, the hydrogen bonding network of the 6-propionate side chain and four waters (1024, 1058, 1102, and 1149), which have been detected in the native protein (Figure 2-9(a)), are replaced by a row of three waters (1174, 1397, and 1323) in rMb(**1**). These changes might affect the water-mediated interaction between the hemin and main chain of the CD loop (Arg45 N, Asp44 N, and Lys42 O). On the other hand, the structure of the remaining 7-propionate and the hydrogen bonding network of the surrounding waters and protein residues are well-conserved in rMb(**1**).

The crystals of rMb(**2**) and native myoglobin (PDB entry 1A6K) are monoclinic and have very similar unit cell dimensions. These polypeptide structures can be superimposed well with an rmsd of 0.14 Å. The deviation of iron atoms after the superposition is as little as 0.04 Å (Figure 2-8(b)). They have very similar side chain torsion angles and positions in the distal His64 and the proximal His93. The 7-propionate side chain of the native protein is directed to the proximal site and interacts with Ser92, His97 and three waters (1033, 1059, and 1118) (Figure 2-9(a)). Comparison of the distal site of the heme pocket between the native myoglobin and rMb(**2**) (panels (a) and (c) of Figure 2-9) shows no significant structural change in the remaining 6-propionate and hydrogen bonding network. The hydrogen bonding network of the proximal site of rMb(**2**) also exhibits a similar hydrogen bonding network, since the room generated by the lack of the 7-propionate side chain is filled by the two waters which mimic the O atoms of the

propionate side chain that maintains the hydrogen bonds with His97, Ser92 and Wat1033 (Wat1215 of rMb(**2**)). The only difference is that the proximal side of rMb(**2**) cannot order four waters, including Wat1118 and Wat1059 that have been bound to Ser92 in the native protein.

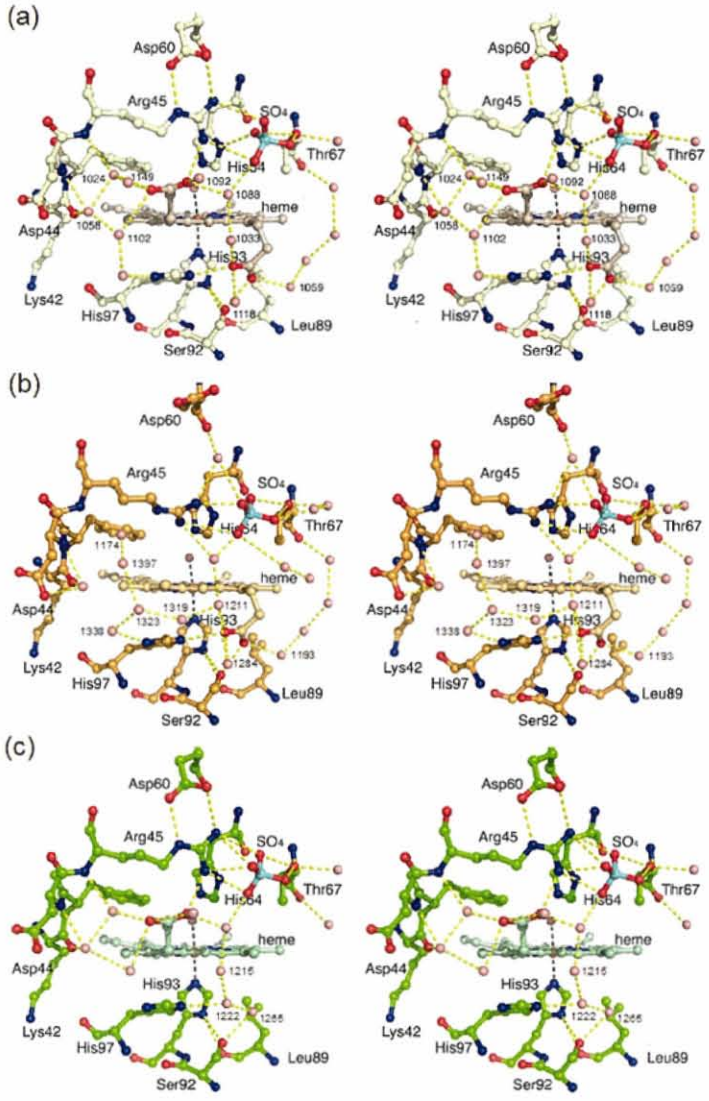

Figure 2-9. Stereoview of the heme pocket region in myoglobins: (a) native protein (1A6K), (b) rMb(**1**), and (c) rMb(**2**).

O_2 and CO binding. As one can clearly see in Table 2-5, the rate constants of the O_2 association for rMb(**1**) and rMb(**2**) are close to that observed for the reference protein rMb(**3**), whereas the dissociation of the O_2 ligand from oxy-rMb(**1**) is approximately 3 times faster than those for rMb(**2**) and rMb(**3**). Furthermore, the autoxidation for oxy-rMb(**1**) is also accelerated, suggesting that the oxygenated rMb(**1**) is less stable rather than those for rMb(**2**) and rMb(**3**). The CO binding behavior of the reconstituted myoglobins is different with the O_2 binding as shown in Table 2-6. The CO dissociation for rMb(**1**) is 1.3-fold faster than that for rMb(**3**). In contrast, rMb(**2**) shows a slightly higher rate constant for CO association and a lower constant for CO dissociation, indicating that the affinity of rMb(**2**) for CO is approximately 2-fold higher than that of rMb(**3**). For the CO binding, the 7-propionate side chain may regulate the binding kinetics.

Table 2-5. O_2 binding parameters for myoglobins[a]

protein	$k^{O2}_{on}(\mu M^{-1}s^{-1})^b$	$k^{O2}_{off}(s^{-1})^c$	$K^{O2}(M^{-1})^d$	$k_{auto}(h^{-1})^e$
rMb(**1**)	19 ± 0.8	59 ± 1.9	3.2×10^5	0.58 ± 0.01
rMb(**2**)	19 ± 0.7	18 ± 0.6	1.1×10^6	0.13 ± 0.01
rMb(**3**)	18 ± 1.1	21 ± 0.6	8.6×10^5	0.10 ± 0.01

[a] pH 7.0 (100 mM potassium phosphate buffer) and 25 °C. [b] Rate constants of O_2 association. [c] Rate constants of O_2 dissociation. [d] O_2 binding affinities are determined by the ratio of k^{O2}_{on} to k^{O2}_{off}. [e] Rate constants for autoxidation from oxymyoglobin to metmyoglobin, at pH 7.0 (100 mM potassium phosphate buffer) and 37 °C.

Table 2-6. CO binding parameters for myoglobins[a]

protein	$k^{CO}_{on}(\mu M^{-1}s^{-1})^b$	$k^{CO}_{off}(s^{-1})^c$	$K^{CO}(M^{-1})^d$	M^e
rMb(**1**)	0.58 ± 0.01	0.070 ± 0.002	8.3×10^6	26
rMb(**2**)	0.86 ± 0.01	0.044 ± 0.004	2.0×10^7	18
rMb(**3**)	0.63 ± 0.01	0.056 ± 0.003	1.1×10^7	13

[a] pH 7.0 (100 mM potassium phosphate buffer) and 25 °C. [b] Rate constants of CO association. [c] Rate constants of CO dissociation. [d] CO binding affinities are determined by the ratio of k^{CO}_{on} to k^{CO}_{off}. [e] K^{CO}/K^{O2} ratio.

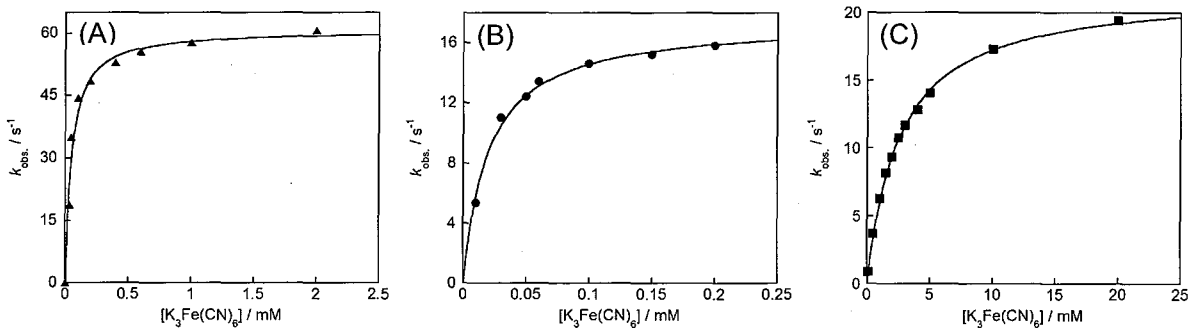

Figure 2-10. Plots of observed pseudo-first-order rate constant, k_{obs}, versus $[K_3Fe(CN)_6]$ for the reaction of oxygenated myoglobins with $K_3Fe(CN)_6$ in 100 mM potassium phosphate buffer (pH 7.0) at 25 °C. (A)rMb(**1**), (B)rMb(**2**), and (C)rMb(**3**).

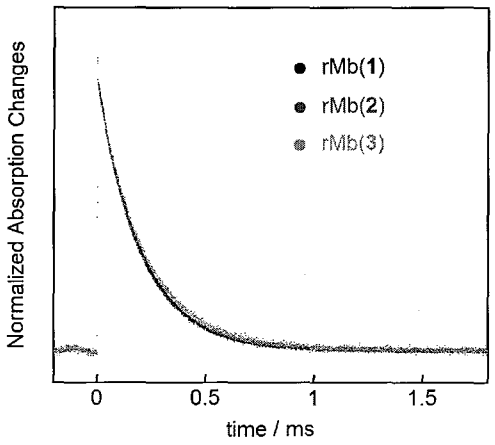

Figure 2-11. Time courses of O_2 association reaction for oxymyoglobins in 100 mM potassium phosphate buffer (pH 7.0) at 25 °C under air. The Soret maxima at 435 nm were monitored.

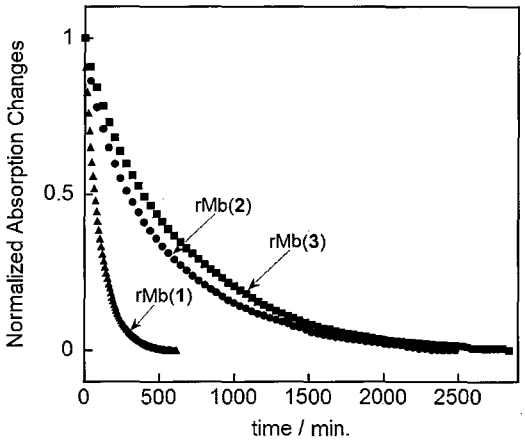

Figure 2-12. Plot of the normalized absorption changes at 580 nm versus time during the stages of autoxidation reaction for oxymyoglobins in 100 mM KPi (pH 7.0) at 37 °C: rMb(**1**) (▲), rMb(**2**) (●), and rMb(**3**) (■).

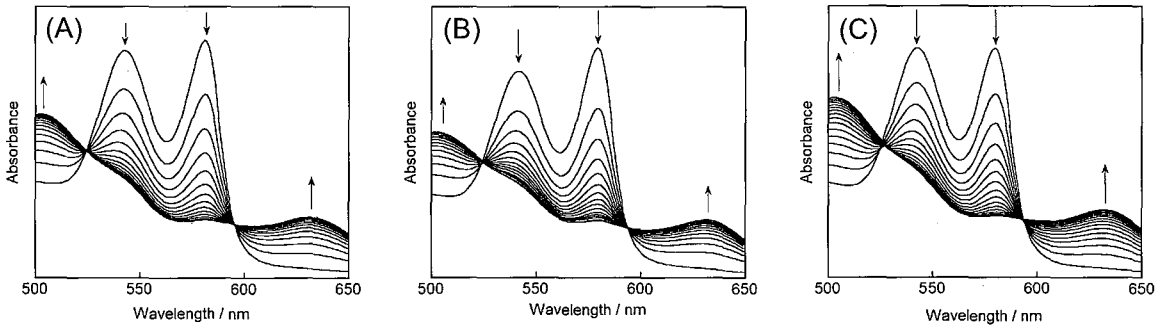

Figure 2-13. Electronic absorption spectral changes during stages of autoxidation reaction for oxymyoglobins in 100 mM potassium phosphate buffer (pH 7.0) at 37 °C. (A) rMb(**1**) every 32 min, (B) rMb(**2**) every 160 min, and (C) rMb(**3**) every 160 min.

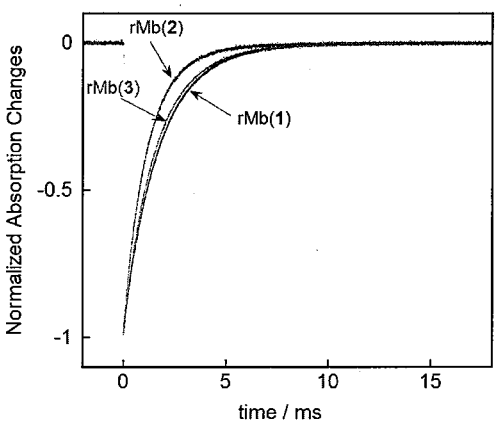

Figure 2-14. Time courses of CO association reaction for CO-myoglobins in 100 mM potassium phosphate buffer (pH 7.0) at 25 °C under CO atmosphre. The Soret maxima at 423 nm were monitored.

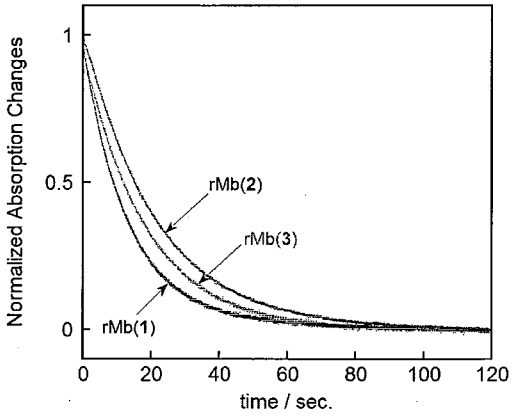

Figure 2-15. Time courses of ligand exchage reaction from CO-Mbs to NO-Mbs in 100 mM potassium phosphate buffer (pH 7.0) at 25 °C. The Soret maxima at 423 nm were monitored.

CO binding structure. To obtain further insight into the CO binding mechanism, the infrared (IR) and RR spectra of CO complexes were recorded [23]. The Fe–C stretching modes for rMb(**2**) and the reference protein rMb(**3**) were exhibited at 511 cm^{-1}, which is 2 cm^{-1} higher than that of rMb(**1**), suggesting that the Fe–C bond for rMb(**1**) is weakened compared to that of the reference protein.

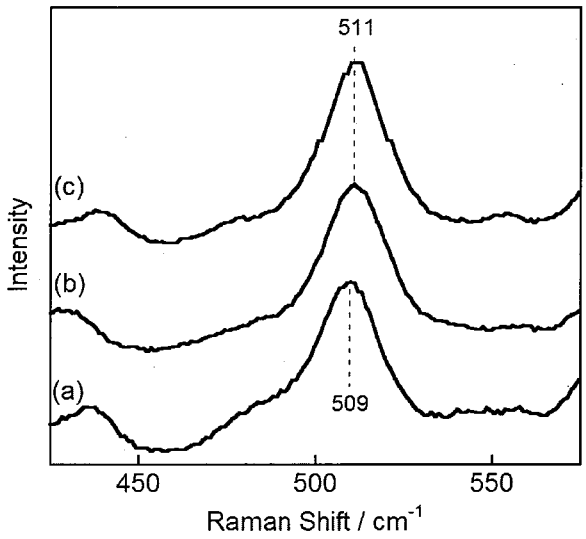

Figure 2-16. Resonance Raman spectra of CO-myoglobins in the 425–575 cm^{-1} region in 100 mM potassium phosphate buffer (pH 7.0) at room temperature: (a) rMb(**1**), (b) rMb(**2**), (c) rMb(**3**). The excitation wavelength was 413.1 nm and a laser power was 10 mW.

The IR spectra in the region of the CO band for the myoglobins are shown in Figure 2-17. It is known that the IR spectrum of the CO-bound native protein exhibits two major peaks at 1945 cm^{-1} (A_1 conformer; 70%) and 1932 cm^{-1} (A_3 conformer; 30%) under physiological conditions, although there are at least four peaks in the region of 1900–2000 cm^{-1} [24, 25]. All proteins, rMb(**1**)–rMb(**3**), exhibit the similar main band (A_1) with the shoulder band (A_3) , while the peak populations for the A_1 and A_3 conformers for CO-rMb(**1**) and CO-rMb(**2**) species are clearly different from those found for the reference protein, CO-rMb(**3**). Table 2-7 demonstrates that the population of the A_3 conformer band in rMb(**1**) is slightly smaller than that of rMb(**3**), whereas the population of the A_3 conformer band in rMb(**2**) is 2-fold larger than that observed for rMb(**3**). These findings suggest that each heme propionate side chain has an influence on the C–O bond strength for CO-myoglobin.

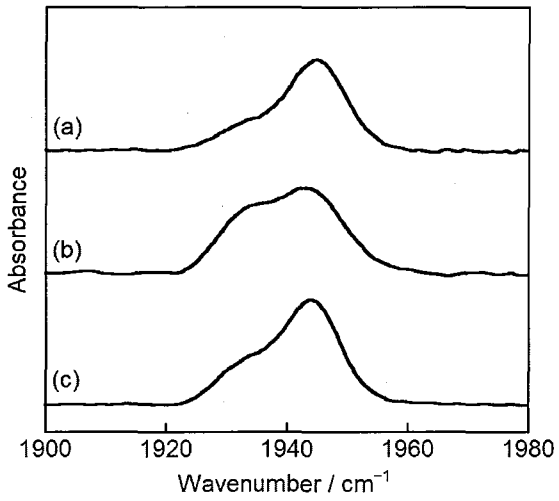

Figure 2-17. IR spectra of CO-bound myoglobins in the 1900–1980 cm^{-1} region in 100 mM potassium phosphate buffer (pH 7.0) at room temperature: (a) rMb(**1**), (b) rMb(**2**), and (c) rMb(**3**).

Table 2-7. IR stretching bands for CO-myoglobins at room temperature and pH 7.0

protein	$A_1(cm^{-1})^a$	$A_3(cm^{-1})^a$
rMb(**1**)	1945(83%)	1934(17%)
rMb(**2**)	1943(57%)	1933(43%)
rMb(**3**)	1944(74%)	1933(26%)

[a] The populations of A_1 and A_3 bands in parentheses. These values were obtained by the deconvolution of each spectrum.

2-4. Discussion

Role of each propionate side chain in myoglobin structure. The distal and proximal sites in the myoglobin have highly conserved hydrogen bonding networks formed by several amino acid residues and two heme propionate side chains. Much work has been done in understanding the structural and functional role of these networks by a variety of myoglobin mutants. In the study presented in chapter 1 of this thesis, it was found that the one-legged hemins **1** and **2** were slightly unstable in the protein matrix under acidic conditions [26]. The dissociation of hemin for rMb(**1**) and rMb(**2**) from the protein matrix occurs at pH 4.3–4.4, which is 0.2 pH unit higher than that observed for the native protein. The small differences in the $pK_{1/2}$ values between the native and reconstituted proteins may be derived from the lack of one propionate side chain. It is well-known that the stabilization of the heme in the protein matrix is mainly due to the Fe–His93 coordination and the hydrophobic contacts between the hemin and apolar amino acid residues, whereas the two heme propionate side chains are not tightly bound to the polar amino acid residues.

The structural data for the mutants with an unnatural residue at position 45 or 92 have been presented for evaluation of the physiological significance of the propionate–protein interaction. For example, the 3D structure of the K45S mutant of the pig myoglobin reveals that the mutation produces a more accessible ligand-binding pocket, whereas the overall structure of the mutant shows only small deviations from that observed for the wild-type protein. The high-resolution X-ray structure of rMb(**1**) demonstrates that the Arg45 residue swings away from the heme pocket to the bulk due to the removal of the 6-propionate side chain–Arg45 interaction. Additionally, the terminal carboxylate group in the Asp60 residue, which tightly interacts with Arg45 in the wild-type myoglobin, is also shifted to the outside because of the lack of a salt bridge with Arg45. Furthermore, the distal hydrogen bonding networks of rMb(**1**) cannot order the waters which have been mediated by the interaction between the CD loop and the heme in the native myoglobin. The finding suggests that a part of the CD loop and E helix regions may partially be loosened by the lack of the 6-propionate side chain with the disruption of the Arg45(CD3)–Asp60(E3) salt bridge.

The X-ray crystallographic analyses of rMb(**1**) and rMb(**2**) at high resolution revealed no remarkable differences in the length of the hydrogen bonds of Ser92–His93 or Leu89–His93 (Table 2-4) which have been proposed to have a role in regulating the coordination geometry of the His93 imidazole. In general, the rotation of the imidazole ring in His93 is sensitive for the ^{1}H NMR spectroscopic measurement of the low-spin ferric state of myoglobin in the presence of KCN (metcyanomyoglobin). La Mar and his coworkers suggested that the heme-5-CH_3 resonance for metcyano-rMb(**2**) clearly shifted upfield at 23.8 ppm, whereas the 5-CH_3 proton signals of metcyano-rMb(**1**) and the corresponding native protein appeared at 26.9 and 26.1 ppm, respectively [27]. Since it is well-known that a clear relationship exists between the angle of the His imidazole ring on the heme plane and the heme methyl chemical shift, it can be proposed that the removal of the 7-propionate side chain induces a slight deviation in the His imidazole ring with a clockwise rotation of ~5−10° on the porphyrin plane [28]. Similar arguments may apply to the S92 mutants such as S92A and S92D [20, 29]. Furthermore, the RR spectra for deoxymyoglobin in the lower-frequency region are indicative of the feature of the Fe–His stretching mode. Friedman, Sligar, and

their coworkers reported that the replacements of Leu89 and Ser92 with Ile and Ala, respectively, shifted the frequency of the ν(Fe–His) mode to a higher value by ~3 cm^{-1} [30]. The 1 cm^{-1} higher wavenumber shift of the corresponding frequency mode by removal of the 7-propionate side chain in rMb(**2**) is similar to those observed with the L89 and S92 mutants. This finding suggests that the 7-propionate side chain also plays an important role in the formation of the hydrogen bonding network to regulate the conformation and coordination property of the histidine imidazole ring.

Role of each propionate side chain in O_2 binding. It is worth noting in the O_2 binding parameters that the dissociation of O_2 for oxy-rMb(**1**) is approximately 3-fold faster than that observed for rMb(**2**) and the reference protein rMb(**3**). This finding supports the fact that the lack of the 6-proiponate side chain remarkably accelerated the dissociation of O_2 from oxy-rMb(**1**). As described above, there is a unique hydrogen bonding network, including the 6-propionate side chain and Arg45 and His64 residues, whereas the 3D structure of met-rMb(**1**) displays the deviation of the Arg45 residue. Thus, the lack of the 6-propionate side chain may have an influence on the conformation of the distal His64 which stabilizes the bound O_2, although a clear difference in the geometry of His64 imidazole rings between rMb(**1**) and the native protein was not seen. Olson and his coworkers reported that the replacement of Arg45 with Ser45 or Gly45 accelerated the O_2 dissociation 2.6- or 2.0-fold, respectively, compared to the native myoglobin [31]. Both results clearly support the fact that the 6-propionate side chain and residue 45 are crucial units for fixing the imidazole ring of His64 in the best position to stabilize the bound O_2.

On the other hand, the O_2 dissociation of oxy-rMb(**2**) is slightly slower than that of rMb(**3**), and consequently, the affinity of rMb(**2**) for O_2 is the highest among three myoglobins. This result could be derived from the increase in the level of π-back-donation from the heme iron to dioxygen due to the increase in the strength of the His93–Fe coordination. The CO dissociation of CO-rMb(**2**) and CO-rMb(**3**) shows a similar behavior, and the stronger Fe–C bond and the weaker CO bond for CO-rMb(**2**) compared to the corresponding bonds of the CO complex of rMb(**3**) support an increase in the level of π-back-donation from the heme iron to the ligand (vide infra).

In addition, the 6-propionate–Arg45 interaction seems to inhibit the unfavorable autoxidation from the oxygenated protein to the inert aquomet species, because the oxidation of oxy-rMb(**1**) is 4.5- and 5.8-fold faster than that for oxy-rMb(**2**) and oxy-rMb(**3**), respectively, as shown in Table 2-5. Although the autoxidation mechanism is generally complicated [32–34], the findings suggest that the 6-propionate side chain clearly contributes to the stabilization of the oxygenated protein species.

The O_2 association rate constants for the reconstituted myoglobins, rMb(**1**) and rMb(**2**), are the same as that observed for rMb(**3**), indicating that the removal of the 6- or 7-propionate side chain has no drastic effect on the O_2 association. It has been reported that the changes in the O_2 association rate constants for the position 45 mutants are relatively small. These results suggest that the "wall" formed by the 6-propionate side chain and Arg45 via hydrogen bonding interaction may play a role in the inhibition of the entry of water molecules but does not act as a kinetic barrier to the entry of O_2 into the heme pocket [35].

Role of each propionate side chain in CO binding. The kinetic parameters of the CO association and dissociation rate constants for rMb(**2**) are slightly different from those observed for rMb(**1**) and the reference protein rMb(**3**). These results indicate that the removal of the 7-propionate side chain enhances the CO affinity by 2-fold due to a small increase in the association rate constant and a small decrease in the dissociation rate constant for rMb(**2**). Although the changes in these parameters are not significant, these results show the same pattern that was observed for the S92A myoglobin mutant, in which the hydrogen bonding network in the proximal site is partially eliminated. It is known that the replacement of Ser92 with a nonpolar residue such as Ala allows flexibility of the proximal histidine, His93, because the S92A mutant lacks the characteristic hydrogen bonding network formed by the 7-propionate side chain and Ser92 and His93 [20, 36]. As a result, the imidazole ring of His93 in the S92A mutant can be rotated clockwise onto the porphyrin plane to reduce the steric hindrance between the pyrrole nitrogens, N2 and N4, and the axial imidazole carbons, Cδ and Cε, and then the affinity of S92A for CO is slightly increased. In the case of the CO binding for rMb(**2**), the enhanced affinity with the fast k_{on} and slow k_{off} in rMb(**2**) may also be derived from the increase in the structural flexibility of the proximal histidine because of the disruption of the characteristic hydrogen bonding network in the absence of the 7-propionate side chain. In addition, the IR spectra of the CO complex for rMb(**2**) reveal that the lack of the 7-propionate side chain increases in the population of the lower-frequency component (A_3 conformer) of the CO stretching modes at 1933 cm^{-1}. It is clearly indicative of the influence on the distal site with the enhanced π-back-donation from Fe to CO in CO-rMb(**2**). This structural evidence supports the fact that the hydrogen bonding interaction between the 7-propionate side chain and Ser92 regulates the conformation of the proximal histidine and the strength of the His93–Fe coordination. On the other hand, the weakness of the population of the A_3 band in CO-rMb(**1**) suggests that the strength of the hydrogen bonding from the His64 NεH group to the bound ligand is reduced in the distal site. In fact, the CO dissociation for CO-rMb(**1**) is slightly faster than that observed for the reference protein, CO-rMb(**3**). This finding also supports the fact that the removal of the 6-propionate side chain destabilizes the bound ligands.

2-5. Summary

In this study, the author has demonstrated that the 6- and 7-propionate side chains work not only as a linker between the prosthetic group and globin but also as a regulator of the myoglobin function. Using the reconstituted myoglobins with two one-legged hemes in which the 6- or 7-propionate side chain was replaced with a methyl group, the roles of each propionate side chain in myoglobin were clarified.

It is found that the lack of the 6-propionate side chain accelerated the O_2 dissociation and the autoxidation from the oxygenated heme. In addition, the crystallographic analysis indicated the deviation of Arg45 and Asp60 residues from the normal positions upon removal of the 6-proponate side chains. These findings support the facts that the 6-propionate side chain contributes to the formation of the stable hydrogen bonding network in the distal site and the increase in the strength of the hydrogen bond from the His64 NεH atom to the heme-bound ligands. On the other hand, the lack of the 7-propionate side chain increases in the π-back-donation from the iron atom to CO, because the spectroscopic data suggest the slight conformational change of the His93 imidazole ring. According to the 3D structure of the native protein, the hydroxyl group of Ser92 seems to be a pivot between the 7-propionate side chain and His93 imidazole. Thus, the 7-proponate side chain contributes to the regulation of the His93 conformatoin via Ser92 with the hydrogen bonding network in the proximal site. Finally, in this study, the author estimated the structure of the deoxy- and oxymyoglobins from the extension of the obtained metmyoglobin structures. To precisely discuss the relationship between the ligand binding and structure of the proteins, further investigations into the structural analysis of the proteins are necessary.

References

1. Phillips, G. N., Jr. (2001) in *Handbook of Metalloproteins* (Messerschmidt, A., Huber, R., Poulos, T., and Wieghardt, K. Eds.) Vol. 1, pp 5–15, John Wiley & Sons, Chichester, U.K.
2. Hargrove, M. S., Barrick, D., and Olson, J. S. (1996) The association rate constant for heme binding to globin is independent of protein structure, *Biochemistry 35*, 11293–11299.
3. Hunter, C. L., Lloyd, E., Eltis, L. D., Rafferty, S. P., Lee, H., Smith, M., and Mauk, A. G. (1997) Role of the heme propionates in the interaction of heme with apomyoglobin and apocytochrome b_5, *Biochemistry 36*, 1010–1017.
4. Hayashi, T. (2005) in *Encyclopedia of Inorganic Chemistry 2* (King, B. R., Eds.) Vol. IV, pp 2167–2180, John Wiley & Sons, Chichester, U.K.
5. Phillips, S. E. V. (1980) Structure and refinement of oxymyoglobin at 1.6 Å resolution, *J. Mol. Biol. 142*, 531–554.
6. Vojtěchovský, J., Chu, K., Berendzen, J., Sweet, R. M., and Schlichting, I. (1999) Crystal structures of myoglobin-ligand complexes at near-atomic resolution, *Biophys. J. 77*, 2153–2174.
7. Smith, K. M., and Craig, G. W. (1983) Porphyrin synthesis through tripyrrins: An alternate approach, *J. Org. Chem 48*, 4302–4306.
8. Otwinowsky, A., and Minor, W. (1997) Processing of X-ray diffraction data collected in oscillation mode, *Methods Enzymol. 276*, 307–326.
9. Brünger, A. T. (1992) Free R value: A novel statistical quantity for assessing the accuracy of crystal structures, *Nature 355*, 472–475.
10. Brünger, A. T., Adams, P. D., Clore, G. M., DeLano, W. L., Gros, P., Grosse-Kunstleve, R. W., Jiang, J. S., Kuszewski, J., Nilges, M., Pannu, N. S., Read, R. J., Rice, L. M., Simonson, T., and Warren, G. L. (1998) Crystallography & NMR system: A new software suite for macromolecular structure determination, *Acta Cryst. D54*, 905–921.
11. Sheldrick, G. M., and Schneider, T. R. (1997) SHELXL: High resolution refinement, *Methods Enzymol. 277*, 319–343.
12. Collaborative Computational Project, Number 4. (1994) The CCP4 Suite: Programs for Protein Crystallography, *Acta Cryst. D50*, 760–763.
13. Yang, F., and Phillips, G. N., Jr. (1996) Crystal structures of CO-, deoxy- and met-myoglobins at various pH values, *J. Mol. Biol. 256*, 762–774.
14. DeLano, W. L. (2002) *The PyMOL Molecular Graphics System*, DeLano Scientific, San Carlos, CA.
15. Kraulis, P. J. (1991) MOLSCRIPT: A program to produce both detailed and schematic plots of protein structures, *J. Appl. Crystallogr. 24*, 946–950.
16. Merritt, E. A., and Bacon, D. J. (1997) Raster3D: Photorealistic molecular graphics, *Methods Enzymol. 277*, 505–524.
17. Lim, A. R., Sishta, B. P., and Mauk, A. G. (2006) Contribution of the heme propionate groups to the electron transfer and electrostatic properties of myoglobin, *J. Inorg. Biochem. 100*, 2017–2023.
18. Kitagawa, T., and Hirota, S. (2002) in *Handbook of vibrational spectroscopy 5* (Chalmers, J. M., and

Griffiths, P. R., Eds.) pp 3426–3446, Johns Willey & Sons, Chichester, U.K.

19. Ray, G. B., Li, X.-Y., Ibers, J. A., Sessler, J. L., and Spiro, T. G. (1994) How far can proteins bend the FeCO unit? Distal polar and steric effects in heme proteins and models, *J. Am. Chem. Soc. 116*, 162–176.
20. Shiro, Y., Iizuka, T., Marubayashi, K., Ogura, T., Kitagawa, T., Balasubramanian, S., Boxer, S. G. (1994) Spectroscopic study of Ser92 mutants of human myoglobin: Hydrogen bonding effect of Ser92 to proximal His93 on structure and property of myoglobin, *Biochemistry 33*, 14986–14992.
21. Luzzati, P. V. (1952) Traitement statistique des erreurs dans la determination des structures cristallines, *Acta Cryst. 5*, 802–810.
22. Brucker, E. A., Olson, J. S., Phillips, G. N., Jr., Dou, Y., and Ikeda-Saito, M. (1996) High resolution crystal structures of the deoxy, oxy, and aquomet forms of cobalt myoglobin, *J. Biol. Chem. 271*, 25419–25422.
23. Kincaid, J. R. (2000) in *The Porphyrin Handbook* (Kadish, K. M., Smith, K., and Guilard, K. S., Eds.) Vol. 7, pp 225–291, Academic Press, San Diego.
24. Shimada, H., and Caughey, W. S. (1982) Dynamic protein structures, *J. Biol. Chem. 257*, 11893–11900.
25. Li, T., Quillin, M. L., Phillips, G. N. Jr., and Olson, J. S. (1994) Structural determinants of the stretching frequency of CO bound to myoglobin, *Biochemistry 33*, 1433–1446.
26. Hayashi, T., Nakagawa, T., Harada, K., Matsuo, T., Hitomi, Y., and Hisaeda, Y. (2004) Chemical properties of sperm whale myoglobins reconstituted with monopropionated hemins, *Chem. Lett. 33*, 1512–1513.
27. La Mar., G. N., Emerson, S. D., Lecomte, J. T. J., Pande, U., Smith, K. M., Craig, G. W., and Kehres, L. A. (1986) Influence of propionate side chains on the equilibrium heme orientation in sperm whale myoglobin. Heme resonance assignments and structure determination by nuclear Overhauser effect measurement, *J. Am. Chem. Soc. 108*, 5568–5573.
28. Yamamoto, Y., Nanai, N., Chujo, R., and Suzuki, T. (1990) Heme methyl hyperfine shift pattern as a probe for determining the orientation of the functionally relevant proximal histidyl imidazole with respect to the heme in hemoproteins, *FEBS Lett. 264*, 113–116.
29. Lloyd, E., Burk, D. L., Ferrer, J. C., Maurus, R., Doran, J., Carey, P. R., Brayer, G. D., and Mauk, A. G. (1996) Electrostatic modification of the active site of myoglobin: Characterization of the proximal Ser92Asp variant, *Biochemistry 35*, 11901–11912.
30. Peterson, E. S., Friedman, J. M., Chien, E. Y. T., and Sligar, S. G. (1998) Functional implications of the proximal hydrogen-bonding network in myoglobin: A resonance Raman and kinetic study of Leu89, Ser92, His97, and F-helix swap mutants, *Biochemistry 37*, 12301–12319.
31. Carver, T. E., Olson, J. S., Smerdon, S. J., Krzywda, S., Wilkinson, A. J., Gibson, Q. H., Blackmore, R. S., Ropp, J. D., and Sligar, S. G. (1991) Contributions of residues 45(CD3) and heme-6-propionate to the bimolecular and geminate recombination reactions of myoglobin, *Biochemistry 30*, 4697–4705.
32. Brantley, R. E., Jr., Smerdon, S. J., Wilkinson, A. J., Singleton, E. W., and Olson, J. S. (1993) The

mechanism of autoxidation of myoglobin, *J. Biol. Chem. 268*, 6995–7010.

33. Gonzalez, G., Gilles-Gonzalez, M. A., Rybak-Akimova, E. V., Buchalova, M., and Busch, D. H. (1998) Mechanisms of autoxidation of the oxygen sensor FixL and *Aplysia* myoglobin implications for oxygen-binding heme proteins, *Biochemistry 37*, 10188–10194.
34. Shikama, K. (1998) The molecular mechanism of autoxidation for myoglobin and hemoglobin: A venerable puzzle, *Chem. Rev. 98*, 1357–1373.
35. Olson, J. S., and Phillips, G. N., Jr. (1996) Kinetic pathways and barriers for ligand binding to myoglobin, *J. Biol. Chem. 271*, 17593–17596.
36. Smerdon, S. J., Krzywda, S., Wilkinson, A. J., Brantley, R. E., Jr., Carver, T. E., Hargrove, M. S., and Olson, J. S. (1993) Serine^{92}(F7) contributes to the control of heme reactivity and stability in myoglobin, *Biochemistry 32*, 5132–5138.

Chapter 3

Evaluation of the Functional Role of the Heme-6-propionate Side Chain in Cytochrome P450cam

3-1. Introduction

The heme *b* (protoheme IX) prosthetic group binds to the protein matrix of hemoproteins via multiple noncovalent interactions to form a holoprotein [1], in which two peripheral heme-propionates have been generally regarded as functioning as anchors for the heme group by forming interactions with the generally polar protein matrix [2]. In the case of cytochrome P450cam (P450cam), the monoxygenase responsible for *d*-camphor hydroxylation, the heme-6-propionate side chain forms hydrogen bonds with Thr101, Gln108, Arg112, and His355 [3] as shown in Figure 3-1. For example, the 6-propionate–Thr101 hydrogen bonding interaction is known to contribute to the thermostability of the protein [4]. The 6-propionate side chain has also been proposed [5] to participate in an electron transfer pathway from reduced putidaredoxin (Pdx) to the heme via Arg112 located at the Pdx binding site [6]. Therefore, to understand the exact role of the 6-propionate side chain in P450cam, the author prepared a novel P450cam reconstituted with a "one-legged heme" **1** where the 6-propionate side chain of the heme is replaced with a methyl group. Here, the author will discuss the structural and functional roles of the 6-propionate side chain by spectroscopic and structural analyses of the reconstituted protein.

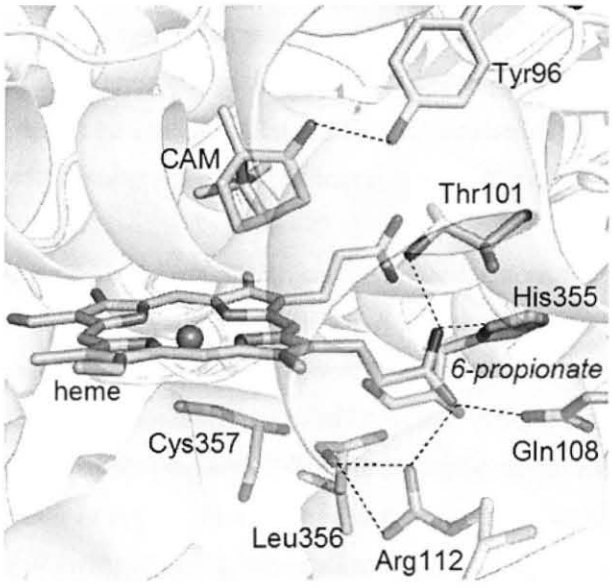

Figure 3-1. Hydrogen bonding network in the active site of camphor-bound wild-type cytochrome P450cam (PDB ID: 1DZ4).

3-2. Experimental Section

3-2-1. Instruments

^{1}H NMR spectra were collected on a Bruker DPX400 (400 MHz) NMR spectrometer. ^{1}H NMR chemical shift values are indicated in ppm relative to the residual solvent resonance. The UV−visible experiments were conducted using a Shimadzu UV-3150 double beam spectrophotometer equipped with a thermostated cell holder having a 0.1 °C deviation. The mass analysis of the proteins was carried out using a TOF mass spectrometer equipped with electrospray ionization on an Applied Biosystems Mariner API-TOF workstation. The equipment for resonance Raman spectroscopy and X-ray crystallographic analysis is described below. Kinetic measurements for the reduction of the proteins were carried out using a stopped-flow system made by Unisoku, Co., Ltd. (Osaka, Japan). The product analysis was performed using a Shimadzu GC-2014 gas chromatograph with a capillary column, DB-1 (J & W Scientific, 30 m × 0.25 mm × 0.25 μm). The pH values were monitored by a HORIBA F-52 pH meter. The reconstitution of P450cam was carried out in an MB120B-G glove box (M.Braun Inertgas-Systeme GmbH, Germany) equipped with an MCPD-3000 Multi Channel Photo Detector and UV/VIS light source (MC-2530) using optical fibers (Otsuka Electronics Co., Ltd, Japan).

3-2-2. Materials

All reagents of the highest guaranteed grade available were obtained from commercial sources and were used as received unless otherwise indicated. Distilled water was demineralized by a Barnstead NANOpure DIamond^{TM} apparatus. The one-legged heme was synthesized by the method described in chapter 1 of this thesis. The proteins were purified by column chromatography through a DE-52 (Whatman), Sephacryl S-200 (Amersham Biosciences), Sephadex G-25 (Amersham Biosciences), and Blue Sepharose 6 Fast Flow (Amersham Biosciences) column.

3-2-3. Methods

Preparations of the wild-type cytochrome P450cam. The wild-type cytochrome P450cam was expressed in *Escherichia coli*, strain JM109, and purified by a previously described procedure with minor modifications [7]. The *E. coli* carrying a gene for the wild-type cytochrome P450cam was grown for 10 hours at 37 °C in 7.5 mL of LB media containing ampicillin (50 μg/mL) with vigorous shaking (200 rpm). The culture was then added to 150 mL of LB media containing ampicillin (50 μg/mL) in 500 mL flask with baffle and was incubated at 37 °C for 13 hours with vigorous shaking (200 rpm). Then, 30 mL of the culture was added to 1.5 L of TB media containing ampicillin (50 μg/mL) and isopropyl-β-D(−)-thiogalactopyranoside (IPTG) (0.24 g/L) in 5 L flask with baffle and was incubated at 37 °C for 10 hours with vigorous shaking (220 rpm). The bacteria were harvested by centrifugation (8800 rpm for 7 min at 4 °C). The total wet weight of bacteria obtained from 6 L of culture media was ca. 90 g

(wet weight). It was stored at −80 °C. The purification of the wild-type P450cam was done at 4 °C unless otherwise indicated. It was lysed by treatments with lysozyme (50 mg of lysozyme per 50 g wet weight of bacteria) (At the same time, RNase A (10 mg/mL × 100 μL) and DNase I (5 U/μL × 160 μL) were added) and with ultrasonication in 40 mM potassium phosphate buffer (pH 7.4) containing 1 mM *d*-camphor (buffer A) (200 mL of buffer per 50 g wet weight of bacteria). The bacterial lysate was loaded on an anion-exchange column DE52 (Whatman, Φ 2.5 cm × 47 cm, v = 230 mL) equilibrated with buffer A, and the column was developed with a linear 0−0.4 M KCl gradient (1.5 L total volume) in the same buffer (flow rate was about 1.5 mL/min.). The eluate containing the cytochrome P450cam was precipitated using ammonium sulfate from 40% (supernatant) to 60% (precipitate), and dialyzed against buffer A. The cytochrome P450cam purified by DE52 anion-exchange column chromatography and ammonium sulfate fractionation was further purified by gel filtration on a Sephacryl S-200 column (Φ 2.6 cm × 60 cm, v = 320 mL, flow rate was about 1.0 mL/min.) equilibrated with 50 mM potassium phosphate buffer (pH 7.4) containing 1 mM *d*-camphor and 50 mM KCl. The fractions containing the cytochrome P450cam with A_{391}/A_{280} ratio of more than 0.8 were collected and concentrated. The enzyme was further purified by an affinity column Blue Sepharose 6FF (Φ 1.5 cm × 34 cm, v = 60 mL) equilibrated with 20 mM potassium phosphate buffer (pH 7.4) containing 0.2 mM *d*-camphor. The column was washed with an column volume of 20 mM potassium phosphate buffer (pH 7.4) containing 0.2 mM *d*-camphor and was developed with a linear 0–0.2 M KCl gradient (500 mL total volume) in the same buffer (flow rate was about 0.7 mL/min.). The fractions containing the cytochrome P450 with A_{391}/A_{280} ratio of more than 1.5 were collected and concentrated. The buffer was exchanged to 50 mM potassium phosphate buffer (pH 7.4) containing 1 mM *d*-camphor and 50 mM KCl, and concentrated into a 1 mM solution. Further, the concentrated sample was frozen with liquid nitrogen and stored at −80 °C. The enzyme samples with an absorption ratio of $A_{391}/A_{280} > 1.5$ were used for the present study. Concentration of the wild-type protein was spectrophotometrically determined using the extinction coefficient of 102 $mM^{-1}cm^{-1}$ at 391 nm [8]. The yield of the wild-type P450cam was 4.5 μmol (200 mg).

Preparations of the wild-type putidaredoxin (Pdx) and putidaredoxin reductase (PdR). Putidaredoxin (Pdx) and putidaredoxin reductase (PdR) were expressed in *E. coli* and purified by the method of Gunsalus and Wagner as previously described [8]. The *E. coli* carrying a gene for the putidaredoxin (Pdx) and putidaredoxin reductase (PdR) was grown for 11 hours at 37 °C in 5 mL of LB media containing ampicillin (50 μg/mL) with vigorous shaking (220 rpm). The culture was then added to 100 mL of LB media containing ampicillin (50 μg/mL) in 500 mL flask with baffle and was incubated at 37 °C for 13 hours with vigorous shaking (220 rpm). Next, 25 mL of the culture was added to 1 L of TB media containing ampicillin (50 μg/mL) in 5 L flask with baffle and was incubated at 37 °C for 8.5 hours with vigorous shaking (220 rpm). The bacteria were harvested by centrifugation (8800 rpm for 7 min at 4 °C). The total wet weight of bacteria obtained from 4 L of culture media was 50 g. It was stored at –80 °C. The purification of the wild-type Pdx and PdR was done at 4 °C unless otherwise indicated. The bacteria were thawed on water bath and lysed by treatments with lysozyme (120 mg of lysozyme per 50 g wet weight of

bacteria) (At the same time, RNase A (10 mg/mL × 50 μL) and DNase I (5 U/μL × 200 μL) were added) and with ultrasonication in 40 mM potassium phosphate buffer (pH 7.4) containing 1 mM *d*-camphor (buffer A) with 10 mM β-mercaptoethanol (250 mL of buffer per 50 g wet weight of bacteria). The bacterial lysate was loaded on an anion-exchange column DE52 (Whatman, Φ 2.5 cm × 41 cm, v = 200 mL) equilibrated with buffer A with 10 mM β-mercaptoethanol, and the column was developed with a linear 0−0.4 M KCl gradient (2.0 L total volume) in the same buffer with 10 mM β-mercaptoethanol (flow rate was about 1.5 mL/min.). The eluate containing the PdR was precipitated using ammonium sulfate (70% saturated), dialyzed against buffer A with 10 mM β-mercaptoethanol. The eluate containing the Pdx was precipitated using ammonium sulfate (85% saturated), dialyzed against buffer A with 10 mM β-mercaptoethanol. The putidaredoxin (Pdx) and the putidaredoxin reductase (PdR) purified by DE52 column and ammonium fractionation were further purified by gel filtration on a Sephacryl S-200 column (Φ 2.6 cm × 60 cm, v = 320 mL, flow rate was about 0.7 mL/min.) equilibrated with 40 mM potassium phosphate buffer (pH 7.4) containing 1 mM *d*-camphor, 50 mM KCl, and 10 mM β-mercaptoethanol, respectively. The fractions containing the Pdx with A_{330}/A_{278} ratio of more than 0.7 and the fractions containing the PdR with A_{273}/A_{455} ratio of less than 7.0 were collected and concentrated, respectively. Further, the concentrated sample was frozen with liquid nitrogen and stored at −80 °C. The purified Pdx and PdR employed in this study had A_{325}/A_{280} and A_{454}/A_{275} ratios greater than 0.70 and 0.14, respectively. Concentrations of the Pdx and PdR were spectrophotometrically determined using the extinction coefficients of 10.4 $mM^{-1}cm^{-1}$ at 455 nm and 10.0 $mM^{-1}cm^{-1}$ at 454 nm, respectively [8]. The yield of Pdx was 9.0 μmol (103 mg) and the yield of PdR was 5.8 μmol (252 mg).

Preparation of apoP450cam. The apoP450cam was prepared by the conventional acid-butanone procedure of Wagner et al. [9]. The pH of the solution of wild-type P450cam (100 μM) dissolved in 0.1 M His-HCl was lowered to 2.5 with cold 0.1 M HCl on ice. To extract heme, an equivolume of 2-butanone was added to the solution. The extraction was repeated three times, and the aqueous apoprotein solution was dialyzed against a 100-fold volume of degassed 0.01% (w/v) $NaHCO_3$ aq. with Ar bubbling at 4 °C for 3 hours. The dialysis was repeated three times (3 hours × 3). Apoprotein was subsequently dialyzed against a 75-fold volume of a degassed solution containing 20% (v/v) glycerol and 0.1 M histidine at pH 8.0 with Ar bubbling at 4 °C for 12 hours.

Protein reconstitution with one-legged heme. ApoP450cam was prepared by the conventional acid-butanone method [9] as described above. The insertion of the one-legged heme into the apoprotein was carried out by Wagner's protocol [9] with some modifications. The 7 mL apoP450cam (105 μM) solution containing 20% (v/v) glycerol and 0.1 M histidine at pH 8.0 was transferred into a glove box (O_2 < 1 ppm). The apoprotein solution was then combined with about 350 μL of aqueous saturated *d*-camphor (8.2 mM) containing 23 mg of dithiothreitol (DTT). The solution was gently stirred for 25 min at room temperature. A 49 μL DMF solution containing a stoichiometric amount of the one-legged heme **1** (15 mM) was dropwise added to the magnetically stirred solution of apoprotein over a period of 10 min. A

UV–vis spectrum of an aliquot of the reaction mixture was monitored in the glove box every 8–10 h and then the reconstitution was completed for 48 h at room temperature.

Purification of reconstituted protein. The purification procedure was done at 4 °C. The reconstituted protein was added into an equivolume of 50 mM KPi (pH 7.4) containing 1 mM *d*-camphor and 250 mM KCl. The solution was concentrated to 0.5 mL using an Amicon Stirred Cell with an Ultrafiltration Disc (YM30) (gas pressure < 0.05 MPa). The free one-legged heme was removed from the concentrated protein solution using a Sephadex G25 column (Φ 1.5 cm × 50 cm, v = 88 mL) equilibrated with 50 mM KPi (pH 7.4) containing 1 mM *d*-camphor and 100 mM KCl (flow rate: ca. 1.0 mL/min.). The protein fractions were collected and purified on a DE52 anion-exchange column (Φ 1.5 cm × 9 cm, v = 16 mL) equilibrated with 50 mM KPi (pH 7.4) containing 1 mM *d*-camphor and 50 mM KCl (flow rate: ca. 0.5 mL/min.). The column was developed with a linear 50–400 mM KCl gradient (100 mL total volume) at a 0.5 mL/min flow rate. Fractions of the main band with an absorption ratio of $A_{418}/A_{280} > 1.0$ for the protein with the one-legged heme were combined, concentrated to a volume of 0.4 mL by the Amicon Stirred Cell containing an Ultrafiltration Disc (YM30) (gas pressure < 0.05 MPa). The sample purified by the DE52 column was loaded onto a Blue Sepharose 6FF column (Φ 1.0 cm × 27 cm, v = 21 mL) equilibrated with 50 mM KPi (pH 7.4) containing 1 mM *d*-camphor and 100 mM KCl (flow rate: ca. 0.4 mL/min.) to remove the inactive P420 species [10]. The fractions of the P450 species were collected and concentrated into a 1 mM solution. Concentration of the ferric camphor-bound reconstituted P450cam with one-legged heme **1** (rP450cam(**1**)) was spectrophotometrically estimated using the extinction coefficient of 102 $mM^{-1}cm^{-1}$ at 391 nm [8]. Concentration of rP450cam(**1**) was also spectrophotometrically estimated from the absorption difference at 446 and 490 nm of the difference spectrum between the CO-bound and ferrous forms, using the extinction coefficient of 93 $mM^{-1}cm^{-1}$ [8, 11].

Characterization of reconstituted P450cam. The protein was first characterized by UV–vis spectroscopy. Since it is well known that the CO-bound P450cam exhibits the characteristic Soret band at 446 nm, the protein sample was reduced by addition of dithionite to yield the CO-bound species under a CO atmosphere. The difference spectrum between the CO-bound and reduced forms of the reconstituted protein showed a λ_{max} at 446 nm, indicating that the thiolate of the Cys357 was ligated to the heme iron of the one-legged heme as seen in the wild-type protein.

The ESI-TOF mass spectrum of the reconstituted protein displayed two peaks at 46547.1 and 47105.7 after deconvolution of the raw data. These numbers are assigned as the apo and reconstituted P450cams (the calculated mass numbers are 46542.89 and 47101.34, respectively).

Reduction of ferric P450cam by reduced Pdx. The reduction of the ferric P450cam was spectrophotometrically monitored after mixing with the reduced Pdx on a stopped-flow apparatus. The 2 μM ferric P450cam solution contains 1 mM *d*-camphor and 100 mM KCl. The reduced Pdx solution

(3–60 μM) was prepared using NADH (360 μM) and a catalytic amount of the PdR (ca. 0.1 μM). Both solutions (50 mM KPi buffer at pH 7.4 in the presence of 1 mM *d*-camphor and 100 mM KCl) contain 60 mM glucose, 0.1 mg/mL glucose oxidase, and 3,000 units/mL catalase to quench the dioxygen in these solutions. The reduction rate of the ferric P450cam by the reduced Pdx was measured by rapid mixing of both solutions under a CO atmosphere at 20 °C, and the rate constant of the reaction was determined by monitoring the formation of the CO-bound P450cam at 446 nm [12].

The reduction of the ferric P450 sample by reduced Pdx can be represented by a two-step model as shown in Scheme 3-1 [12]. In this scheme, $P450cam^{3+}$, $P450cam^{2+}$, $CO\text{-}P450cam^{2+}$, Pdx^{red}, and Pdx^{ox} represent ferric P450cam, ferrous P450cam, CO-bound ferrous P450cam, reduced Pdx and oxidized Pdx, respectively. The previous studies of Peterson and Griffin [13], and Hintz and Peterson [12], which determined the kinetics of carbon monoxide binding to reduced cytochrome, demonstrated that, under the conditions of saturating carbon monoxide used in these studies, the binding of carbon monoxide to reduced cytochrome P450cam is complete within the dead time of the stopped-flow instrument. The ferrous P450cam is immediately trapped as its CO adduct in this experimental condition [12]. Since the conversion from ferrous P450cam–oxidized Pdx ($P450cam^{2+}$–Pdx^{ox}) complex to ferric P450cam–reduced Pdx ($P450cam^{3+}$–Pdx^{red}) complex is completely inhibited due to the strong affinity of CO to the ferrous form, the author can assume $k_{-ET1} = 0$ for eq. 3-1. In this case, the ET reaction follows the Michaelis–Menten type mechanism, and the dissociation constant can be estimated by eq. 3-3 and k_{ET1} can be calculated from the dependence of the formation rate of the CO adduct on the concentration of Pdx. The values of the Michaelis constant (K_{m1}) and the ET rate (k_{ET1}) for the first ET process were estimated by fitting the k_{obs1} values using eq. 3-2 [14].

$$P450_{cam}{}^{3+} + Pdx^{red} \underset{k_{-1}}{\overset{k_1}{\rightleftharpoons}} P450_{cam}{}^{3+}\text{–}Pdx^{red}\ \text{complex} \underset{k_{-ET1}}{\overset{k_{ET1}}{\rightleftharpoons}} P450_{cam}{}^{2+}\text{–}Pdx^{ox}\ \text{complex} \xrightarrow{CO} CO\text{–}P450_{cam}{}^{2+} \qquad (3\text{-}1)$$

$$k_{obs1} = \frac{k_{ET1}[Pdx]}{[Pdx] + K_{m1}} \qquad (3\text{-}2) \qquad\qquad K_{m1} = \frac{k_{-1} + k_{ET1}}{k_1} \qquad (3\text{-}3)$$

NADH oxidation. The NADH oxidation was monitored by the change in the optical absorbance at 340 nm (an extinction coefficent of 6.22 $mM^{-1}cm^{-1}$) for NADH at 20 °C [7]. The reaction condition included the appropriate amount of P450cam (0.042 μM of wild-type P450cam and 0.038 μM of reconstituted P450cam), 100 μM NADH, 14 μM Pdx, 0.12 μM PdR in 50 mM KPi buffer (pH 7.4) (1.5 mL) containing 1 mM *d*-camphor, 100 mM KCl, 600 units/mL catalase and 200 units/mL SOD. The ratio of the rate constants of the NADH oxidation for the wild-type and the reconstituted proteins was independent of the NADH concentration (100–360 μM).

Product analysis. The enzymatic reaction was carried out under the above conditions. Furthermore, 20 μL of 10 mM benzyl alcohol (final concentration is 133 μM) was added to the solution as an internal standard after the reaction. The reaction mixture was extracted with 0.8 mL of CH_2Cl_2, and the organic phase was collected and concentrated to less than 50 μL by a slow N_2 stream. The residue was analyzed by gas chromatography. The temperature was 50 °C initially and was raised to 150 °C at a rate of 5 °C per min, then to 280 °C at a rate of 20 °C per min. Under these conditions, benzyl alcohol elutes in 9.9 min, camphor in 13.4 min, 5-*exo*-hydroxycamphor in 19.5 min.

Resonance Raman spectroscopy excited at 413.1 nm. A 100 μL solution of 40 μM P450cam in 50 mM KPi buffer containing 100 mM KCl and 1 mM *d*-camphor at pH 7.4 was transferred to an airtight spinning cell. The Raman scattering was excited at 413.1 nm (3 mW) by a Kr^+ laser. The data were collected at room temperature. The frequencies of the Raman lines for the ferric P450cams in the high-frequency region were calibrated with toluene and acetone. The frequencies of the Raman lines for the ferric P450cams in the low-frequency region were calibrated with toluene and CH_2Cl_2.

Resonance Raman spectroscopy excited at 363.8 nm. A 50 μL solution of 100 μM P450cam in 50 mM KPi buffer containing 100 mM KCl and 1 mM *d*-camphor at pH 7.4 was transferred to an airtight spinning cell. The Raman scattering was excited at 363.8 nm (6 mW) by an Ar^+ laser. The data were collected at room temperature. The frequencies of the Raman lines for the ferric P450cams were calibrated with indene and CCl_4.

Measurement of resonance Raman spectroscopy of ferrous CO-P450cam excited at 441.6 nm. A 4 μL solution of 1.0 mM ferric P450cam in 50 mM potassium phosphate buffer (pH 7.4) containing 100 mM KCl and 1 mM *d*-camphor was transferred to an air-tight spinning cell. The solution was diluted with 86 μL of 50 mM potassium phosphate buffer (pH 7.4) containing 100 mM KCl and 1 mM *d*-camphor. The CO adduct of the P450cam (ferrous CO-P450cam) was formed through two repeated evacuations of the gas inside the cell followed by the introduction of N_2 and finally the incorporation of $^{12}C^{16}O$ before a small amount (10 mM, 10 μL) of N_2-saturated dithionite solution was added. The Raman scattering was excited at 441.6 nm (3 mW) by a He/Cd laser. The Raman shifts were calibrated with toluene and CCl_4.

Proton nuclear magnetic resonance (^1H NMR) spectroscopy. A buffer dissolving the ferric P450cam was replaced with deuterated 50 mM KPi (pD 7.4) containing 1 mM *d*-camphor and 100 mM KCl by Amicon® Ultra-4 centrifugal filter device (NWCL 30000, 4500 rpm). After replacing buffers, the solution of the ferric P450cam (0.4 mM) in deuterated 50 mM KPi (pD 7.4) containing 1 mM *d*-camphor and 100 mM KCl was placed in a 5 mm tube (SHIGEMI Co. Ltd.). The measurements of ^1H NMR spectrum were carried out at 296 K. The residual water signal was suppressed by using a H_2O presaturation pulse program. The assignments of the characteristic methyl signals were based on the previous papers [15].

Monitoring the conversion from P450 to P420 species. Ferric forms (ca 2 μM) of reconstituted and wild-type P450cams in 50 mM KPi buffer (pH 7.4), containing 1 mM *d*-camphor and 100 mM KCl, were allowed to stand at 25 °C. Their UV–vis spectra were recorded repetitively over the course of one day. At each 1–3 hours, an aliquot was taken and its difference spectrum between CO- and reduced forms was recorded. The decay of the intensity at 391 nm from the *d*-camphor-bound high-spin state was found to correspond to the conversion from P450 to P420 species. The P420 species was inactive to *d*-camphor hydroxylation in a reconstituted system comprised of Pdx, PdR and NADH.

Crystallization of the reconstituted and the wild-type proteins. Crystals of the reconstituted P450cam and wild-type P450cam were grown using the sitting-drop vapor diffusion method. Crystallization was carried out on a VDX Plate™ with Micro-Bridges® (HAMPTON RESEARCH Corporation). A 700 μL aliquot of the buffer solution (50 mM Tris-HCl at pH 7.4 containing 250 mM KCl, 10 mM dithioerythritol (DTE) and 1 mM *d*-camphor) with 14% (w/v) PEG8000 (ICN Biomedicals, Inc.) for the reconstituted protein was poured into the reservoir of the VDX Plate™. For the wild-type protein crystallization, 14% (w/v) PEG4000 (Fluka) instead of PEG8000 was used. Next, the protein dissolved in the 6 μL of the same buffer solution with 14% (w/v) PEG8000 for the reconstituted protein or 14% (w/v) PEG4000 for the wild-type protein was poured into the well of the Micro-Bridges®, respectively. The plate was sealed with an acrylic tape and then placed at −5 °C for 2 days.

Data collection and structure refinement. The crystals in a cryoprotectant solution (15% hexylene glycol for the reconstituted protein and 20% hexylene glycol for the wild-type protein) were flash-frozen in liquid nitrogen. The X-ray diffraction data were collected at BL44XU in SPring-8, Hyogo, Japan. The data were indexed, integrated, scaled and merged using the program HKL2000 [16]. The data collection and refinement statistics are shown in Tables 3-1 and 3-2. The initial phases of the reconstituted and the wild-type proteins were obtained by the molecular replacement method of MOLREP [17] in the CCP4 program suite [18] using the wild-type camphor-bound P450cam as a search model [3(a)]. The 5% randomly selected reflections were selected as test reflections for use in the free R cross-validation method throughout the refinement [19]. The model was manipulated using the program COOT [20], and refined with the program REFMAC5 [21] in the CCP4 program suite [18]. The figures were created with Pymol [22]. The atomic coordinates and structure factors have been deposited in the Protein Data Bank (entries 2ZAW and 2ZAX for the reconstituted ferric camphor-bound P450cam with one-legged heme **1** and the wild-type ferric camphor-bound P450cam, respectively).

Table 3-1. X-ray data collection and refinement statistics of the ferric rP450cam(**1**) (2ZAW)

Data Collection	
X-ray source	SPring-8 BL44XU
detector	MAC Science DIP-6040 (Imaging Plate)
wavelength (Å)	0.7
resolution (Å)	45.04–1.55 (1.59–1.55)
space group	$P4_32_12$
unit cell parameters (Å)	$a = 63.675$, $b = 63.675$, $c = 250.272$
number of observations	553416 (N.A.)
number of unique reflections	75813 (4929)
completeness (%)	99.8 (100.0)
$I/\sigma(I)$	9.1 (5.9)
redundancy	7.3 (7.4)
Refinement	
resolution (Å)	45.02–1.55
total reflections	75743
number of non-H atoms	
protein	3208
water	804
other	52
R_{cryst} (%)	15.9
R_{free} (%)	18.2
r.m.s.d from target	
bond lengths (Å)	0.010
angle distances (Å)	1.501
mean isotropic equivalent B-factor (Å^2)	
all protein atoms	16.41
main-chain atoms	11.45
side-chain atoms	13.27
water molecules	34.43
protoheme	8.19
potassium ion	8.91
camphor	6.06
chloride ion	12.57

Table 3-2. X-ray data collection and refinement statistics of the wild-type ferric P450cam (2ZAX)

Data Collection	
X-ray source	SPring-8 BL44XU
detector	MAC Science DIP-6040 (Imaging Plate)
wavelength (Å)	0.7
resolution (Å)	31.77–1.60 (1.66–1.60)
space group	$P4_32_12$
unit cell parameters (Å)	$a = 63.522$, $b = 63.522$, $c = 249.670$
number of observations	486112 (N.A.)
number of unique reflections	65093 (6730)
completeness (%)	99.5 (100.0)
$I/\sigma(I)$	8.7 (5.6)
redundancy	7.1 (7.1)
Refinement	
resolution (Å)	31.77–1.60
total reflections	65093
number of non-H atoms	
protein	3208
water	562
other	63
R_{cryst} (%)	16.5
R_{free} (%)	18.3
r.m.s.d from target	
bond lengths (Å)	0.011
angle distances (Å)	1.502
mean isotropic equivalent B-factor (Å^2)	
all protein atoms	16.77
main-chain atoms	13.87
side-chain atoms	15.63
water molecules	30.08
protoheme	10.60
potassium ion	10.65
camphor	6.12

3-3. Results

Preparation and characterization of reconstituted cytochrome P450cam with 6-methyl-6-depropionated heme. Insertion of the one-legged heme **1** into apoP450cam was carried out according to the method of Wagner et al. [9] with minor modifications. Conventionally, in the reconstitution, non-native hemes were dissolved in 0.1 or 0.01 M KOH and added to the apoprotein solution [9, 23–26]. However, the one-legged heme **1** was not sufficiently dissolved in 0.1 or 0.01 M KOH. Therefore, the stoichiometric amount of one-legged heme **1** was dissolved in *N*, *N*-dimethylformamide (DMF) [27] and added to the apoprotein solution in the presence of 20 mM dithiothreitol (DTT) and 0.4 mM *d*-camphor in a glove box (< 1 ppm O_2). After 8 h of the addition of one-legged heme solution, the P420 species were favored over the P450 species. But 22 h of the addition of one-legged heme solution, the P450 species were favored over the P420 species (Figure 3-3). As time goes by, population of P450 species hyperbolic increased and reached to equilibrium after 36–48 h (Figure 3-4). At equilibrium, 30% of apoprotein converted to P450 species, 20% of apoprotein converted to P420 species, and 50% of apoprotein remained to be not reconstituted. The ratio of added heme to apoprotein over 1.0 resulted in over 20% conversion to P420 species and in decrease of the yield of P450 species at equilibrium. Therefore, the ideal ratio of added heme to apoprotein was 1:1 in the case of monodepropionated-heme reconstitution. The excess hemes were removed by passage through G25 gel filtration column. Furthermore, the apoprotein not reconstituted was removed by passage through DE52 anion-exchange column. Finally, to remove inactive P420 species, reconstituted sample was passed through a Blue Sepharose 6 Fast Flow column [10].

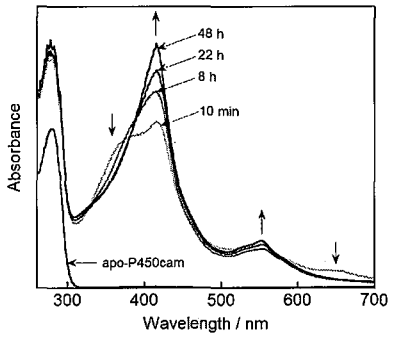

Figure 3-2. UV–vis spectral changes at various time during the reconstitution reaction in 0.1 M His buffer (pH 8.0) containing 20% glycerol (v/v), 0.4 mM *d*-camphor, and 20 mM DTT at room temperature in a glove box (O_2 < 1 ppm).

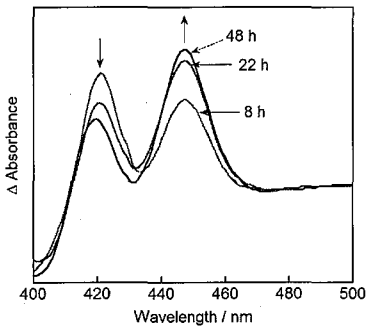

Figure 3-3. Difference spectral changes between CO- and reduced- forms of $P450_{cam}$ at various time during the reconstitution reaction in 0.1 M His buffer (pH 8.0) containing 20% glycerol (v/v), 0.4 mM *d*-camphor, and 20 mM DTT at room temperature in a glove box (O_2 < 1 ppm).

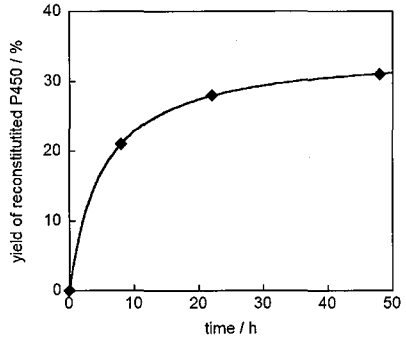

Figure 3-4. Plot of the yield of reconstituted $P450_{cam}$ versus time during the stages of reconstitution reaction in 0.1 M His buffer (pH 8.0) containing 20% glycerol (v/v), 0.4 mM *d*-camphor, and 20 mM DTT at room temperature in a glove box (O_2 < 1 ppm).

The ESI-TOF mass spectrum of the purified reconstituted protein displayed two peaks at 46547.1 and 47105.7 after deconvolution of the raw data (Figure 3-5). These numbers are assigned as the apo and reconstituted P450cams (the calculated mass numbers are 46542.89 and 47101.34, respectively).

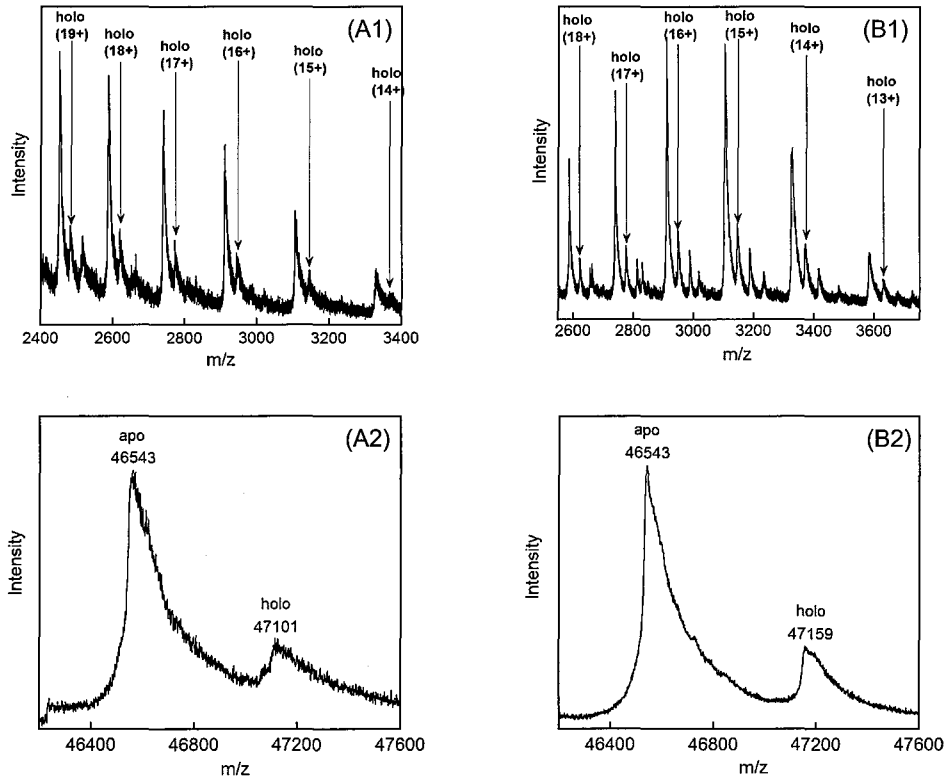

Figure 3-5. ESI-TOF mass spectra of $P450_{cam}$s in 5.7 mM ammonium acetate buffer containing 27% CH_3CN, 0.2% formic acid, 10% methanol. (A1) $rP450_{cam}$(**1**), (B1) wild-type $P450_{cam}$, deconvoluted mass spectra of $P450_{cam}$s (A2) $rP450_{cam}$(**1**), (B2) wild-type $P450_{cam}$. Experimental conditions: spray tip potential 4500 V, nozzle potential 200 V, nozzle temperature 140 °C, detector voltage 2350 V, sample infusion rate 5 μL/min.

Figure 3-6 shows absorption spectra of ferric enzyme in the presence of 1 mM *d*-camphor and 100 mM KCl at 20 °C. The spectra of $rP450_{cam}$(**1**) was almost indistinguishable from that of wild-type enzyme. The UV–vis spectrum of the purified reconstituted ferric protein has a Soret band wavelength at 391 nm characteristic of the high-spin state in the presence of 1 mM *d*-camphor with 100 mM KCl [28]. The difference spectrum between CO-bound and reduced forms of the reconstituted P450cam indicates a Soret λ_{max} at 446 nm, indicating that the thiolate of Cys357 is ligated to the heme iron of the one-legged heme as seen in the wild-type protein (Figure 3-6 (D)). The ferrous P450cams were obtained by dithionite reduction in a glove box. The CO forms were prepared by flushing the ferric forms with pure CO gas before a small amount of dithionite was added. The oxygenated enzymes (oxy-P450cams) were prepared by mixing the solution of ferrous enzymes with an equal volume of O_2 saturated buffer at 4 °C. These spectra are comparable with the analogous spectra of the camphor-bound wild-type protein (Figure 3-6). This suggests that removal of the 6-propionate side chain does not have a serious influence on the electronic and structural properties of the heme. The absorption maxima for the various species of the P450cams are summarized in Table 3-3.

Table 3-3. Absorption maxima for $P450_{cam}$s

protein	λ_{max} (nm)			
	ferric-$P450_{cam}$	ferrous-$P450_{cam}$	oxy-$P450_{cam}$[c]	CO-$P450_{cam}$
$rP450_{cam}$(**1**) (+cam)[a]	391, 512, 646	410, 547	421, 557	446, 550
wt-$P450_{cam}$ (+cam)[a]	391, 512, 646	409, 545	420, 555	446, 550
wt-$P450_{cam}$ (−cam)[b]	417, 535, 569	408, 540[d]		447, 550[d]

[a] pH 7.4 (50 mM potassium phosphate buffer containing 100 mM KCl and 1 mM *d*-camphor) and 20 °C.
[b] pH 7.4 (20 mM potassium phosphate buffer containing 100 mM KCl) and 20 °C. [c] at 4 °C.
[d] pH 7.0 (50 mM potassium phosphate buffer) and 25 °C from ref. [8].

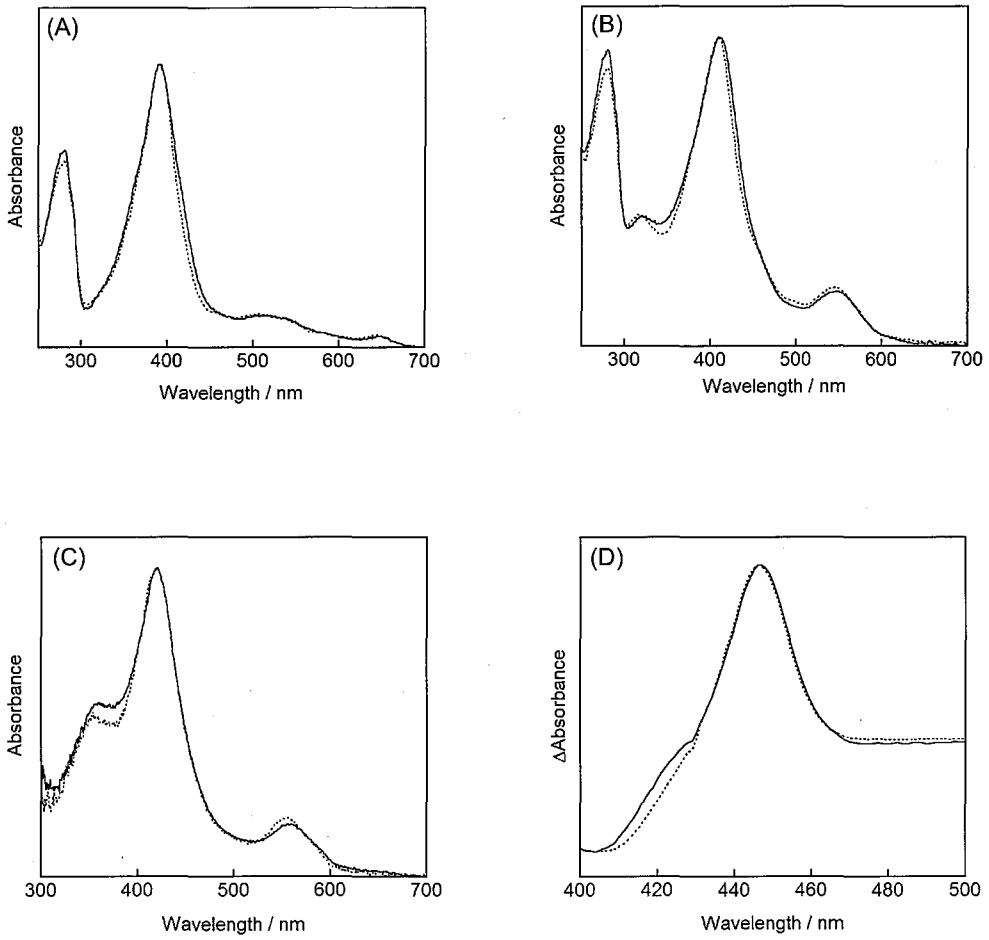

Figure 3-6. Absorption spectra of $rP450_{cam}$(**1**) (solid line) and wild-type $P450_{cam}$ (dotted line) in 50 mM KPi (pH 7.4) containing 100 mM KCl and 1 mM *d*-camphor at 20 °C. (A) ferric-$P450_{cam}$s, (B) ferrous-$P450_{cam}$s, (C) oxy-$P450_{cam}$s (at 4 °C), (D) difference spectra between CO- and ferrous-$P450_{cam}$s.

High-frequency resonance Raman spectra of ferric P450cams excited at 413.1 nm. In the high-frequency range, the spectra are dominated by the stretching porphyrin modes that are sensitive to spin state and coordination state of the iron [29]. The visRR spectra in the high-frequency region, where skeletal stretching vibrations of prophyrin macrocycle appear, reflect the oxidation state, coordination number, and spin state of the heme iron. The ν_4 band at 1370–1375 cm^{-1} is an oxidation state marker. The ν_3 band at 1480–1510 cm^{-1} is an oxidation state, coordination number and spin state marker. The ν_2 band at 1565–1585 cm^{-1} is a spin state marker. In the all samples, the oxidation marker band ν_4 appeared in the 1371–1373 cm^{-1} regions, which indicates the ferric state. The ν_3 band for ferric camphor-free wild-type P450cam appeared at 1502 cm^{-1}, which corresponded to the six-coordinate ferric low-spin species. The ν_3 band for ferric camphor-bound wild-type P450cam appeared at 1487 cm^{-1}, which corresponded to the five-coordinate ferric high-spin species. Also, the ν_3 band for ferric camphor-bound rP450cam(**1**) appeared at 1488 cm^{-1}, which corresponded to the five-coordinate ferric high-spin species. This suggests that removal of the 6-propionate side chain does not have a serious influence on the electronic and structural properties of the heme.

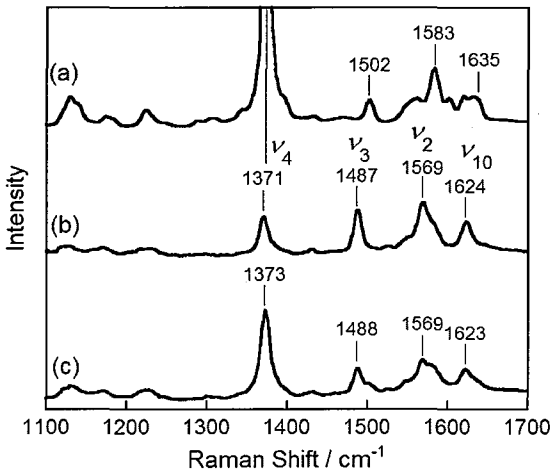

Figure 3-7. Resonance Raman spectra of ferric P450cams in 1100–1700 cm^{-1} region in 50 mM potassium phosphate buffer (pH 7.4) containing 1 mM *d*-camphor (except (a)) and 100 mM KCl at room temperature; (a) camphor-free wild-type P450cam spectrum, (b) camphor-bound wild-type P450cam spectrum and (c) camphor-bound rP450cam(**1**) spectrum. The excitation wavelength was 413.1 nm and the laser power was 3 mW.

Table 3-4. Frequencies of resonance Raman lines (cm^{-1}) in the high-frequency region of the ferric form

protein	ν_4	ν_3	ν_2	ν_{10}
$rP450_{cam}$(**1**) (+cam)[a]	1373	1488	1569	1623
wt-$P450_{cam}$ (+cam)[a]	1371	1487	1569	1624
wt-$P450_{cam}$ (−cam)[b]	1373	1502	1583	1635

[a] pH 7.4 (50 mM KPi buffer containing 100 mM KCl and 1 mM *d*-camphor) at room temperature.
[b] pH 7.4 (50 mM KPi buffer containing 100 mM KCl) at room temperature.

Low-frequency resonance Raman spectra of ferric P450cams excited at 413.1 nm. The low-frequency region is sensitive to ruffling and other distortion in the porphyrin macrocycle. It is also sensitive to the conformational changes of the substituents [29]. The band located at 343 cm^{-1} for rP450cam(**1**) and 345 cm^{-1} for wt-P450cam is assigned to the ν_8(Fe–N) in-plane skeletal mode. The band located at 365 cm^{-1} is assigned to the $\gamma_6(A_{2u})$ out-of-plane mode associated with the pyrrole tilting vibration. The band at 314 cm^{-1} is assigned to the $\gamma_7(A_{2u})$ out-of-plane mode from methine wagging motion [29]. The band of the vinyl bending mode located at 426 cm^{-1} in the camphor-free wild-type P450cam was shifted to 422 cm^{-1} in the camphor-bound wild-type P450cam and rP450cam(**1**), respectively. The band assigned to the porphyrin-propionate bending mode appeared at 380 cm^{-1} in the camphor-free and camphor-bound wild-type P450cam. However, the corresponding band was not observed in the camphor-bound rP450cam(**1**) reconstituted with the monodepropionated heme **1**.

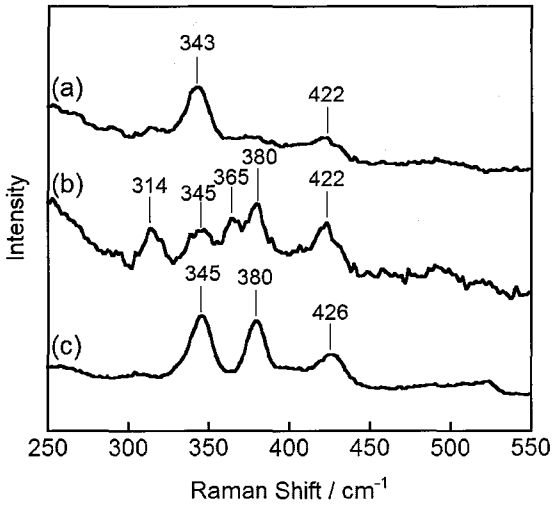

Figure 3-8. Resonance Raman spectra of ferric P450cams in 250–550 cm^{-1} region in 50 mM potassium phosphate buffer (pH 7.4) containing 1 mM *d*-camphor (except (c)) and 100 mM KCl at room temperature; (a) camphor-bound rP450cam(**1**) spectrum, (b) camphor-bound wild-type P450cam spectrum and (c) camphor-free wild-type P450cam spectrum. The excitation wavelength was 413.1 nm and the laser power was 3 mW.

Table 3-5. Frequencies of resonance Raman lines (cm^{-1}) in the low-frequency region of the ferric form

protein	$\gamma_7(A_{2u})$	ν_8(Fe–N) A_{1g}	$\gamma_6(A_{2u})$	$\delta(C_\beta C_c C_d)$propionate	$\delta(C_\beta C_a C_b)$vinyl + $\delta(C_\beta CH_3)$ in-plane
$rP450_{cam}$(**1**) (+cam)[a]	—	343	—	—	422
wt-$P450_{cam}$ (+cam)[a]	314	345	365	380	422
wt-$P450_{cam}$ (–cam)[b]	—	345	—	380	426

[a] pH 7.4 (50 mM KPi buffer containing 100 mM KCl and 1 mM *d*-camphor) at room temperature.
[b] pH 7.4 (50 mM KPi buffer containing 100 mM KCl) at room temperature.

Low-frequency resonance Raman spectra of ferrous CO complex of P450cams excited at 441.6 nm. The Fe–CO stretching (ν_1) mode appeared at 465 cm^{-1} for ferrous CO complex of camphor-free wild-type P450cam [30]. Furthermore, the Fe–CO stretching (ν_1) mode appeared at 485 cm^{-1} for ferrous CO complex of camphor-bound wild-type P450cam [30]. Therefore, camphor binding to ferrous CO complex of camphor-free wild-type P450cam shifted Fe–CO stretching mode ($\Delta\nu$ = 20 cm^{-1}). The Fe–CO stretching (ν_1) mode appeared at 483 cm^{-1} for ferrous CO complex of camphor-bound rP450cam(**1**). It is very similar to that of ferrous CO complex of camphor-bound wild-type P450cam (Figure 3-9).

Resonance Raman spectra of ferric P450cams excited at 363.8 nm. The resonance Raman spectra of the rP450cam(**1**) in the low-frequency region excited at 363.8 nm (Figure 3-10 and 3-11) showed the Fe–S stretching mode at 348 cm^{-1}, which is shifted 3 cm^{-1} lower relative to the corresponding band of the wild-type protein [31] (Figure 3-10). Thus, the lower frequency data provide evidence that the lack of the 6-propionate side chain induces weakening of the Fe–Cys357 ligation.

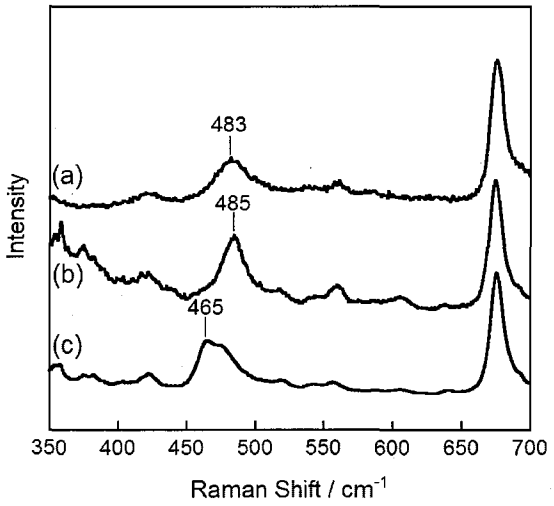

Figure 3-9. Resonance Raman spectra of CO-P450cams in 350–700 cm^{-1} region in 50 mM potassium phosphate buffer (pH 7.4) containing 1 mM *d*-camphor (except (c)) and 100 mM KCl at room temperature; (a) camphor-bound rP450cam(**1**) spectrum, (b) camphor-bound wild-type P450cam spectrum, and (c) camphor-free wild-type P450cam spectrum. The excitation wavelength was 441.6 nm and the laser power was 3 mW.

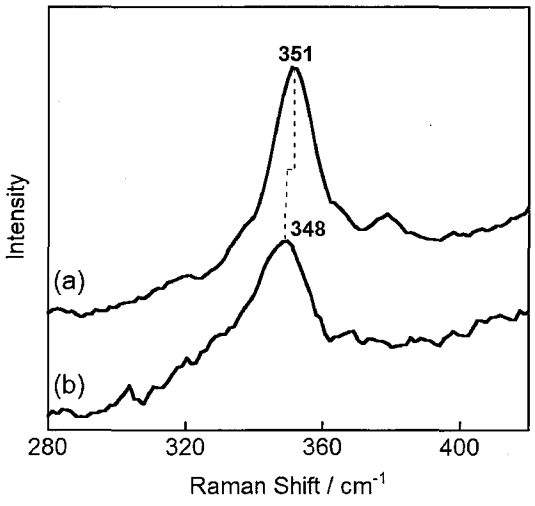

Figure 3-10. Resonance Raman spectra of ferric P450cams in 280–420 cm^{-1} region in 50 mM potassium phosphate buffer (pH 7.4) containing 1 mM *d*-camphor and 100 mM KCl at room temperature; (a) camphor-bound wild-type P450cam spectrum and (b) camphor-bound rP450cam(**1**) spectrum. The excitation wavelength was 363.8 nm and the laser power was 6 mW.

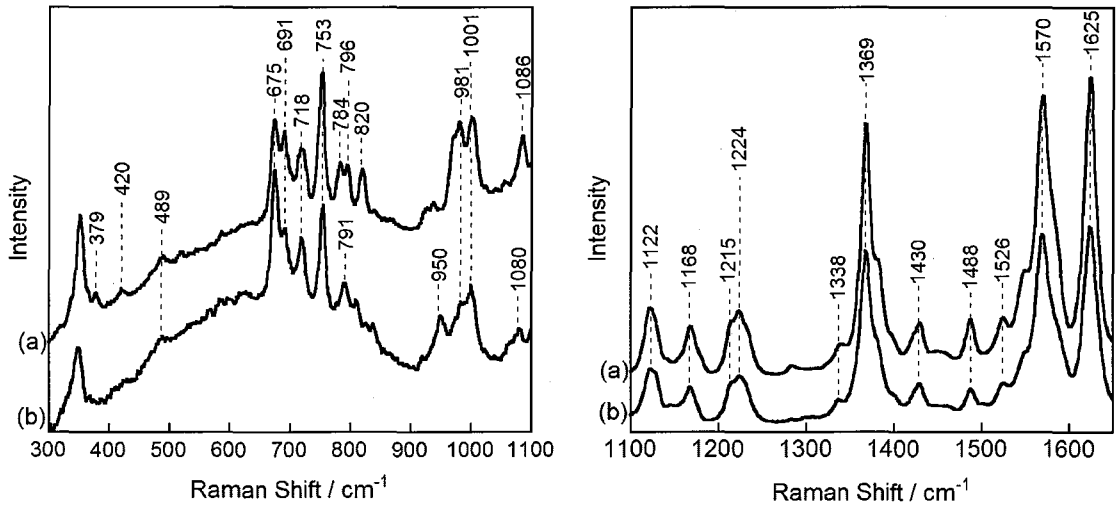

Figure 3-11. Resonance Raman spectra of ferric P450cams excited at 363.8 nm in 300–1100 cm^{-1} and 1100–1650 cm^{-1} regions in 50 mM potassium phosphate buffer (pH 7.4) containing 1 mM *d*-camphor and 100 mM KCl at room temperature; (a) camphor-bound wild-type P450cam and (b) camphor-bound rP450cam(**1**) spectrum. The excitation wavelength was 363.8 nm and the laser power was 6 mW.

Table 3-6. Frequencies of resonance Raman lines (cm^{-1}) for the Fe–CO stretching mode in the ferrous state and for the Fe–S stretching frequencies in the ferric state [a]

protein	ν_{Fe-CO}	ν_{Fe-S}
$rP450_{cam}$(**1**)	483	348
wt-$P450_{cam}$	485	351

[a] pH 7.4 (50 mM KPi buffer containing 100 mM KCl and 1 mM *d*-camphor) at room temperature.

Proton nuclear magnetic resonance (^1H NMR) spectroscopy. Figure 3-12 shows paramagnetic shifts of the heme substituents for the ferric forms of wild-type P450cam and rP450cam(**1**) in 50 mM KPi (pD 7.4) containing 100 mM KCl and 1 mM *d*-camphor at 296 K. Camphor-bound ferric wt-P450cam is in the high-spin state and shows the hyperfine shifted NMR peaks at 62.3, 57.6, 40.4, and 35.6 ppm, which could be assigned to 8-, 3-, 5-, and 1-methyl groups of the heme, respectively [15] at 296 K. Camphor-bound ferric $rP450_{cam}$(**1**) is in the high-spin state and shows the hyperfine shifted NMR peaks at 61.8, 56.4, 41.8, and 35.3 ppm, which could be assigned to 8-, 3-, 5-, and 1-methyl groups of the heme, respectively, in the analogy of camphor-bound ferric wild-type P450cam. In addition, the signal of 6-methyl group appeared at 43.9 ppm.

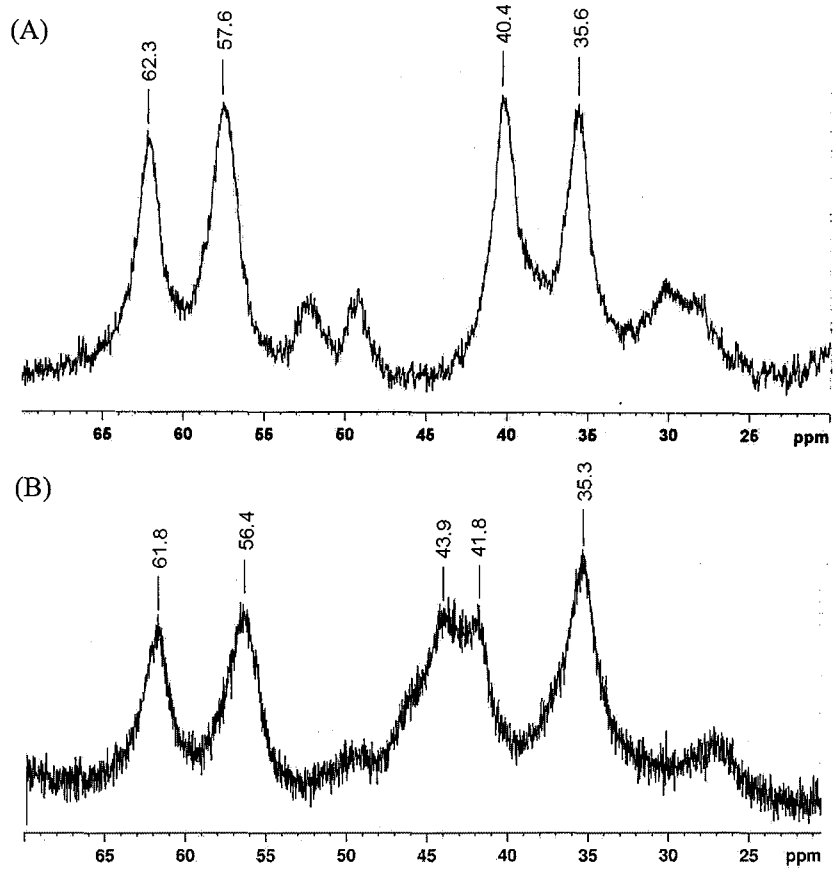

Figure 3-12. ^1H NMR spectra of the ferric high-spin form for (A) wild-type P450cam and (B) rP450cam(**1**) in 50 mM KPi (pD 7.4) containing 100 mM KCl and 1 mM *d*-camphor at 296 K.

Table 3-7. Heme methyl assignment (ppm) for ferric P450cams[a]

	assignment (ppm)[b]				
protein	8-CH_3	3-CH_3	6-CH_3	5-CH_3	1-CH_3
wt-P450cam	62.3	57.6	-----	40.4	35.6
rP450cam(**1**)	61.8	56.4	43.9	41.8	35.3

[a] in deuterated 50 mM KPi (pD 7.4) containing 100 mM KCl and 1 mM *d*-camphor at 296 K.
[b] The assignment of proton signals for wild-type P450cam was based on the literature in ref. [15]. The assignment for the reconstituted P450cam was tentatively performed by the analogy of wild-type protein.

Crystal structure of the reconstituted P450cam with one-legged heme. The X-ray structure of a tetragonal crystal of the ferric rP450cam(**1**) has been determined at a resolution of 1.55 Å at 100 K (Figure 3-13). Wild-type and reconstituted proteins are superimposable with a root-mean-square deviation (all Cα atoms) of 0.126 Å (Table 3-8) [32]. The one-legged heme is located in the same plane in the normal position of the heme pocket. The conformations of amino acid residues surrounding the heme pocket are generally similar to those of the wild-type protein, with the notable exception of the conformation of Thr101 (Figure 3-14) [3(b), 32]. The hydroxyl group of Thr101, which interacts with the 6-propionate side chain in the wild-type protein, is found to form a hydrogen bond with Tyr96 with an intervening distance of 2.69 Å. Notably, a chloride anion occupies the position of the 6-propionate carboxylate as a counteranion. This chloride ion interacts with Gln108, Arg112, and His355 with intervening distances of 3.28, 3.27, and 2.95 Å, respectively.

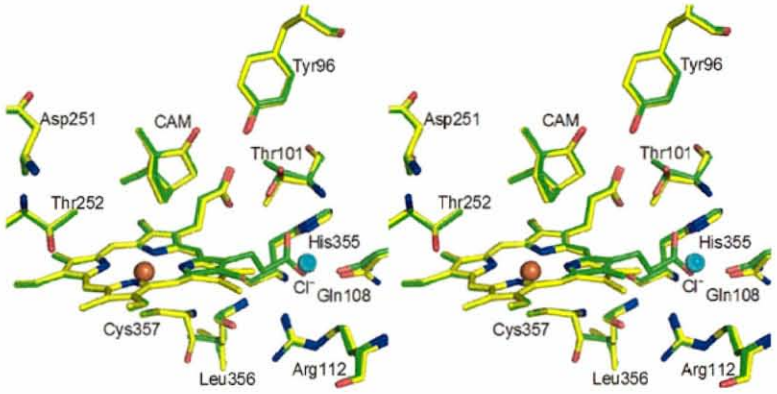

Figure 3-13. Superimposed structures (stereo image) of reconstituted (PDB ID: 2ZAW) and wild-type (PDB ID: 2ZAX) ferric P450cams. The carbon atoms of the reconstituted and the wild-type structures are shown as yellow and green sticks, respectively.

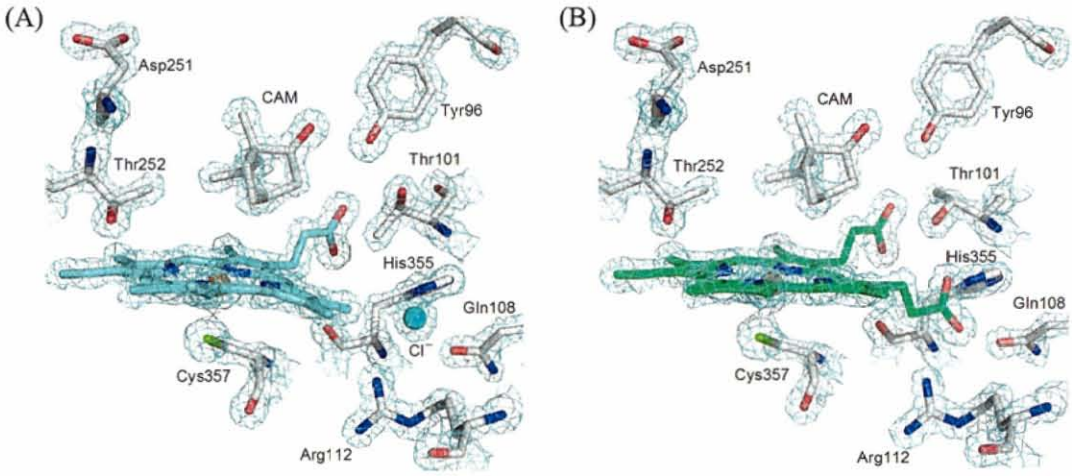

Figure 3-14. Active site structures of (A) reconstituted (2ZAW) and (B) wild-type (2ZAX) P450cams. The $2F_o-F_c$ electron density (2.0σ contours) around the heme and amino acid residues is also shown.

Table 3-8. Geometry of the reconstituted and wild-type *d*-camphor-bound P450cams

	rP450cam(**1**) (2ZAW)	wild-type (2ZAX)
Sample	ferric camphor-bound	ferric camphor-bound
Space group	$P4_32_12$	$P4_32_12$
Resolution (Å)	1.55	1.60
Program	REFMAC 5	REFMAC 5
pH of crystal	7.4	7.4
r.m.s.d. of Cα (Å)	0.126 (2ZAX)	------
Distances (Å)		
Cys 357 S – Fe	2.38	2.38
Camphor C5 – Fe	3.90	4.05
Tyr96 O – camphor O	2.66	2.68
Thr101 O – Tyr96 O	2.69	3.68
Thr101 O – 6-propionate O	-----	2.83
Arg112 NH1– Leu356 CO	2.92	2.83
Arg112 NH2– Leu356 CO	2.92	3.01
Cys 357 S – Leu358 N	3.46	3.46
Cys 357 S – Gly359 N	3.16	3.15
Cys 357 S – Gln360 N	3.29	3.28

The first electron transfer from reduced Pdx to ferric P450cam. To investigate the influence of the lack of heme-6-propionate side chain on electron transfer reaction, the author measured the first electron transfer rate from reduced Pdx to ferric P450cam in the single turnover reaction. The first electron transfer rate can be evaluated by monitoring the formation rate of ferrous CO complex of P450cam after the rapid mixing of ferric P450cam and reduced Pdx under CO atmosphere [12]. The apparent rate constants (k_{obs1}) at the various concentrations of Pdx was estimated from the time course of absorbance change at 446 nm, which is the Soret maximum of ferrous CO ligated P450cam, fitted to a single exponential curve. Next, apparent first-order rate constants were plotted as a function of reduced Pdx concentration (Figure 3-15). The values of the Michaelis constant (K_{m1}) and the first electron transfer rate (k_{ET1}) were estimated by fitting the k_{obs1} values using eq. 3-3. The values obtained in the first electron transfer reaction are summarized in Table 3-9.

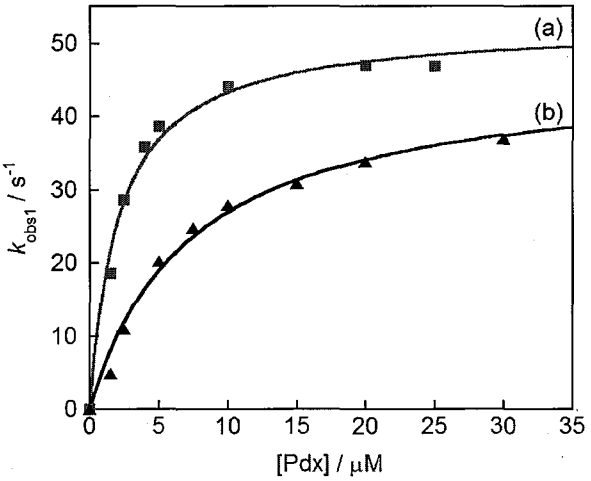

Figure 3-15. Observed first-order rates (k_{obs1}) for the ferric form reduction of (a) the wild-type (closed square) and (b) $rP450_{cam}$(**1**) (closed triangle) by reduced putidaredoxin versus concentration of reduced putidaredoxin in 50 mM KPi (pH 7.4) containing 100 mM KCl and 1 mM *d*-camphor at 20 °C.

Table 3-9. Kinetic and equilibrium parameters of the first electron transfer reaction[a]

Protein	k_{ET1} (s^{-1})	K_{m1} (μM)
rP450cam(**1**)	46 ± 2.4	7.3 ± 0.99
wt-P450cam	53 ± 1.6	2.1 ± 0.25

[a] pH 7.4 (50 mM KPi buffer containing 100 mM KCl and 1 mM *d*-camphor) at 20 °C.

NADH oxidation and product analysis. The rate constant of NADH oxidation by rP450cam(**1**) was found to be 1150 μM min^{-1}(μM enzyme)$^{-1}$, while the rate for wild-type P450cam is 1350 μM min^{-1}(μM enzyme)$^{-1}$ (Figure 3-17). The only product in the reaction with the rP450cam(**1**) was 5-*exo*-hydroxycamphor (Figure 3-16), and the NADH consumption was found to be tightly coupled to total product formation as seen in wild-type P450cam. These findings indicate that the enzyme activity is maintained despite the removal of the 6-propionate side chain from the heme framework.

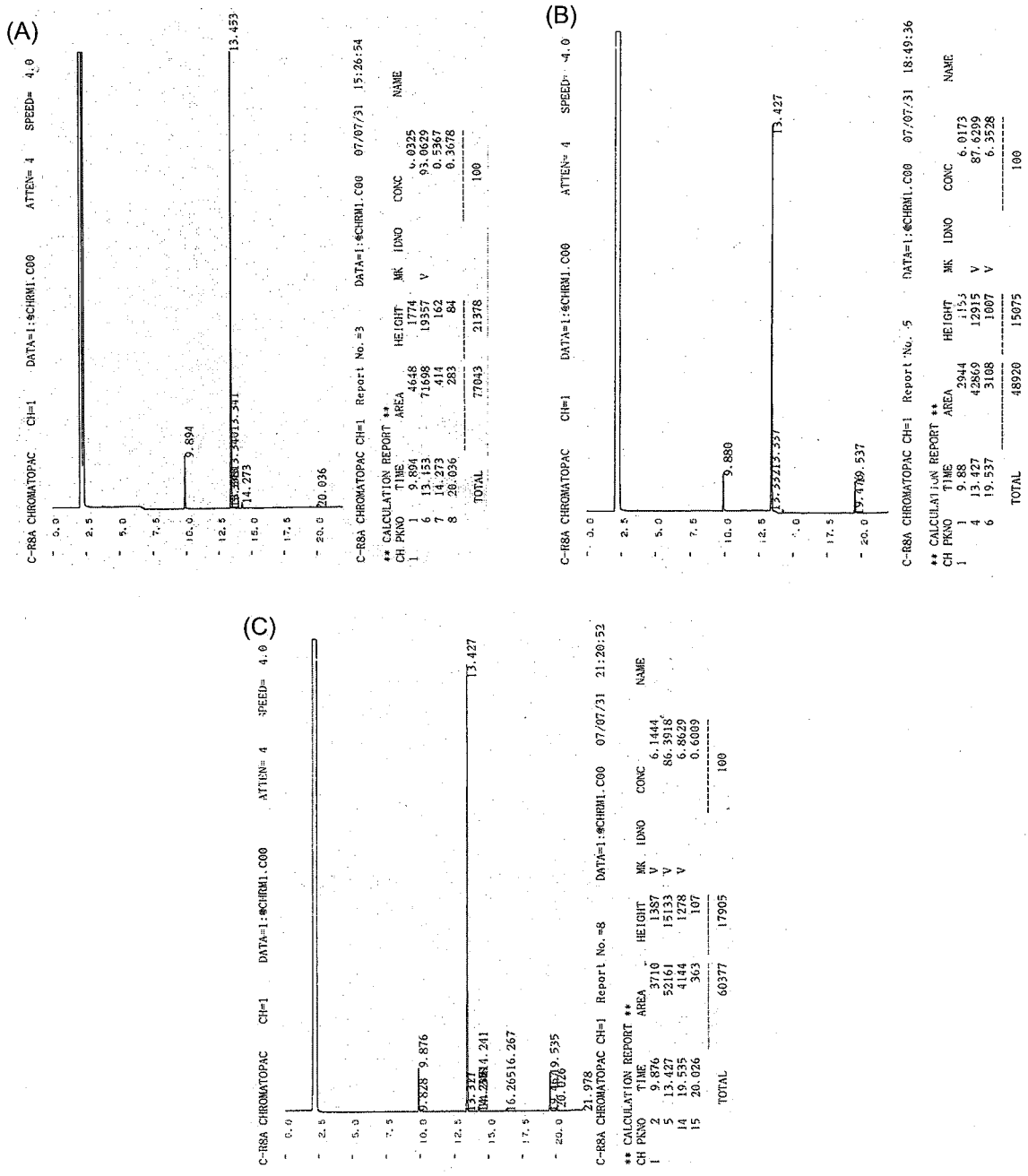

Figure 3-16. The transformation of *d*-camphor as monitored by GC. Under the conditions described in experimental section, the retention times were 9.9 min for benzyl alcohol, 13.4 min for *d*-camphor, and 19.5 min for 5-*exo*-hydroxycamphor. (A) Chromatogram obtained after the incubation of 14 μM Pdx, 0.12 μM PdR, 600 units/mL catalase, 200 units/mL SOD and 100 μM NADH in 50 mM KPi (pH 7.4) containing 100 mM KCl and 1 mM *d*-camphor at 20 °C for 15 min, (B) Chromatogram obtained after the incubation in the same conditions of (A) with 0.042 μM wild-type P450cam for 2 min, (C) Chromatogram obtained after the incubation in the same conditions of (A) with 0.038 μM rP450cam(**1**) for 2 min.

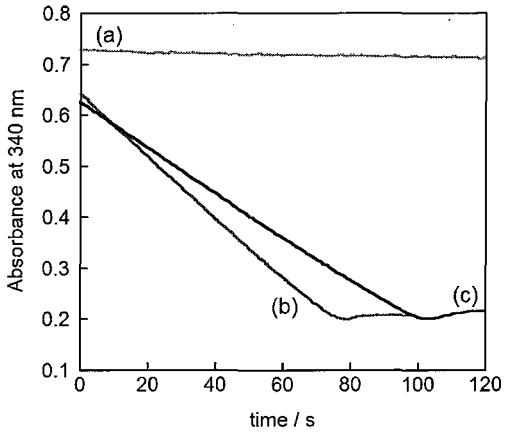

Figure 3-17. The NADH oxidation by the wild-type and rP450cam(**1**) in a reconstituted system. (a) The trace obtained after the incubation of 14 μM Pdx, 0.12 μM PdR, 600 units/mL catalase, 200 units/mL SOD and 100 μM NADH in 50 mM KPi (pH 7.4) containing 100 mM KCl and 1 mM *d*-camphor at 20 °C, (b) The trace obtained after the incubation in the same conditions of (a) with 0.042 μM wild-type P450cam, (c) The trace obtained after the incubation in the same conditions of (a) with 0.038 μM rP450cam(**1**).

Table 3-10. NADH oxidation rate and coupling ratio[a]

protein	NADH oxidation rate (μM min^{-1}(μM enzyme)$^{-1}$)	coupling ratio[b] (%)
rP450cam(**1**)	$(1.15 \pm 0.05) \times 10^3$	100
wt-P450cam	$(1.35 \pm 0.05) \times 10^3$	100

[a] pH 7.4 (50 mM KPi buffer containing 100 mM KCl and 1 mM *d*-camphor with 14 μM Pdx, 0.12 μM PdR, 600 units/mL catalase, 200 units/mL SOD) at 20 °C. [b] Ratio between the hydroxylated product (5-*exo*-hydroxycamphor) and NADH oxidized.

The conversion from P450 to P420 species. The reconstituted ferric P450cam, rP450cam(**1**), was converted into an inactive species at 25 °C with a half-life of 300 min at a protein concentration of 2 μM (Figure 3-19) with a set of isosbestic points (Figure 3-18). The final UV–vis spectrum which exhibits maxima at 369, 416, and 540 nm is similar to that obtained by pressure-induced ferric P420cam (Figure 3-18) [33, 34]. On the other hand, no clear decay was observed for the wild-type ferric protein under these conditions (Figure 3-19).

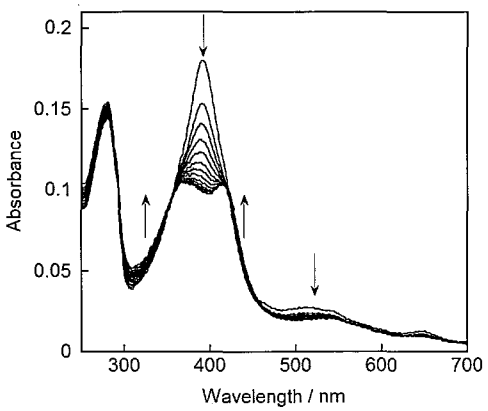

Figure 3-18. Spectral changes of rP450cam(**1**) (ca. 2 μM) over 26 h at 25 °C in 50 mM KPi buffer (pH 7.4) containing 1 mM *d*-camphor and 100 mM KCl.

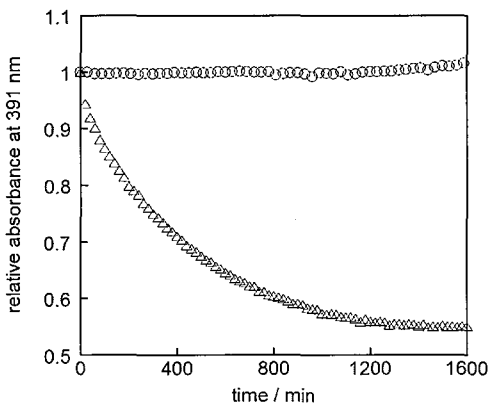

Figure 3-19. Time-dependent conversion of ferric P450 into an inactive P420 species for rP450cam(**1**) (open triangles) and wild-type P450cam (open circles), respectively, monitored at 391 nm in 50 mM KPi buffer (pH 7.4) containing 100 mM KCl and 1 mM *d*-camphor at 25 °C. [P450cam] = 2 μM.

3-4. Discussion

Role of 6-propionate side chain in P450cam structure. The spectra of ferric, ferrous, oxy-, and CO-bound forms in the presence of 1 mM *d*-camphor and 100 mM KCl are comparable with the analogous spectra of the camphor-bound wild-type protein in the same conditions (Figure 3-6). Further, for the ferric rP450cam(**1**), the resonance Raman spectrum of the high-frequency region (Figure 3-7) and ^{1}H NMR spectrum of the downfield region (Figure 3-12) are comparable with analogous spectra of the camphor-bound wild-type protein. This suggests that removal of the 6-propionate side chain does not have a serious influence on the electronic and structural properties of the heme, and that the thiolate of Cys357 is ligated to the heme iron of the one-legged heme **1** as seen in the wild-type protein.

Role of 6-propionate side chain in the electron transfer event. The rate constant of NADH oxidation by rP450cam(**1**) was found to be 1150 μM min^{-1}(μM enzyme)$^{-1}$, while the rate for wild-type P450cam is 1350 μM min^{-1}(μM enzyme)$^{-1}$ (Figure 3-17). The only product in the reaction with the rP450cam(**1**) was 5-*exo*-hydroxycamphor (Figure 3-16), and the NADH consumption was found to be tightly coupled to total product formation as seen in wild-type P450cam. These findings indicate that the enzyme activity is maintained despite the removal of the 6-propionate side chain from the heme framework. In contrast, the Pdx affinity for the rP450cam(**1**) is approximately 3.5-fold weaker than that observed for the wild-type protein, although the electron-transfer rate from reduced Pdx to ferric P450cam was found to be similar for both proteins (Figure 3-15, Table 3-9). These results indicate that the lack of the 6-propionate side chain has a slight influence on the Arg112–Pdx binding event. Although the decrease of the Pdx affinity for rP450cam(**1**) could originate from perturbation of the Arg112 residue and other residues in the general vicinity, a clear difference in the geometry of Arg112 between both rP450cam(**1**) and wild-type enzyme was not seen (Figure 3-13). This is probably due to the presence of the chloride ion that replaces the 6-propionate side chain to retain the ion pair interaction and/or the formation of intermolecular tight salt-bridge with Asp202 in the crystals (Figure 3-20).

Role of 6-propionate side chain on the Fe–S bond. Surprisingly, the reconstituted ferric P450cam was converted into an inactive species at 25 °C with a half-life of 300 min at a protein concentration of 2 μM (Figure 3-19) (no clear decay was observed for the wild-type ferric protein under these conditions). The final UV–vis spectrum which exhibits maxima at 369, 416, and 540 nm is similar to that obtained by pressure-induced ferric P420cam (Figure 3-18) [33, 34]. This species, which is inactive toward the catalytic hydroxylation of *d*-camphor, is proposed to be the P420 structure derived from the protonation of the thiolate of Cys357 in P450cam [34, 35]. In contrast to wild-type P450cam, the thiolate of Cys357 is partially visible from the molecular surface of the crystal structure of the rP450cam(**1**) (Figure 3-21). This suggests that bulk water could be accessible to Cys357 as a result of the removal of the 6-propionate side chain. Therefore, the rP450cam(**1**) is readily converted into the inactive P420 species as a result of facile protonation of the Cys357 thiolate. The resonance Raman spectra of the reconstituted P450cam in the low-frequency region excited at 363.8 nm showed the Fe–S stretching mode at 348 cm^{-1}, which is shifted 3

cm^{-1} lower relative to the corresponding band of the wild-type protein (Figure 3-10) [30(b)]. Thus, the lower frequency data provide evidence that the lack of the 6-propionate side chain induces weakening of the Fe–Cys357 ligation. This in turn suggests that lengthening of the Fe–S bond facilitates the conversion to the thiolate-protonated P420 form [36].

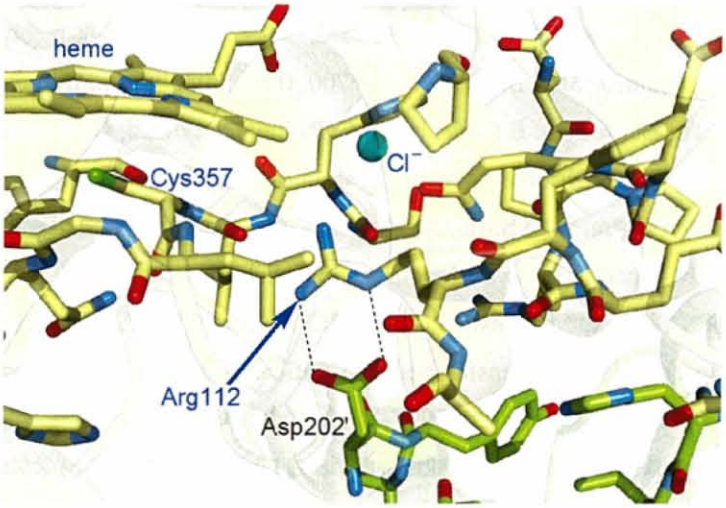

Figure 3-20. Structure of an interface between two rP450cam(**1**) molecules in the crystals (PDB ID: 2ZAW). Arg112 (C atom colored yellow) and Asp202' (C atom colored green) form an intermolecular salt-bridge with the distances of 2.80 and 2.91 Å.

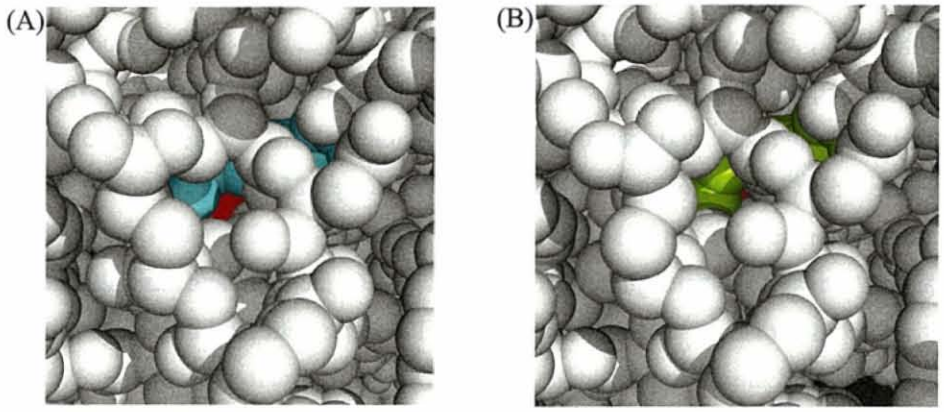

Figure 3-21. Protein surface views as a CPK model. (A) rP450cam(**1**) (PDB ID: 2ZAW) and (B) wild-type P450cam (PDB ID: 2ZAX). The thiolate of Cys357, the one-legged heme **1**, and wild-type heme were shown in red, cyan, and light green, respectively. Chloride ion was omitted for clarity, because the chloride affinity could not be high in the solution.

3-5. Summary

In summary, the present results clearly demonstrate two importamt functional roles of the heme-6-propionate side chains in cytochrome P450cam; fixation of the Pdx-binding site by the Arg112 residue, and stabilization of the Fe–S (thiolate) coordination to prevent the formation of the inactive P420 species. Particularly, the latter role indicates that the 6-propionate side chain–amino acid interaction is essential for P450cam to retain its enzyme activity.

References

1. Gunsalus, I. C., Meeks, J. R., Lipscomb, J. D., Debrunner, P., and Munck, E. (1974) in *Molecular Mechanism of Oxygen Activation* (Hayaishi, O., Eds.) pp 559–613, Academic Press, New York.
2. Schneider, S., Marles-Wright, J., Sharp, K. H., and Paoli, M. (2007) Diversity and conservation of interactions for binding heme in b-type heme proteins, *Nat. Prod. Rep. 24*, 621–630.
3. (a) Poulos, T. L., Finzel, B. C., and Howard, A. J. (1987) High-resolution crystal structure of cytochrome P450cam, *J. Mol. Biol. 195*, 687–700. (b) Schlichting, I., Berendzen, J., Chu, K., Stock, A. M., Maves, S. A., Benson, D. E., Sweet, R. M., Ringe, D., Petsko, G. A., and Sligar, S. G. (2000) The catalytic pathway of cytochrome P450cam at atomic resolution, *Science 287*, 1615–1622.
4. Manna, S. K., and Mazumdar, S. (2006) Role of threonine 101 on the stability of the heme active site of cytochrome P450cam: Multiwavelength circular dichroism studies, *Biochemistry 45*, 12715–12722.
5. Roitberg, A. E., Holden, M. J., Mayhew, M. P., Kurnikov, I. V., Beratan, D. N., and Vilker, V. L. (1998) Binding and electron transfer between putidaredoxin and cytochrome P450cam. Theory and experiments, *J. Am. Chem. Soc. 120*, 8927–8932.
6. Unno, M., Shimada, H., Toba, Y., Makino, R., and Ishimura, Y. (1996) Role of Arg^{112} of cytochrome $P450_{cam}$ in the electron transfer from reduced putidaredoxin, *J. Biol. Chem. 271*, 17869–17874.
7. Imai, M., Shimada, H., Watanabe, Y., Matsushima-Hibiya, Y., Makino, R., Koga, H., Horiuchi, T., and Ishimura, Y. (1989) Uncoupling of the cytochrome P-450cam monooxygenase reaction by a single mutation, threonine-252 to alanine or valine: A possible role of the hydroxy animo acid in oxygen activation, *Proc. Natl. Acad. Sci. USA 86*, 7823–7827.
8. Gunsalus, I. C., and Wagner, G. C. (1978) Bacterial $P\text{-}450_{cam}$ methylene monooxygenase components: Cytochrome *m*, putidaredoxin, and putidaredoxin reductase, *Methods Enzymol. 52*, 166–188.
9. Wagner, G. C., Perez, M., Toscano, W. A., Jr., and Gunsalus, I. C. (1981) Apoprotein formation and heme reconstitution of cytochrome $P\text{-}450_{cam}$, *J. Biol. Chem. 256*, 6262–6265.
10. private communication from R. Makino, et al.
11. Koga, H., Aramaki, H., Yamaguchi, E., Takeuchi, K., Horiuchi, T., and Gunsalus, I. C. (1986) *camR*, a negative regulator locus of the cytochrome $P\text{-}450_{cam}$ hydroxylase operon, *J. Bacteriol. 166*, 1089–1095.
12. Hintz, M. J., and Peterson, J. A. (1981) The kinetics of reduction of cytochrome $P\text{-}450_{cam}$ by reduced putidaredoxin, *J. Biol. Chem. 256*, 6721–6728.
13. Peterson, J. A., and Griffin, B. W. (1972) Carbon monoxide binding by *Pseudomonas putida* cytochrome P-450, *Arch. Biochem. Biophys. 151*, 427–433.
14. Brewer, C. B., and Peterson, J. A. (1988) Single turnover kinetics of the reaction between oxycytochrome $P\text{-}450_{cam}$ and reduced putidaredoxin, *J. Biol. Chem. 263*, 791–798.
15. (a) Mouro, C., Bondon, A., Jung, C., De Certaines, J. D., and Simonneaux, G. (2000) Assignment of heme methyl ^{1}H-NMR resonances of high-spin and low-spin ferric complexes of cytochrome P450cam using one-dimensional and two-dimensional paramagnetic signals enhancement (PASE) magnetization transfer experiments, *Eur. J. Biochem. 267*, 216–221. (b) Banci, L., Bertini, I., Marconi,

S., Pierattelli, R., and Sligar, S. G. (1994) Cytochrome P450 and aromatic bases: A ^{1}H NMR study, *J. Am. Chem. Soc. 116*, 4866–4873. (c) Wakasugi, K., Ishimori, K., and Morishima, I. (1996) NMR studies of recombinant cytochrome P450cam mutants, *Biochimie 78*, 763–770.

16. Otwinowsky, A., and Minor, W. (1997) Processing of X-ray diffraction data collected in oscillation mode, *Methods Enzymol. 276*, 307–326.
17. Vagin, A., and Teplyakov, A. (1997) *MOLREP*: an automated program for molecular replacement, *J. Appl. Cryst. 30*, 1022–1025.
18. Collaborative Computational Project, Number 4 (1994) The CCP4 Suite: Programs for Protein Crystallography, *Acta Cryst. D50*, 760–763.
19. Brünger, A. T. (1992) Free R value: A novel statistical quantity for assessing the accuracy of crystal structures, *Nature 355*, 472–475.
20. Emsley, P., and Cowtan, K. (2004) *Coot*: Model-building tools for molecular graphics, *Acta Cryst. D60*, 2126–2132.
21. (a) Murshudov, G., Vagin, A., and Dodson, E. (2004) in the Refinement of Protein structures, Proceedings of Daresbury Study Weekend. (b) Murshudov, G. N., Vagin, A. A. and Dodson, E. J. (1997) Refinement of macromolecular structures by the maximum-likelihood method, *Acta Cryst. D53*, 240–255. (c) Pannu, N. S., Murshudov, G. N., Dodson, E. J., and Read, R. J. (1998) Incorporation of prior phase information strengthens maximum-likelihood structure refinement, *Acta Cryst. D54*, 1285–1294. (d) Murshudov, G. N., Vagin, A. A., Lebedev, A., Wilson, K. S., and Dodson, E. J. (1999) Efficient anisotropic refinement of macromolecular structures using FFT, *Acta Cryst. D55*, 247–255. (e) Winn, M. D., Isupov, M. N., and Murshudov, G. N. (2001) Use of TLS parameters to model anisotropic displacements in macromolecular refinement, *Acta Cryst. D57*, 122–133.
22. DeLano, W. L. (2002) *The PyMOL Molecular Graphics System*, DeLano Scientific, San Carlos, CA.
23. Wagner, G. C., Gunsalus, I. C., Wang, M.-Y. R., and Hoffman, B. M. (1981) Cobalt-substituted cytochrome P-450$_{cam}$, *J. Biol. Chem. 256*, 6266–6273.
24. (a) Gelb, M. H., Toscano, W. A., Jr., and Sligar, S. G. (1982) Chemical mechanisms for cytochrome P-450 oxidation: Spectral and catalytic properties of a manganese-substituted protein, *Proc. Natl. Acad. Sci. USA 79*, 5758–5762. (b) Makris, T. M., Koenig, K., Schlichting, I., and Sligar, S. G. (2006) The status of high-valent metal oxo complexes in the P450 cytochromes, *J. Inorg. Biochem. 100*, 507–518.
25. Makino, R., Iizuka, T., Sakaguchi, K., and Ishimura, Y. (1982) Effects of heme substitution on the activity of heme-containing oxygenases, in *Oxygenase and oxygen metabolism* (Nozaki, M., Yamamoto, S., Ishimura, Y., Coon, M. J., and Ernster, L., Eds.) pp 467–477, Academic Press, New York.
26. Kobayashi, K., Amano, M., Kanbara, Y., and Hayashi, K. (1987) One-electron reduction of the oxyform of 2,4-diacetyldeuterocytochrome P-450$_{cam}$, *J. Biol. Chem. 262*, 5445–5447.
27. Furukawa, Y., Ishimori, K., and Morishima, I. (2000) Electron transfer reactions in Zn-substituted cytochrome P450cam, *Biochemistry 39*, 10996–11004.

28. It is well known that under the present conditions, the wild-type protein is a *d*-camphor-bound high-spin species.
29. Kincaid, J. R. (2000) in *The Porphyrin Handbook* (Kadish, K. M., Smith, K., and Guilard, K. S., Eds.) Vol. 7, pp 225–291, Academic Press, San Diego.
30. (a) Uno, T., Nishimura, Y., Makino, R., Iizuka, T., Ishimura, Y., and Tsuboi, M. (1985) The resonance Raman frequencies of the Fe-CO stretching and bending modes in the CO complex of cytochrome P-450cam, *J. Biol. Chem. 260*, 2023–2026. (b) Wells, A. V., Li, P., Champion, P. M., Martinis, S. A., and Sligar, S. G. (1992) Resonance Raman investigations of *Escherichia coli*-expressed *Pseudomonas putida* cytochrome P450 and P420, *Biochemistry 31*, 4384–4393. (c) Yu, N.-T., Kerr, E. A., Ward, B., and Chang, C. K. (1983) Resonance Raman detection of Fe–CO stretching and Fe–C–O bending vibrations in sterically hindered carbonmonoxy "strapped hemes". A structural probe of Fe-C-O distortion, *Biochemistry 22*, 4534–4540.
31. (a) Champion, P. M., Stallard, B. R., Wagner, G. C., and Gunsalus, I. C. (1982) Resonance Raman detection of an Fe–S bond in cytochrome $P450_{cam}$, *J. Am. Chem. Soc. 104*, 5469–5472. (b) Koo, L. S., Tschirret-Guth, R. A., Straub, W. E., Moënne-Loccoz, P., Loehr, T. M., and Ortiz de Montellano, P. R. (2000) The active site of the thermophilic CYP119 from *Sulfolobus solfataricus*, *J. Biol. Chem. 275*, 14112–14123. (c) Schelvis, J. P. M., Berka, V., Babcock, G. T., and Tsai, A.-L. (2002) Resonance Raman detection of the Fe–S bond in endothelial nitric oxide synthase, *Biochemistry 41*, 5695–5701.
32. The PDB codes of the wild-type and reconstituted proteins are 2ZAX and 2ZAW, respectively.
33. The conversion of P450 into P420 form was directly confirmed by monitoring the CO-form of the aliquots sampled from the protein solution using a UV–vis spectrophotometer.
34. Martinis, S. A., Blanke, S. R., Hager, L. P., Sligar, S. G., Hui Bon Hoa, G., Rux, J. J., and Dawson, J. H.(1996) Probing the heme iron coordination structure of pressure-induced cytochrome $P420_{cam}$, *Biochemistry 35*, 14530–14536.
35. Perera, R., Sono, M., Sigman, J. A., Pfister, T. D., Lu, Y., and Dawson, J. H. (2003) Neutral thiol as a proximal ligand to ferrous heme iron: Implications for heme proteins that lose cysteine thiolate ligation on reduction, *Proc. Natl. Acad. Sci. U.S.A. 100*, 3641–3646.
36. P420 can be produced by increased temperature or pressure, exposure to organic solvents, and extremes of pH. Ligand exchange to histidine from cysteine might occur to form P420 by these drastic procedures. However, the occurrence of histidine ligation is less likely for the present conversion observed at 25 °C, which includes a set of isosbestic points (Figure 3-18).

Chapter 4

Heme-7-Propionate Side Chain is a Water Gate Essential to Substrate-Induced Cytochrome P450cam Activation

4-1. Introduction

Monooxygenase cytochrome P450cam (P450cam), which catalyzes 5-*exo*-hydroxylation of *d*-camphor, binds protoheme IX (heme) as a prosthetic group via multiple noncovalent interactions. The resting state of the enzyme has a ferric low-spin heme with a coordinated water molecule and a unique water cluster at the substrate binding side of the heme (Figure 4-1(A)) [1–3]. The water cluster is expelled from the active site upon binding of *d*-camphor to generate a 5-coordinated high-spin heme (Figure 4-1(B)) [4, 5] with concurrent increase in redox potential of the heme iron. The positively shifted redox potential allows an efficient reduction by the electron transfer system of the ferric heme to the ferrous heme. Therefore, the water exclusion is the critical initial step of the P450cam catalytic cycle (Figure 4-2). The crystal structures of the ferric enzyme reveal a narrow space extending from the active site to the surface of the enzyme molecule. However, the space is known to be a channel for *d*-camphor to penetrate into the active site [6]. Therefore it is unlikely that this channel permits the water exodus upon binding of the substrate [3–5]. In contrast, a theoretical study postulated that the water molecules could be expelled through a space transiently formed by a cleavage of the 7-propionate–Arg299 salt-bridge due to a metastable rotamer of the Arg299 residue [7], although any experimental evidences for the rotamer of Arg299 have never been provided. In general, a heme-propionate side chain in various hemoproteins has been regarded as a simple anchor that connects the heme prosthetic group to the protein matrix [8]. To evaluate the structural and functional roles of the 7-propionate side chain in P450cam, the author prepared the reconstituted P450cam protein with a "one-legged heme" **2** whose 7-propionate side chain was removed from the heme by organic synthesis technique [9]. Here, the author will report an important functional role of the 7-propionate side chain in regulation of the P450cam catalytic activity.

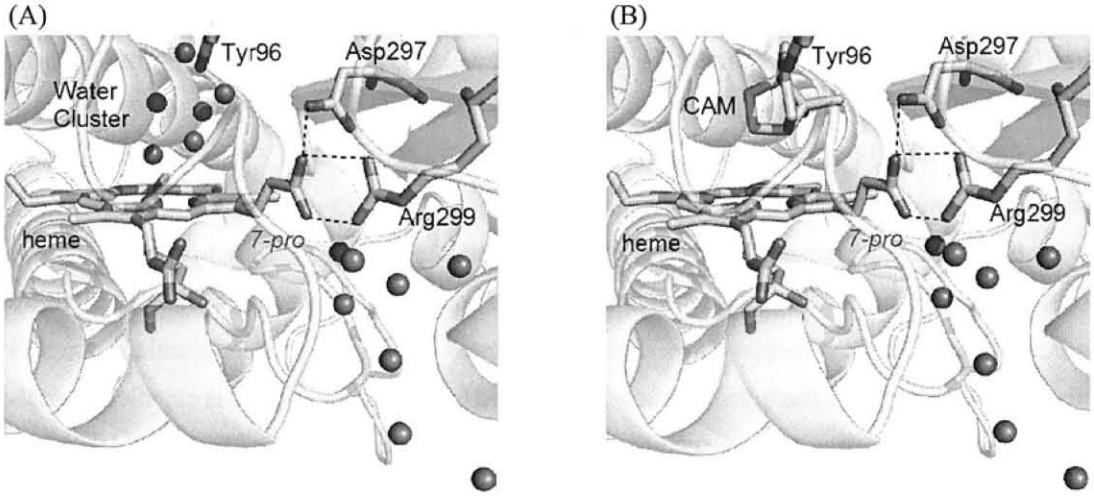

Figure 4-1. Crystal structures of (A) camphor-free (PDB ID: 1PHC) and (B) camphor-bound (PDB ID: 2CPP) wild-type ferric P450cams.

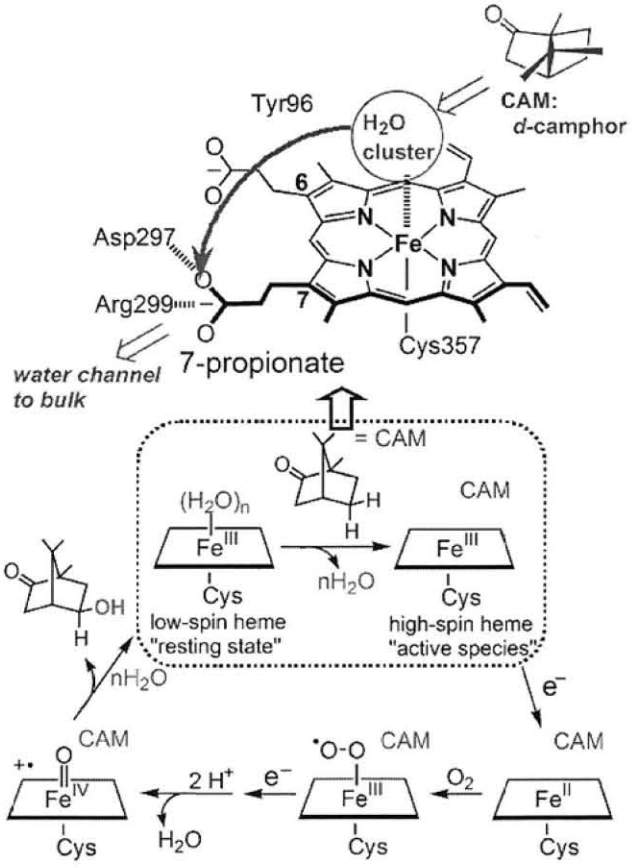

Figure 4-2. Catalytic mechanism of *d*-camphor hydroxylation by cytochrome P450cam and water cluster exclusion upon binding of *d*-camphor.

4-2. Experimental Section

4-2-1. Instruments

^{1}H NMR spectra were collected on a Bruker DPX400 (400 MHz) NMR spectrometer. ^{1}H NMR chemical shift values are indicated in ppm relative to the residual solvent resonance. The UV–visible experiments were conducted using a Shimadzu UV-3150 double beam spectrophotometer equipped with a thermostated cell holder having a 0.1 °C deviation. The mass analysis of the proteins was carried out using a TOF mass spectrometer equipped with electrospray ionization on an Applied Biosystems Mariner API-TOF workstation. The equipment for resonance Raman spectroscopy and X-ray crystallographic analysis is described below. Kinetic measurements for the reduction of the proteins were carried out using a stopped-flow system made by Unisoku, Co., Ltd. (Osaka, Japan). The product analysis was performed using a Shimadzu GC-2014 gas chromatograph with a capillary column, DB-1 (J & W Scientific, 30 m × 0.25 mm × 0.25 μm). The pH values were monitored by a HORIBA F-52 pH meter. The reconstitution of P450cam was carried out in an MB120B-G glove box (M.Braun Inertgas-Systeme GmbH, Germany) equipped with an MCPD-3000 Multi Channel Photo Detector and UV/VIS light source (MC-2530) using optical fibers (Otsuka Electronics Co., Ltd, Japan).

4-2-2. Materials

All reagents of the highest guaranteed grade available were obtained from commercial sources and were used as received unless otherwise indicated. Distilled water was demineralized by a Barnstead NANOpure DIamond^{TM} apparatus. The one-legged heme **2** was synthesized by the method described in chapter 1 of this thesis. The proteins were purified by column chromatography through a DE-52 (Whatman), Sephacryl S-200 (Amersham Biosciences), Sephadex G-25 (Amersham Biosciences), and Blue Sepharose 6 Fast Flow (Amersham Biosciences) column.

4-2-3 Methods

Characterization of reconstituted P450cam. The protein was first characterized by UV–vis spectroscopy. Since it is well known that the CO-bound P450cam exhibits the characteristic Soret band at 446 nm, the protein sample was reduced by addition of dithionite to yield the CO-bound species under a CO atmosphere. The difference spectrum between the CO-bound and reduced forms of the reconstituted protein showed a λ_{max} at 446 nm, indicating that the thiolate of the Cys357 was ligated to the heme iron of the one-legged heme as seen in the wild-type protein.

The ESI-TOF mass spectrum of the reconstituted protein displayed two peaks at 46541.7 and 47102.8 after deconvolution of the raw data. These numbers are assigned as the apo and reconstituted P450cams (the calculated mass numbers are 46542.89 and 47101.34, respectively).

Preparation of camphor-free P450cam. The camphor-free sample was prepared by passing the camphor-bound P450cam through a G25 column equilibrated with 50 mM Tris-HCl (pH 7.4). The buffer of the eluted sample was exchanged to 20 mM potassium phosphate buffer at pH 7.4 containing 100 mM KCl for the titration experiment or 50 mM potassium phosphate buffer at pH 7.4 containing 100 mM KCl for the measurements of resonance Raman spectroscopy.

d-Camphor affinity determination. 3 mL of camphor-free wild-type P450cam solution (ca. 1.7 μM in 20 mM KPi (pH 7.4) containing 100 mM KCl) in 10 mm quarz cell was titrated with aliquots of 3 mM *d*-camphor in 20 mM KPi (pH 7.4) containing 100 mM KCl at 20 °C. Binding was followed by monitoring the decrease in absorbance at 417 nm. K_d value of wild-type P450cam for *d*-camphor was determined using a plot for an equation $\Delta A = \Delta A_\infty$[substrate] / ([substrate] + K_d), where ΔA and ΔA_∞ are absorption changes upon addition of substrate at 0 < [substrate] < ∞ and [substrate] = ∞ (extrapolated), respectively, and [substrate] is free substrate concentration. The binding constant of reconstituted P450cam for *d*-camphor was not determined by titrimetric UV–vis measurement using the camphor-free reconstituted protein, because the reconstituted protein was readily converted into inactive P420 species during the titration at the low concentrations of *d*-camphor. Thus, the binding constant was estimated at three different *d*-camphor concentrations (0.25, 0.5 and 1 mM) using the low-spin (camphor-free) and high-spin (camphor-bound) populations obtained by the deconvolution of UV–vis spectrum; The camphor-free spectrum of the reconstituted protein was available, whereas the camphor-bound spectrum of the wild-type protein was used for the deconvolution, because the affinity of *d*-camphor was too low to obtain the *d*-camphor-bound reconstituted protein. The solubility of *d*-camphor under the experimental conditions is approximately 8 mM. The three independently obtained K_d values remained constant at 20 °C, pH 7.4 in the presence of 100 mM KCl.

NADH oxidation. The NADH oxidation was monitored by the change in the optical absorbance at 340 nm (an extinction coefficent of 6.22 $mM^{-1}cm^{-1}$) for NADH at 20 °C [10]. The reaction condition included the appropriate amount of P450cam (0.042 μM of wild-type P450cam and 0.96 μM of reconstituted P450cam), 100 μM NADH, 14 μM Pdx, 0.12 μM PdR in 50 mM KPi buffer (pH 7.4) containing 1 mM *d*-camphor, 100 mM KCl, 600 units/mL catalase and 200 units/mL SOD. The ratio of the rate constants of the NADH oxidation for the wild-type and the reconstituted proteins was independent of the NADH concentration (100–360 μM).

Crystallization of the reconstituted protein. Crystals of the reconstituted P450cam were grown using the sitting-drop vapor diffusion method. Crystallization was carried out on a VDX Plate™ with Micro-Bridges® (HAMPTON RESEARCH Corporation). A 700 μL aliquot of the buffer solution (50 mM Tris-HCl at pH 7.4 containing 250 mM KCl, 10 mM dithioerythritol (DTE) and 1 mM *d*-camphor) with 14% (w/v) PEG8000 (ICN Biomedicals, Inc.) was poured into the reservoir of the VDX Plate™. Next, the protein dissolved in the 6 μL of the same buffer solution with 14% (w/v) PEG8000 was poured into the well of the Micro-Bridges®. The plate was sealed with an acrylic tape and then placed at −5 °C for 2 days.

The obtained crystals were further soaked in a saturated amount of *d*-camphor solution containing 50 mM Tris-HCl at pH 7.4, 250 mM KCl and 10 mM DTE with 14.5% (w/v) PEG8000 for one day at −5 °C.

Data collection and structure refinement. The crystals were soaked in a cryoprotectant solution (5% hexylene glycol and after 30 min, 15% hexylene glycol in reservoir solution) and flash-frozen in liquid nitrogen. The X-ray diffraction data were collected at BL44XU in SPring-8, Hyogo, Japan. The data were indexed, integrated, scaled and merged using the program HKL2000 [11]. The data collection and refinement statistics are shown in Table 4-1. The initial phases of the reconstituted protein were obtained by the molecular replacement method of MOLREP [12] in the CCP4 program suite [13] using the wild-type camphor-bound P450cam as a search model [4]. The 5% randomly selected reflections were selected as test reflections for use in the free R cross-validation method throughout the refinement [14]. The model was manipulated using the program COOT [15], and refined with the program REFMAC5 [16] in the CCP4 program suite [13]. The figures were created with Pymol [17]. The atomic coordinates and structure factors have been deposited in the Protein Data Bank (entry 2Z97).

Energy minimization analysis by X-PLOR. The effect of the conformational change of Asp297 was predicted by energy minimization using the program X-PLOR [18]. The conformation of Asp297 was constrained to that of the reconstituted protein. The residues, Tyr75, Gln322, and Arg299, which were deviated from the wild-type structure (2CPP) in the reconstituted protein structure, were set to be free from constraint (residues 296−301 (except 297) and 318−327 were also set to be free from constraint.). The 7-propionate and its near by residue, His355 (and residues 351−356) were also set to be free from constraint.

Table 4-1. X-ray data collection and refinement statistics of the ferric rP450cam(**2**) (2Z97)

Data Collection	
X-ray source	SPring-8 BL44XU
detector	MAC Science DIP-6040 (Imaging Plate)
wavelength (Å)	0.7
resolution (Å)	50.00–1.80 (1.83–1.80)
space group	$P2_12_12_1$
unit cell parameters (Å)	a = 63.493, b = 66.124, c = 104.882
number of observations	309938 (15390)
number of unique reflections	41567 (2052)
completeness (%)	100.0 (100.0)
$I/\sigma(I)$	5.7 (4.0)
redundancy	7.5 (7.5)
Refinement	
resolution (Å)	30.63–1.80
total reflections	41488
number of non-H atoms	
protein	3421
water	713
other	51
R_{cryst} (%)	15.3
R_{free} (%)	20.3
r.m.s.d from target	
bond lengths (Å)	0.013
angle distances (Å)	1.764
mean isotropic equivalent B-factor (Å^2)	
all protein atoms	20.02
main-chain atoms	15.89
side-chain atoms	17.59
water molecules	35.96
protoheme	12.90
potassium ion	17.62

4-3. Results

Preparation and characterization of reconstituted cytochrome P450cam with 7-methyl-7-depropionated heme. Insertion of the one-legged heme **2** into apoP450cam was carried out according to the method described in chapter 3 of this thesis. The ESI-TOF mass spectrum of the reconstituted protein displayed two peaks at 46541.7 and 47102.8 after deconvolution of the raw data (Figure 4-3). These numbers are assigned as the apo and reconstituted P450cams (the calculated mass numbers are 46542.89 and 47101.34, respectively).

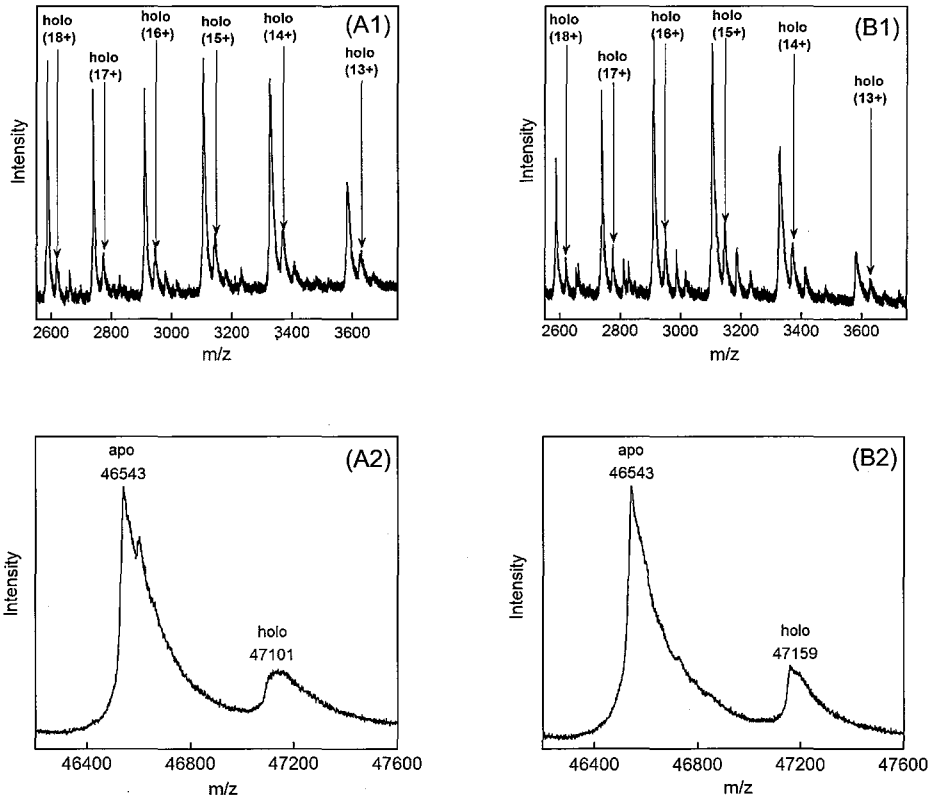

Figure 4-3. ESI-TOF mass spectra of $P450_{cam}$S in 5.7 mM ammonium acetate buffer containing 27% CH_3CN, 0.2% formic acid, 10% methanol. (A1) $rP450_{cam}$(**2**), (B1) wild-type $P450_{cam}$, deconvoluted mass spectra of $P450_{cam}$S (A2) $rP450_{cam}$(**2**), (B2) wild-type $P450_{cam}$. Experimental conditions: spray tip potential 4500 V, nozzle potential 200 V, nozzle temperature 140 °C, detector voltage 2350 V, sample infusion rate 5 μL/min.

Purified rP450cam(**2**) exhibited the ferrous CO-bound P450cam spectrum with the Soret peak at the characteristic wavelength at 446 nm (Figure 4-4(D)), indicating that the thiolate of the Cys357 was ligated to the heme iron of the one-legged heme as seen in the wild-type protein. In contrast, the UV–vis spectrum of the reconstituted ferric P450cam is comparable with that observed for the typical low-spin ferric P450cam species with maxima at wavelengths of 417, 540, and 570 nm in the presence of 1 mM *d*-camphor (Figure 4-4(A)), whereas the wild-type protein usually has a spectrum characteristic of the high-spin species with maxima at 391, 512, and 646 nm under the same conditions. Thus, the replacement of the 7-propionate side chain with the methyl group prevents conversion of the low-spin species to the high-spin species in spite of the addition of *d*-camphor. The content of high-spin state in the presence of 1 mM *d*-camphor and 100 mM KCl is estimated to be 26% based on deconvolution of the Soret band region using the UV–vis spectra of the camphor-free reconstituted protein and camphor-bound wild-type protein.

Under the same conditions, the spectrum of the wild-type protein shows the complete 5-coordinated high-spin heme species, although the low K^+ concentration has an influence on the substrate binding affinity [19]. The ferrous P450cams were obtained by dithionite reduction in a glove box. The CO forms were prepared by flushing the ferric forms with pure CO gas before a small amount of dithionite was added. The oxygenated enzymes (oxy-P450cams) were prepared by mixing the solution of ferrous enzyme with an equal volume of O_2 saturated buffer at 4 °C. These spectra, except for that of ferric form, are comparable with the analogous spectra of the camphor-bound wild-type protein. This suggests that removal of the 7-propionate side chain does not have a serious influence on the electronic and structural properties of the heme. The absorption maxima for the various species of the P450cams are summarized in Table 4-2.

Table 4-2. Absorption maxima for $P450_{cam}$s

	λ_{max} (nm)			
protein	ferric-$P450_{cam}$	ferrous-$P450_{cam}$	oxy-$P450_{cam}$[c]	CO-$P450_{cam}$
$rP450_{cam}$(**2**) (+cam)[a]	417, 540, 570	410, 548	420, 556	446, 550
wt-$P450_{cam}$ (+cam)[a]	391, 512, 646	409, 545	420, 555	446, 550
wt-$P450_{cam}$ (−cam)[b]	417, 535, 569	408, 540[d]		447, 550[d]

[a] pH 7.4 (50 mM potassium phosphate buffer containing 100 mM KCl and 1 mM *d*-camphor) and 20 °C.
[b] pH 7.4 (20 mM potassium phosphate buffer containing 100 mM KCl) and 20 °C. [c] at 4 °C.
[d] pH 7.0 (50 mM potassium phosphate buffer) and 25 °C from ref. [20].

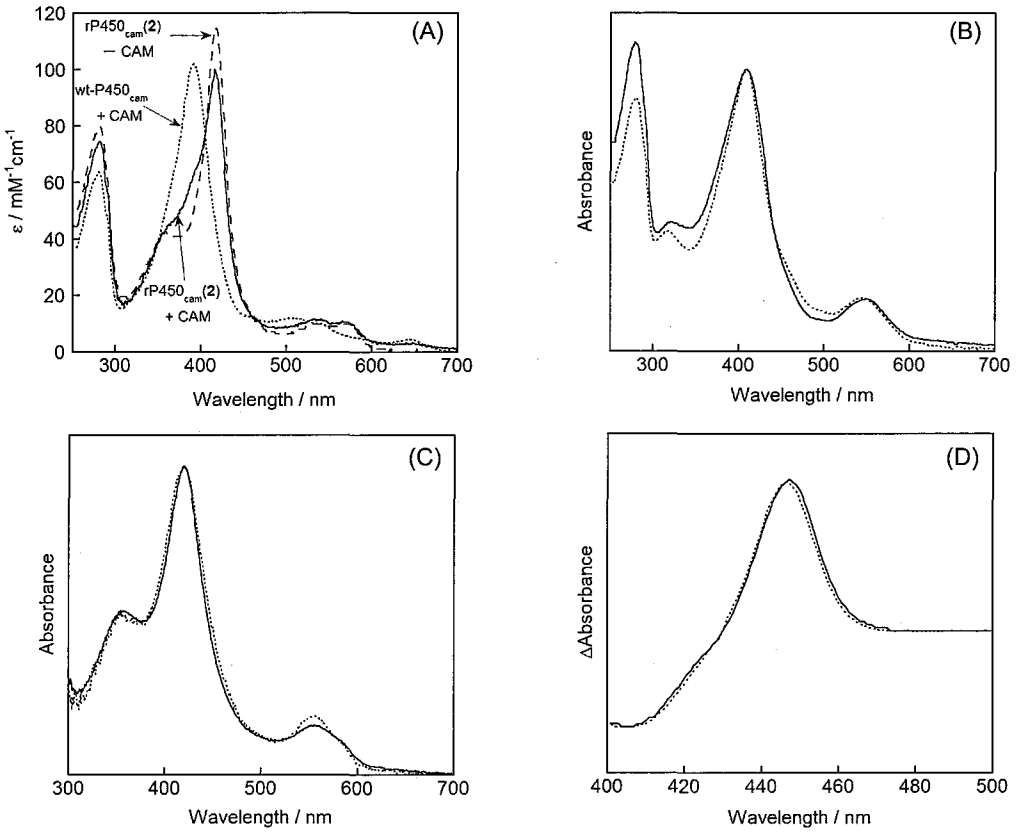

Figure 4-4. Absorption spectra of $rP450_{cam}$(**2**) (solid line) and wild-type $P450_{cam}$ (dotted line) in 50 mM KPi (pH 7.4) containing 100 mM KCl and 1 mM *d*-camphor at 20 °C. (A) ferric-$P450_{cam}$s, (B) ferrous-$P450_{cam}$s, (C) oxy-$P450_{cam}$s (at 4 °C), (D) difference spectra between CO- and ferrous-$P450_{cam}$s.

High-frequency resonance Raman spectra of ferric P450cams excited at 413.1 nm. In the high-frequency range, the spectra are dominated by the stretching porphyrin modes that are sensitive to spin state and coordination state of the iron. The visRR spectra in the high-frequency region, where skeletal stretching vibrations of prophyrin macrocycle appear, reflect the oxidation state, coordination number, and spin state of the heme iron. The ν_4 band at 1370–1375 cm^{-1} is an oxidation state marker. The ν_3 band at 1480–1510 cm^{-1} is an oxidation state, coordination number, and spin state marker. The ν_2 band at 1565–1585 cm^{-1} is a spin state marker. In the all samples, the oxidation marker band ν_4 appeared in the 1371–1373 cm^{-1} regions, which indicates the ferric state. The ν_3 band for ferric camphor-free wild-type P450cam appeared at 1502 cm^{-1}, which corresponded to the six-coordinate ferric low-spin species. The ν_3 band for ferric camphor-bound wild-type P450cam appeared at 1487 cm^{-1}, which corresponded to the five-coordinate ferric high-spin species. The high-frequency resonance Raman spectrum of the ferric reconstituted P450cam exhibits two evident ν_3 bands at 1503 and 1489 cm^{-1} which are derived from the low-spin and high-spin species, respectively (Figure 4-5) [21].

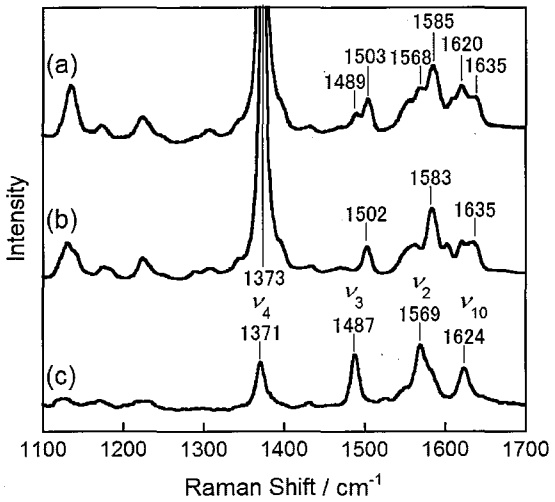

Figure 4-5. Resonance Raman spectra of ferric P450cams in 1100–1700 cm^{-1} region in 50 mM potassium phosphate buffer (pH 7.4) containing 1 mM *d*-camphor (except (b)) and 100 mM KCl at room temperature; (a) rP450cam(**2**) spectrum in the presence of 1 mM *d*-camphor and 100 mM KCl, (b) camphor-free wild-type P450cam spectrum, and (c) camphor-bound wild-type P450cam spectrum. The excitation wavelength was 413.1 nm and the laser power was 3 mW.

Table 4-3. Frequencies of resonance Raman lines (cm^{-1}) in the high-frequency region of the ferric form

protein	ν_4	ν_3	ν_2	ν_{10}
$rP450_{cam}$(**2**) (+cam)[a]	1373	1489, 1503	1568, 1585	1620, 1635
wt-$P450_{cam}$ (+cam)[a]	1371	1487	1569	1624
wt-$P450_{cam}$ (−cam)[b]	1373	1502	1583	1635

[a] pH 7.4 (50 mM KPi buffer containing 100 mM KCl and 1 mM *d*-camphor) at room temperature.
[b] pH 7.4 (50 mM KPi buffer containing 100 mM KCl) at room temperature.

Low-frequency resonance Raman spectra of ferric P450cams excited at 413.1 nm. The low-frequency region is sensitive to ruffling and other distortion in the porphyrin macrocycle. It is also sensitive to the conformational changes of the substituents [22]. The band located at 345 cm^{-1} is assigned to the ν_8(Fe–N) in-plane skeletal mode. The band located at 365 cm^{-1} is assigned to the $\gamma_6(A_{2u})$ out-of-plane mode associated with the pyrrole tilting vibration. The band at 314 cm^{-1} is assigned to the $\gamma_7(A_{2u})$ out-of-plane mode from methine wagging motion [22]. These two bands ($\gamma_6(A_{2u})$ and $\gamma_7(A_{2u})$) were observed only in the case of the camphor-bound wild-type P450cam. The band of the vinyl bending mode located at 426 cm^{-1} in the camphor-free wild-type P450cam was shifted to 422 cm^{-1} in the camphor-bound wild-type P450cam and 421 cm^{-1} in the rP450cam(**2**), respectively. The band assigned to the porphyrin-propionate bending mode appeared at 380 cm^{-1} in the camphor-free and camphor-bound wild-type P450cam and 379 cm^{-1} in the rP450cam(**2**).

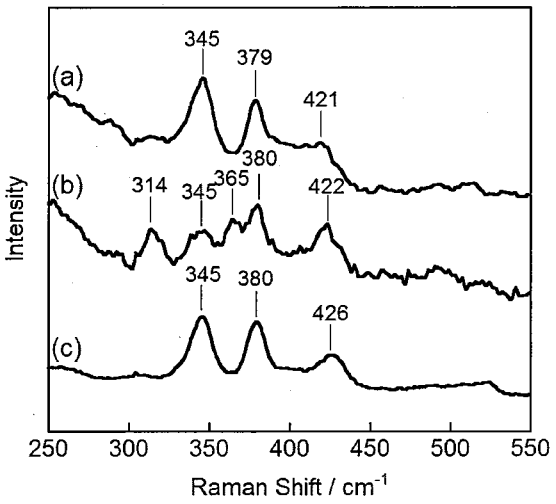

Figure 4-6. Resonance Raman spectra of ferric P450cams in 250–550 cm^{-1} region in 50 mM potassium phosphate buffer (pH 7.4) containing 1 mM *d*-camphor (except (c)) and 100 mM KCl at room temperature; (a) rP450cam(**2**) spectrum in the presence of 1 mM *d*-camphor and 100 mM KCl, (b) camphor-bound wild-type P450cam spectrum, and (c) camphor-free wild-type P450cam spectrum. The excitation wavelength was 413.1 nm and the laser power was 3 mW.

Table 4-4. Frequencies of resonance Raman lines (cm^{-1}) in the low-frequency region of the ferric form

protein	$\gamma_7(A_{2u})$	ν_8(Fe–N) A_{1g}	$\gamma_6(A_{2u})$	$\delta(C_\beta C_c C_d)$propionate	$\delta(C_\beta C_a C_b)$vinyl + $\delta(C_\beta CH_3)$ in-plane
$rP450_{cam}$(**2**) (+cam)[a]	—	345	—	379	421
wt-$P450_{cam}$ (+cam)[a]	314	345	365	380	422
wt-$P450_{cam}$ (–cam)[b]	—	345	—	380	426

[a] pH 7.4 (50 mM KPi buffer containing 100 mM KCl and 1 mM *d*-camphor) at room temperature.
[b] pH 7.4 (50 mM KPi buffer containing 100 mM KCl) at room temperature.

Low-frequency resonance Raman spectra of ferrous CO complex of P450cams excited at 441.6 nm. The Fe–CO stretching (ν_1) mode appeared at 465 cm^{-1} for ferrous CO complex of camphor-free wild-type P450cam. Furthermore, the Fe–CO stretching (ν_1) mode appeared at 485 cm^{-1} for ferrous CO complex of camphor-bound wild-type P450cam. Therefore, camphor binding to ferrous CO complex of camphor-free wild-type P450cam shifted Fe–CO stretching mode ($\Delta\nu$ = 20 cm^{-1}). The Fe–CO stretching (ν_1) mode appeared at 477 cm^{-1} for ferrous CO complex of camphor-bound $rP450_{cam}$(**2**) (Figure 4-7 and 4-8).

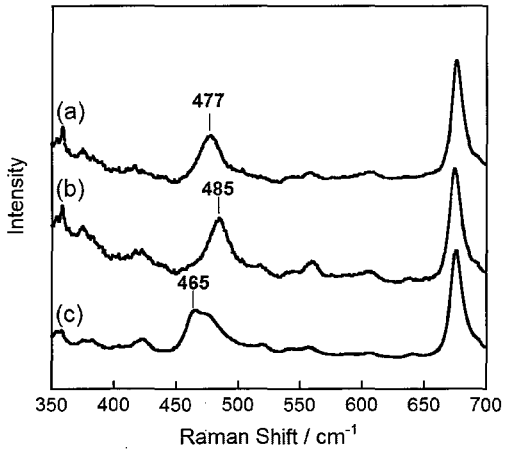

Figure 4-7. Resonance Raman spectra of CO-P450cams in 350–700 cm^{-1} region in 50 mM potassium phosphate buffer (pH 7.4) containing 1 mM *d*-camphor (except (c)) and 100 mM KCl at room temperature; (a) rP450cam(**2**) spectrum, (b) camphor-bound wild-type P450cam spectrum, and (c) camphor-free wild-type P450cam spectrum. The excitation wavelength was 441.6 nm and the laser power was 3 mW.

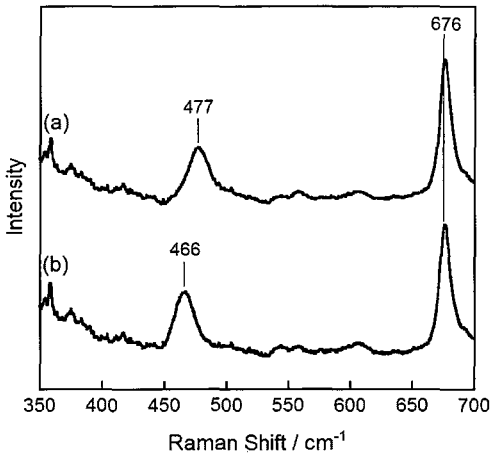

Figure 4-8. Resonance Raman spectra of CO-rP450cam(**2**) in 350–700 cm^{-1} region in 50 mM potassium phosphate buffer (pH 7.4) containing 1 mM *d*-camphor and 100 mM KCl at room temperature; (a) $^{12}C^{16}O$-rP450cam(**2**) spectrum and (b) $^{13}C^{18}O$-rP450cam(**2**) spectrum. The excitation wavelength was 441.6 nm and the laser power was 3 mW.

Resonance Raman spectra of ferric P450cams excited at 363.8 nm. The resonance Raman spectra of the rP450cam(**2**) in the low-frequency region excited at 363.8 nm showed the Fe–S stretching mode at 351 cm^{-1}, which is comparable to the corresponding band of the wild-type protein (Figure 4-9).

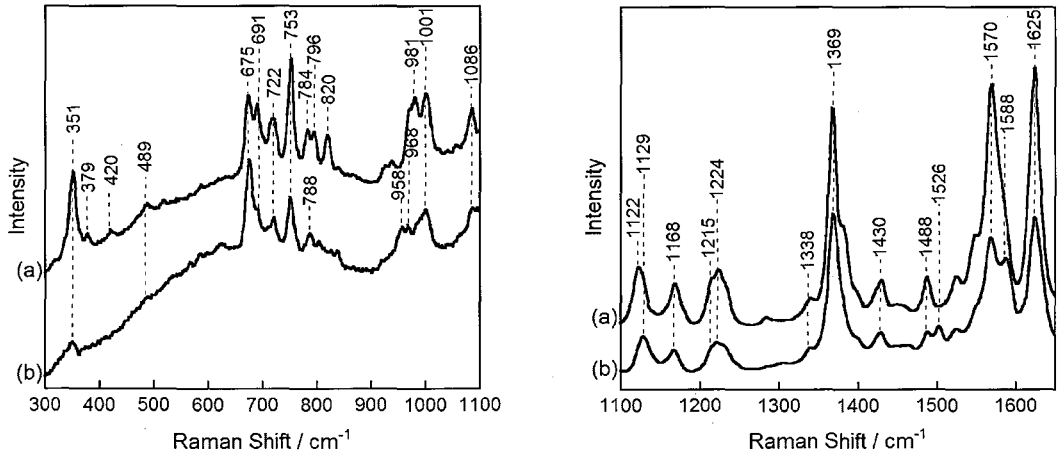

Figure 4-9. Resonance Raman spectra of ferric P450cams excited at 363.8 nm in 300–1100 cm^{-1} and 1100–1650 cm^{-1} regions in 50 mM potassium phosphate buffer (pH 7.4) containing 1 mM *d*-camphor and 100 mM KCl at room temperature; (a) camphor-bound wild-type P450cam and (b) rP450cam(**2**) spectrum. The excitation wavelength was 363.8 nm and the laser power was 6 mW.

Table 4-5. Frequencies of resonance Raman lines (cm^{-1}) for the Fe–CO stretching mode in the ferrous state and for the Fe–S stretching frequencies in the ferric state [a]

protein	ν_{Fe-CO}	ν_{Fe-S}
$rP450_{cam}$(**2**)	477	351
wt-$P450_{cam}$	485	351

[a] pH 7.4 (50 mM KPi buffer containing 100 mM KCl and 1 mM *d*-camphor) at room temperature.

d-Camphor affinity. Dissociation constant K_d value of *d*-camphor for the wild-type P450cam was determined at 20 °C by spectrophotometric titration in the presence of 100 mM KCl as shown in Figure 4-10. The K_d value obtained was 1.7 μM for wild-type P450cam. On the other hand, the binding constant of rP450cam(**2**) for *d*-camphor was not determined by titrimetric UV–vis measurement using the camphor-free reconstituted protein, because the reconstituted protein was readily converted into inactive P420 species during the titration at the low concentrations of *d*-camphor. Thus, the binding constant was estimated at three different *d*-camphor concentrations (0.25, 0.5, and 1 mM) (Figure 4-11) using the low-spin (camphor-free) and high-spin (camphor-bound) populations obtained by the deconvolution of UV–vis spectrum; The camphor-free spectrum of the reconstituted protein was available, whereas the camphor-bound spectrum of the wild-type protein was used for the deconvolution, because the affinity of *d*-camphor was too low to obtain the *d*-camphor-bound reconstituted protein. The solubility of *d*-camphor under the experimental conditions is approximately 8 mM. The dissociation constant of *d*-camphor is estimated to be 3 mM at pH 7.4, 20 °C (Table 4-6), indicating that the *d*-camphor affinity is dramatically reduced by approximately three orders of magnitude upon removal of the 7-propionate side chain. Thus, it is found that the 7-propionate side chain facilitates the high affinity of cytochrome P450cam for its substrate, *d*-camphor.

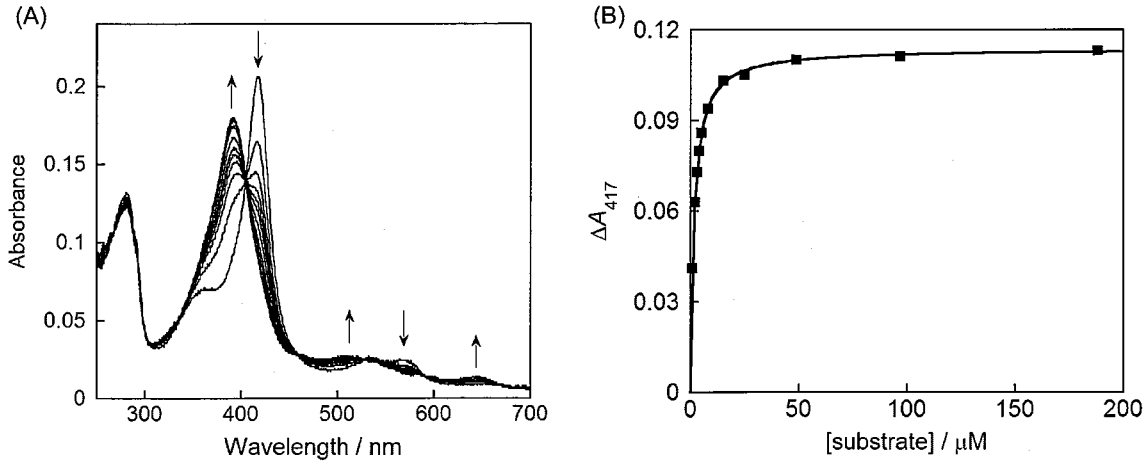

Figure 4-10. *d*-Camphor binding to the wild-type P450cam. Wild-type P450cam (ca. 1.7 μM) was titrated in 3.0 mL of 20 mM KPi (pH 7.4) buffer containing 100 mM KCl at 20 °C with 3 mM *d*-camphor dissolved in the same buffer.

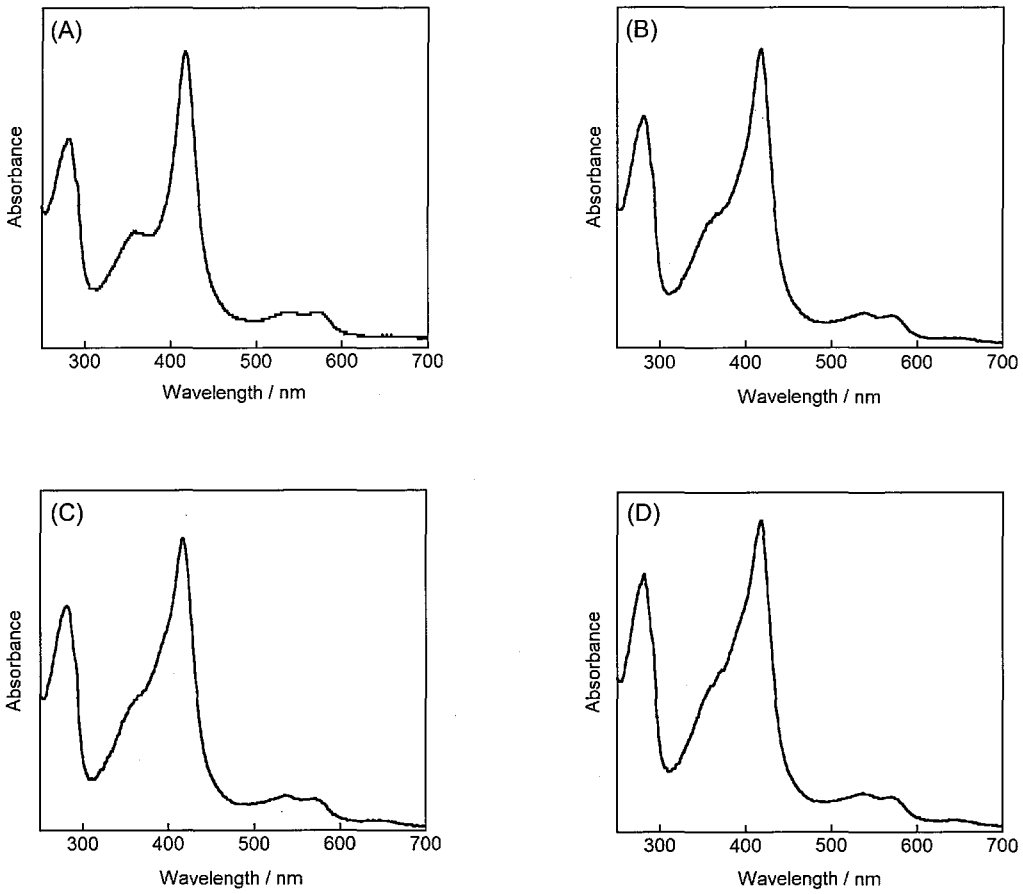

Figure 4-11. UV–vis spectral changes upon the addition of *d*-camphor into the solution of rP450cam(**2**) in the buffer of 50 mM KPi (pH 7.4) containing 100 mM KCl at 20 °C. *d*-Camphor concentrations are (A) 0 mM, (B) 0.25 mM, (C) 0.50 mM, and (D) 1.0 mM.

Table 4-6. High-spin population and dissociation constant of rP450cam(**2**)[a].

Concentration of *d*-camphor	High-spin population[b]	Apparent dissociation constant (K_d)[c]
0.25 mM	21%	0.94 mM
0.50 mM	24%	1.58 mM
1.0 mM	26%	2.85 mM

[a]conditions: 100 mM KCl, 50 mM KPi buffer, pH 7.4 at 20 °C. [b]The value was calculated from the deconvolution of the corresponding UV–vis spectrum based on the typical high-spin and low-spin spectra obtained by camphor-bound wild-type P450cam and camphor-free rP450cam(**2**), respectively. [c]The each dissociation constant which depends on the concentration of K^+ was estimated by the following equation: K_d = [camphor]$_0$•[(low spin population)•[P450cam]$_0$]/[(high spin population)•[P450cam]$_0$]. Errors in K_d < 15%.

d-Camphor affinity dependent on potassium ion (K^+) concentration. The amount of the high-spin state also increases with an increase in the concentration of KCl and the ratio of high-spin/low-spin is close to 60% at 1.0 M of KCl solution in the presence of 1 mM *d*-camphor (Figure 4-12, Table 4-7). It is known that the specific K^+ binding to P450cam has influence on the affinity of *d*-camphor, because the carbonyl oxygen of Tyr96 is one of the K^+ binding sites [19(a)]. In the case of the rP450cam(**2**), it is likely that the removal of the 7-propionate side chain may dramatically decrease the K^+ binding affinity with the deviation of Tyr96 residue and stabilize the water cluster in the heme pocket.

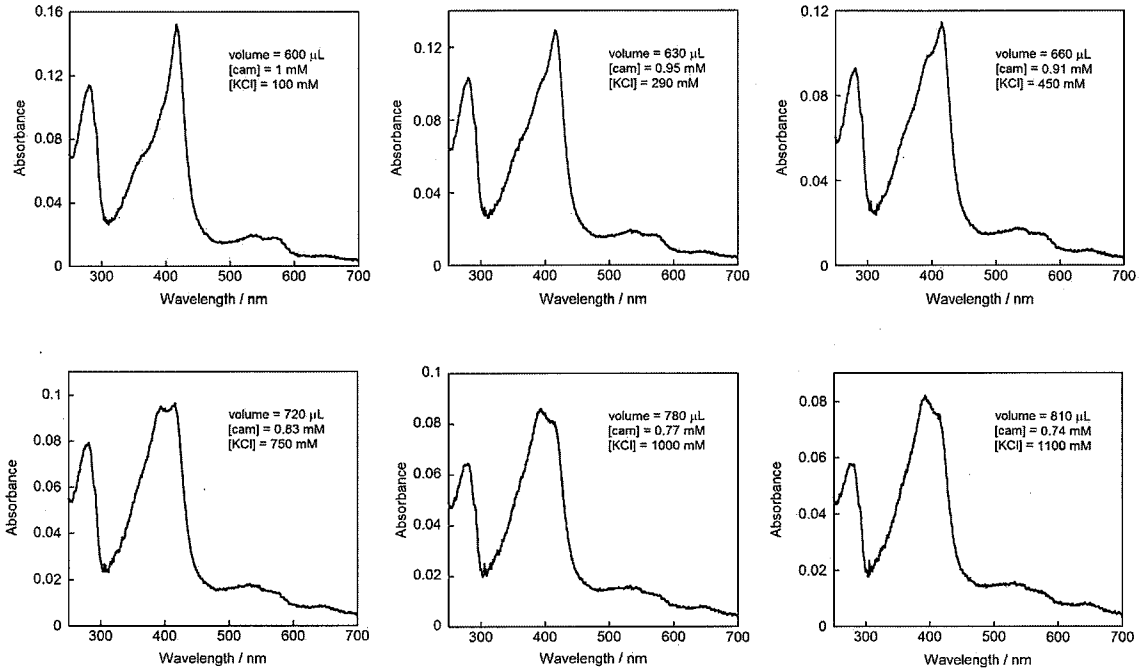

Figure 4-12. UV–vis spectral changes upon the addition of KCl into the solution of rP450cam(**2**) in the buffer of 50 mM KPi (pH 7.4) at 20 °C.

Table 4-7. High-spin population of rP450cam(**2**) at various concentration of KCl and *d*-camphor[a]

Concentration of KCl (mM)	High-spin population (%)[b]	Concentration of *d*-camphor (mM)
100	26	1
290	36	0.95
450	44	0.91
750	54	0.83
1000	59	0.77
1100	62	0.74

[a]conditions: 50 mM KPi buffer, pH 7.4 at 20 °C. [b]The value was calculated from the deconvolution of the corresponding UV–vis spectrum based on the typical high-spin and low-spin spectra obtained by camphor-bound wild-type P450cam and camphor-free rP450cam(**2**), respectively.

Proton nuclear magnetic resonance (^1H NMR) spectroscopy. Figure 4-13 shows the paramagnetic shifts of the heme substituents for the ferric and ferric cyanide-bound forms of wild-type P450cam and rP450cam(**2**) in 50 mM KPi (pD 7.8) containing 100 mM KCl and 1 mM *d*-camphor at 288 K. Camphor-bound ferric wild-type enzyme is in the high-spin state and shows the hyperfine shifted NMR peaks at 65.0, 60.6, 41.9, and 36.8 ppm, which have been assigned to 8-, 3-, 5-, and 1-methyl groups of the heme, respectively (Figure 4-13(a)) [23]. On the other hands, however, ferric rP450cam(**2**) showed no signals in the range from 30 to 70 ppm, showed very broad signals in the range from 12 to 24 ppm (Figure 4-13(c)). In the case of cyanide-bound wild-type enzyme, its heme is in the low-spin state and the sharp signals appear around the diamagnetic region (Figure 4-13 (b)). The peaks at 22.6 and 11.6 ppm for the wild-type enzyme have been assigned to 5- and 1-methyl groups of the heme, respectively [23]. In spite of the addition of excess KCN, rP450cam(**2**) showed very broad signals in the range from 12 to 30 ppm (Figure 4-13(d)). It is suggested that the spin state of the heme iron of rP450cam(**2**) is in both the high- and low-spin states in this condition. Furthermore, the exchange between high- and low-spin states may be faster than the time scale of ^1H NMR.

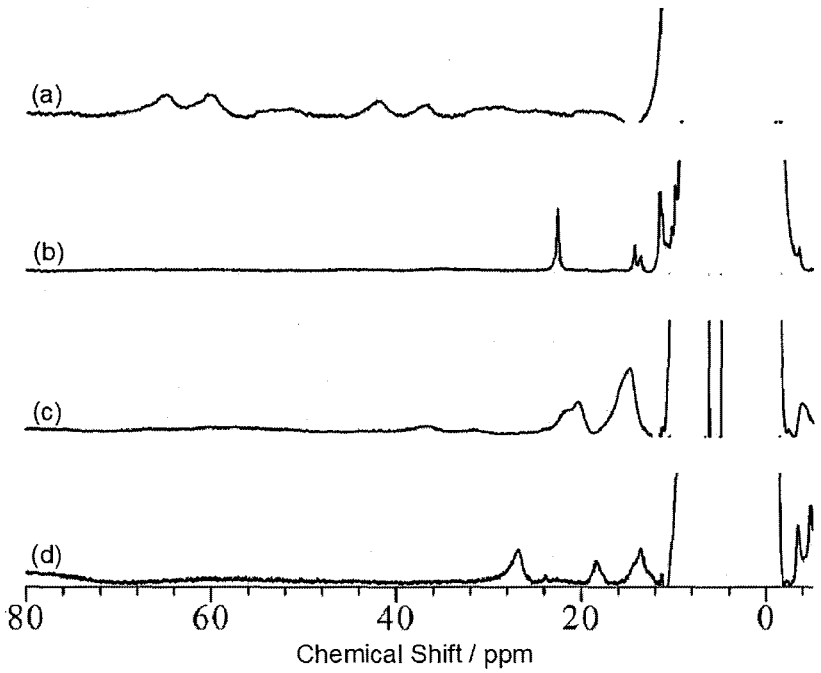

Figure 4-13. ^1H NMR spectra of ferric high-spin form for (a) wild-type P450cam and (c) rP450cam(**2**) and cyanide-bound ferric low-spin form for (b) wild-type P450cam and (d) rP450cam(**2**) in deuterated 50 mM KPi (pD 7.8) containing 100 mM KCl and 1 mM *d*-camphor at 288 K.

Crystal structure of the reconstituted P450cam with one-legged heme. The X-ray structure of the ferric rP450cam(**2**) at a resolution of 1.8 Å reveals that the asymmetric one-legged heme is incorporated into the heme pocket in the same plane and in essentially the same conformation as the heme of the wild-type protein (Figure 4-14(A)). These observations suggest that the lack of the 7-propionate side chain does not exert an influence on the structure and electronic properties of the heme in agreement with the spectroscopic data of P450cam. The polypeptide Cα atoms of both proteins are superimposable with a root-mean-square deviation of 0.507 Å. One notable difference is observed for Asp297, which is evidently deviated from its counterpart in the native structure. In addition, *d*-camphor binds to the substrate binding site with nearly the same conformation with that of the wild-type protein forming a characteristic hydrogen bond with Tyr96 and the C-5 atom faces toward the heme iron. However, *d*-camphor does not fully bind in the substrate binding site (vide infra).

The $F_o - F_c$ map focusing on the substrate binding site clearly shows electron densities that fit to a camphor molecule and two water molecules with occupancies of 0.25 and 0.75, respectively (Figure 4-14(B)). This indicates coexistence of two substrate binding site structures; the camphor-bound form and the camphor-free water-bound structure (their protein structures are crystallographically indistinguishable to each other). In the *d*-camphor-free structure, at least two distinct water molecules are located within the substrate binding site; WAT1028 is coordinated to the heme iron at a distance of 2.54 Å, while the other water molecule, WAT1033, is located within a hydrogen-bonding distance from WAT1028 (Figure 4-14(B) and Figure 4-15). These crystal data also indicate that the lack of the 7-propionate side chain obviously decreases the substrate affinity of the protein.

Relative to the camphor-bound and camphor-free forms of the wild-type protein, two additional water molecules (WAT1030 and 1031) are identified near Tyr96 and Asp297 of the reconstituted P450cam. Furthermore, a single water molecule (WAT1117) occupies the position of the 7-propionate carboxylate. As a result, a unique array of water molecules extending from the Tyr96 residue to the outside of the protein is observed in the crystal structure (Figure 4-14(C)). In the reconstituted protein, it is noted that the Asp297 residue is remarkably flipped and its side chain Oγ1 and Oγ2 atoms are located at the hydrogen bonding distance from WAT1030 and WAT1117 (Figure 4-16). This structural evidence suggests that the Asp297 residue may be capable of undergoing a large conformational change in the protein matrix and influenced to deviate from its native position by the influence of the water molecule array.

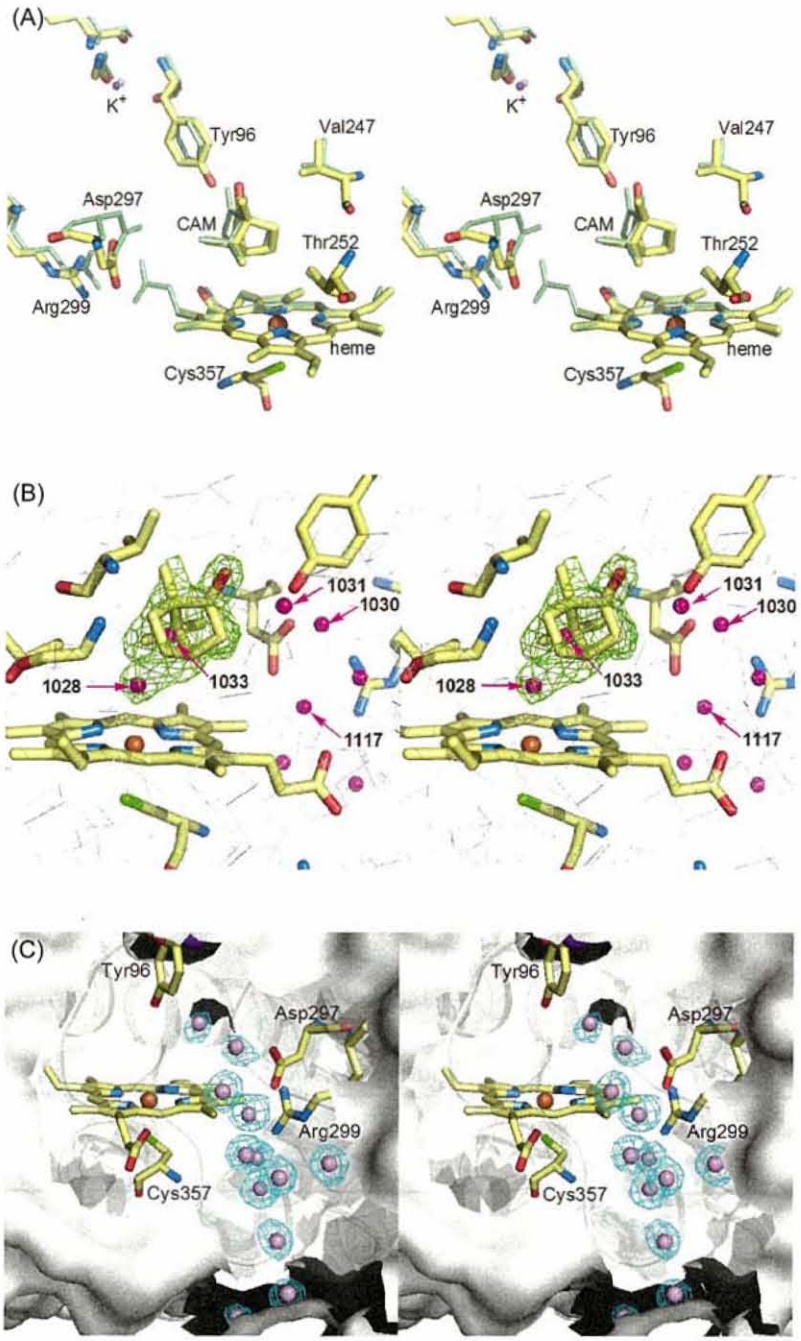

Figure 4-14. Crystal structure of ferric rP450cam(**2**) after one-day of soaking in the presence of *d*-camphor. All panels are stereopair representations. The characteristic water molecules in the crystals are also shown as spheres. (A) Superimposed structure of the rP450cam(**2**) (yellow; 2Z97) and wild-type (green; 2CPP) proteins. (B) Different view angle focusing on the heme pocket with the green F_o–F_c electron density map at 4.0σ. At least two water molecules, WAT1028 and WAT1033, were positioned into the F_o–F_c electron density map and refined together with camphor and the protein. *d*-Camphor binds at the substrate binding site with an occupancy of 0.25, whereas the coordinated WAT1028 and WAT1033 (see pink arrows) are located in the same area with an occupancy of 0.75. In addition, the map shows a slight mass of unassignable density when contoured at 3σ. (C) The structure of the water array and the heme pocket. The cyan $2F_o$–F_c map at 1.0σ is attached to each water molecules. For clarity, *d*-camphor and WAT1028, 1032, and 1033 are omitted. Occupancies and number designations of the representative water molecules are shown in Figure 4-15.

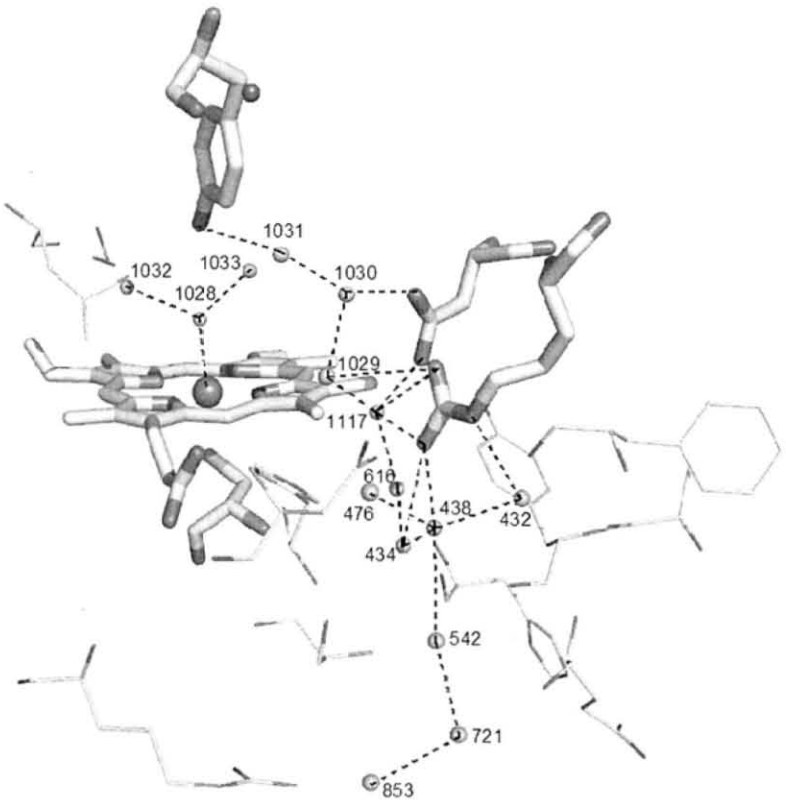

Figure 4-15. Water array structure of rP450cam(**2**) and several representative amino acids which interact with the water molecules. Spheres with numbers represent characteristic water molecules which contribute to the formation of the unique water channel network. For clarity, *d*-camphor is omitted in this figure. Occupancies of these molecules are as follows: WAT1028, 0.75; WAT1033, 0.75; WAT1030, 0.50; WAT1031, 0.30; WAT1032, 0.30; The other water molecules have the occupancy of 1.

Table 4-8. Geometry of rP450cam(**2**) and wild-type P450cams.

	rP450cam(**2**) (2Z97)	wild-type (1PHC)	wild-type (2CPP)
Sample	ferric	ferric camphor-free	ferric camphor-bound
Space group	$P2_12_12_1$	$P2_12_12_1$	$P2_12_12_1$
Unit cell parameters (Å)	a = 63.49, b = 66.12, c = 104.88	a = 108.67, b = 103.90, c = 36.38	a = 108.67, b = 103.90, c = 36.38
Resolution (Å)	1.80	1.60	1.63
Program	REFMAC 5	PROLSQ	PROLSQ
pH of crystal	7.4	7.0	7.0
r.m.s.d. of Cα (Å)	0.507 (2CPP)	0.162 (2CPP)	-----
Distances (Å)			
Cys 357 S − Fe	2.33	2.25	2.20
Water O − Fe	2.54	2.35	-----
Camphor C5 − Fe	4.21	-----	4.21
Tyr96 O − camphor O	2.85	-----	2.65

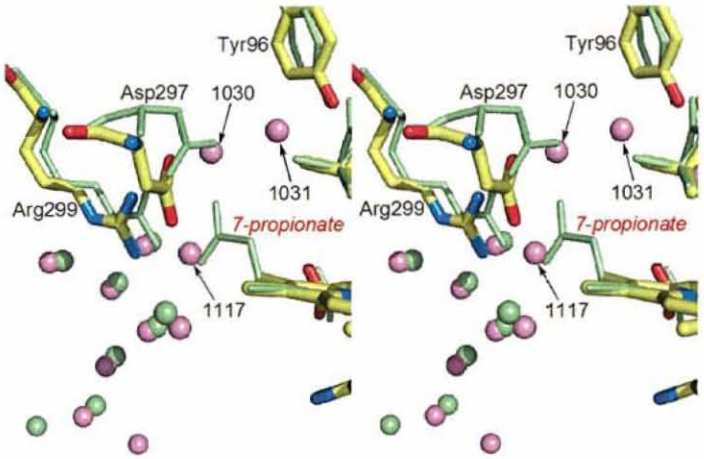

Figure 4-16. Superimposed structure (stereo image) focusing on the triad formed by Asp297, Arg299, and 7-propionate. Colored and green sticks represent the structures of the reconstituted and wild-type (2CPP) proteins, respectively. The pink and green spheres represent waters in the structures of the reconstituted and wild-type (2CPP) proteins, respectively.

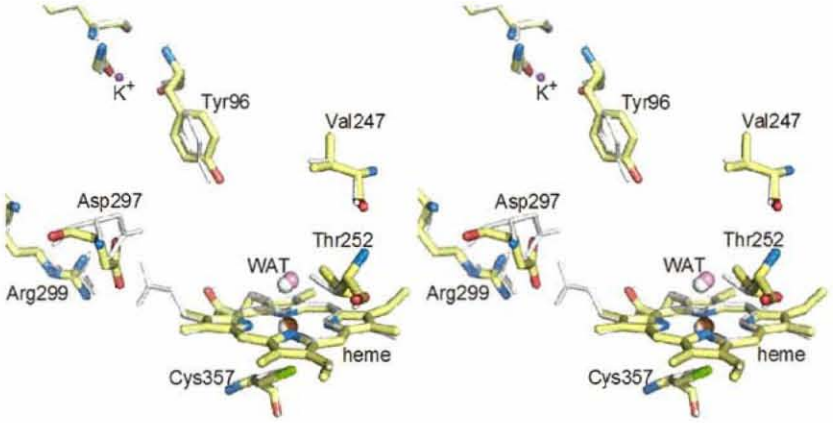

Figure 4-17. Superimposed structure (stereo image) at the active site. Colored and white sticks represent the structures of the reconstituted and wild-type (1PHC: camphor-free structure) proteins, respectively. For clarity, water molecules except the heme-bound water are omitted.

The first electron transfer from reduced Pdx to ferric P450cam. To investigate the effect of the heme iron spin state on electron transfer reaction, the author measured the first electron transfer rate from reduced Pdx to ferric P450cam in the single turnover reaction. The first electron transfer rate can be evaluated by monitoring the formation rate of ferrous CO complex of P450cam after the rapid mixing of ferric P450cam and reduced Pdx under CO atmosphere [24]. The apparent rate constants (k_{obs1}) at the various concentrations of Pdx was estimated from the time course of absorbance change at 446 nm, which is the Soret maximum of ferrous CO ligated P450cam, fitted to a single exponential curve. Next, apparent first-order rate constants were plotted as a function of reduced Pdx concentration (Figure 4-18). The values of the Michaelis constant (K_{m1}) and the first electron transfer rate (k_{ET1}) were estimated by fitting the k_{obs1} values using eq. 3-3. The values obtained in the first electron transfer reaction are summarized in Table 4-9.

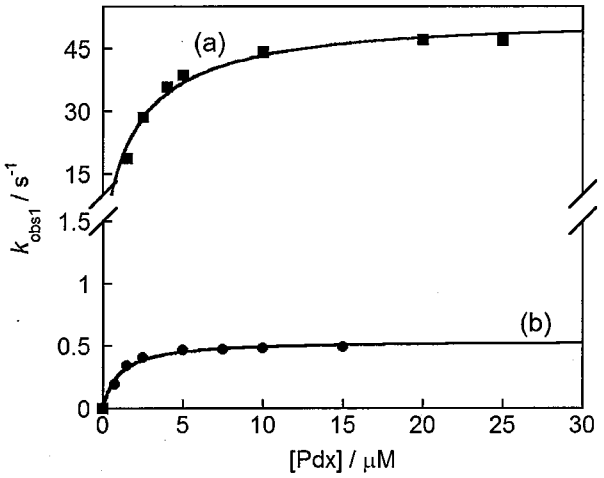

Figure 4-18. Observed first-order rates (k_{obs1}) for the ferric form reduction of (a) the wild-type (closed square) and (b) $rP450_{cam}$(2) (closed circle) by reduced putidaredoxin versus concentration of reduced putidaredoxin in 50 mM KPi (pH 7.4) containing 100 mM KCl and 1 mM *d*-camphor at 20 °C.

Table 4-9. Kinetic and equilibrium parameters of the first electron transfer reaction[a]

Protein	k_{ET1} (s^{-1})	K_{m1} (μM)
rP450cam(**2**)	0.54 ± 0.017	1.0 ± 0.15
wt-P450cam	53 ± 1.6	2.1 ± 0.25

[a] pH 7.4 (50 mM KPi buffer containing 100 mM KCl and 1 mM *d*-camphor) at 20 °C.

NADH oxidation and product analysis. The rate constant of the NADH-driven hydroxylation of *d*-camphor is one-fiftieth that determined for the wild-type protein (Figure 4-20, Table 4-10). In contrast, the product analysis suggests that the hydroxylation of *d*-camphor only occurs at the C-5 position as seen in the wild-type protein (Figure 4-19). The reaction remains well coupled with oxidation of NADH as evidenced by the observation that 87 ± 2 % of NADH was oxidized to produce the product.

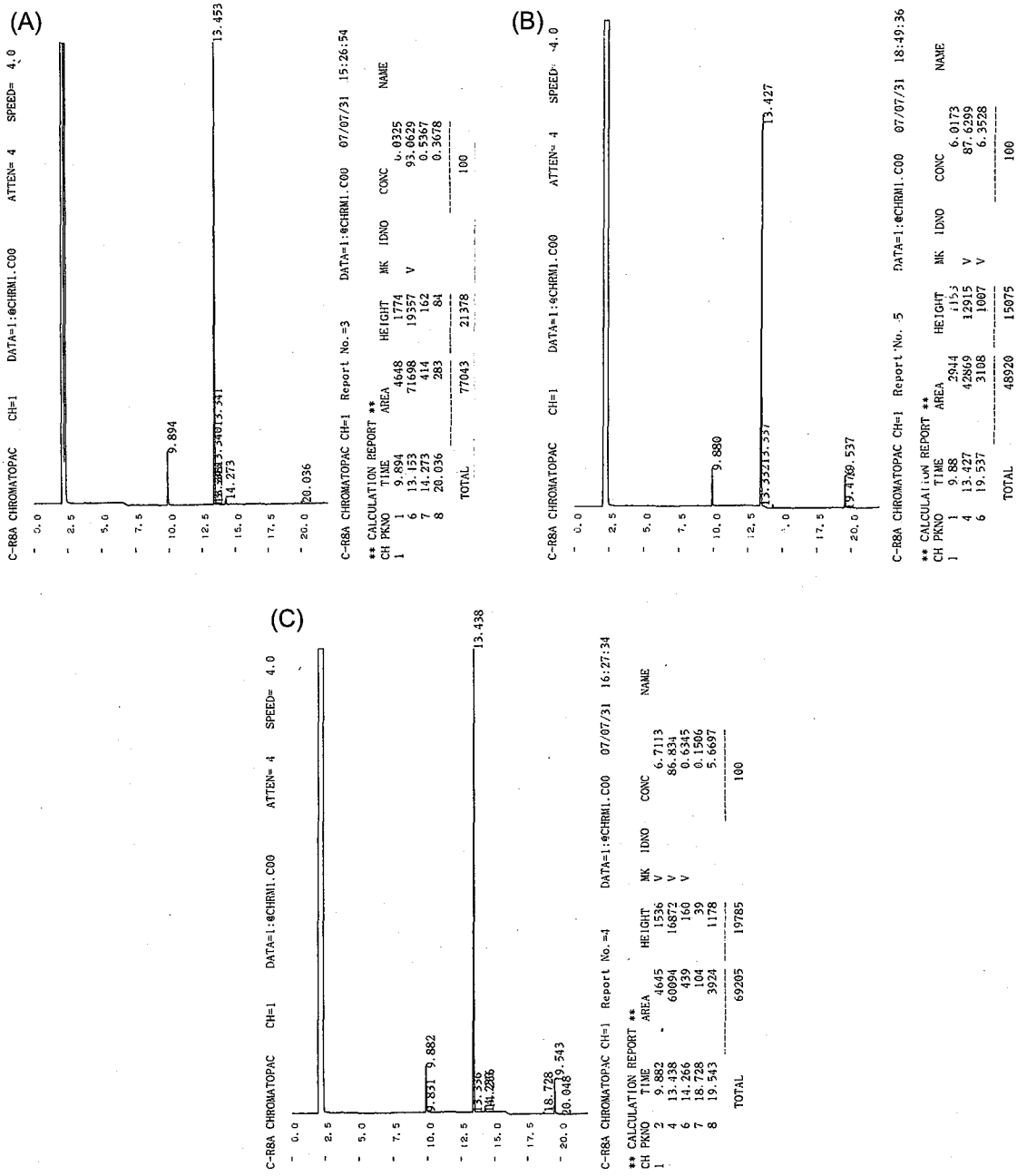

Figure 4-19. The transformation of *d*-camphor as monitored by GC. Under the conditions described in experimental section, the retention times were 9.9 min for benzyl alcohol, 13.4 min for *d*-camphor, and 19.5 min for 5-*exo*-hydroxycamphor. (A) Chromatogram obtained after the incubation of 14 μM Pdx, 0.12 μM PdR, 600 units/mL catalase, 200 units/mL SOD and 100 μM NADH in 50 mM KPi (pH 7.4) containing 100 mM KCl and 1 mM *d*-camphor at 20 °C for 15 min, (B) Chromatogram obtained after the incubation in the same conditions of (A) with 0.042 μM wild-type P450cam for 2 min, (C) Chromatogram obtained after the incubation in the same conditions of (A) with 0.96 μM rP450cam(**2**) for 3 min.

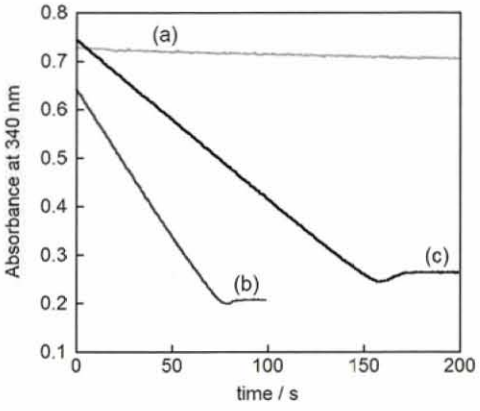

Figure 4-20. The NADH oxidation by the wild-type and rP450cam(**2**) in a reconstituted system. (a) The trace obtained after the incubation of 14 μM Pdx, 0.12 μM PdR, 600 units/mL catalase, 200 units/mL SOD and 100 μM NADH in 50 mM KPi (pH 7.4) containing 100 mM KCl and 1 mM *d*-camphor at 20 °C, (b) The trace obtained after the incubation in the same conditions of (a) with 0.042 μM wild-type P450cam, (c) The trace obtained after the incubation in the same conditions of (a) with 0.96 μM rP450cam(**2**).

Table 4-10. NADH oxidation rate and coupling ratio[a]

protein	NADH oxidation rate ($\mu M\ min^{-1}(\mu M\ enzyme)^{-1}$)	coupling ratio[b] (%)
rP450cam(**2**)	27 ± 2	87 ± 2
wt-P450cam	(1.35 ± 0.05) × 10^3	100

[a] pH 7.4 (50 mM KPi buffer containing 100 mM KCl and 1 mM *d*-camphor with 14 μM Pdx, 0.12 μM PdR, 600 units/mL catalase, 200 units/mL SOD) at 20 °C. [b] Ratio between the hydroxylated product (5-*exo*-hydroxycamphor) and NADH oxidized.

Energy minimization calculation. The conformational changes of 7-propionate and Arg299 owing to the conformational change of Asp297 to the conformation in the reconstituted protein structure were predicted by the energy minimization calculation by the program of X-PLOR [18] as shown in Figure 4-21. The conformational change of Asp297 induced weakening of the interaction between heme-7-propionate and Arg299.

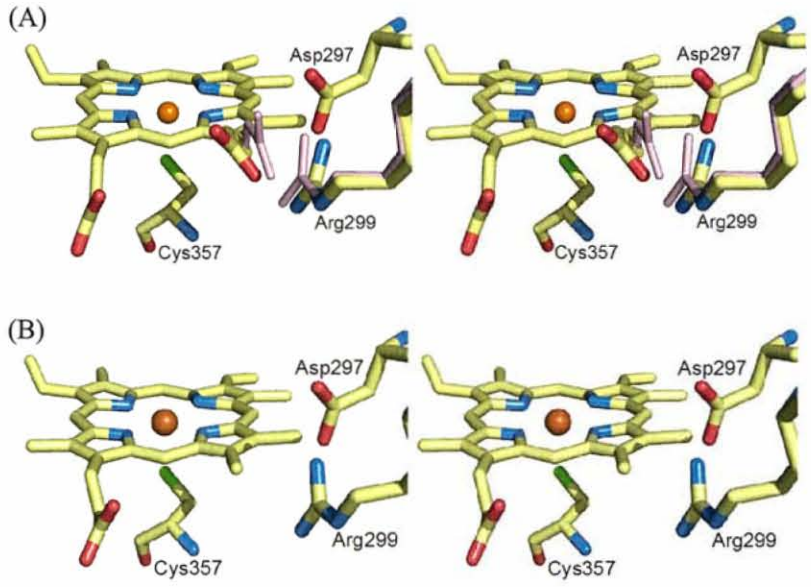

Figure 4-21. Prediction of the conformational changes of 7-propionate and Arg299 owing to the conformational change of Asp297 to the conformation in the reconstituted protein structure by X-PLOR analysis. All panels are stereo pair representation. (A) The pink structure shows the wild-type protein structure (2CPP) and the colored structure denotes the predicted structure by X-PLOR analysis. (B) The reconstituted protein structure (2Z97).

4-4. Discussion

Reconstitution of P450cam with the one-legged heme 2. The insertion of the one-legged heme into apoP450cam was carried out in the presence of 20 mM dithiothreitol (DTT) and 0.4 mM *d*-camphor in a glove box (< 1 ppm O_2) over 2 days at room temperature [25]. The reconstitution was confirmed by ESI-TOF mass spectrum which showed peak at 47102.8 (the calculated mass number is 47101.34). Purified P450cam exhibited the ferrous CO-bound P450cam spectrum with the Soret peak at the characteristic wavelength at 446 nm (Figure 4-4(D)), indicating that the thiolate of the Cys357 was ligated to the heme iron of the one-legged heme as seen in the wild-type protein. In contrast, the UV–vis spectrum of the reconstituted ferric P450cam is comparable with that observed for the typical low-spin ferric P450cam species with maxima at wavelengths of 417, 540 and 570 nm in the presence of 1 mM *d*-camphor (Figure 4-4(A)), whereas the wild-type protein usually has a spectrum characteristic of the high-spin species with maxima at 391, 512, and 646 nm under the same conditions. Thus, the replacement of the 7-propionate side chain with the methyl group prevents conversion of the low-spin species to the high-spin species in spite of the addition of *d*-camphor. The content of high-spin state in the presence of 1 mM *d*-camphor and 100 mM KCl is estimated to be 26% based on deconvolution of the Soret band region using the UV–vis spectra of the camphor-free reconstituted protein and camphor-bound wild-type protein. Under the same conditions, the spectrum of the wild-type protein shows the complete 5-coordinated high-spin heme species, although the low K^+ concentration has an influence on the substrate binding affinity [19(a)]. The high-frequency resonance Raman spectrum of the reconstituted ferric P450cam also exhibits two evident ν_3 bands at 1503 and 1489 cm^{-1} which are derived from the low-spin and high-spin species, respectively (Figure 4-5) [21]. From these results, the dissociation constant of *d*-camphor is estimated to be 3 mM at pH 7.4, 20 °C, indicating that the *d*-camphor affinity is dramatically reduced by approximately three orders of magnitude upon removal of the 7-propionate side chain. Thus, it is found that the 7-propionate side chain facilitates the high affinity of cytochrome P450cam for its substrate, *d*-camphor.

Enzymatic Activities. Although the affinity of the one-legged heme-reconstituted P450cam, rP450cam(**2**), for reduced putidaredoxin (Pdx) is essentially the same as that of wild-type P450cam (Table 4-9), the process of electron transfer from reduced Pdx to ferric reconstituted P450cam is much slower (Figure 4-18, Table 4-9). As a result of this dramatically slowed first electron transfer in the reconstituted protein, the rate constant of the NADH-driven hydroxylation of *d*-camphor is one-fiftieth that determined for the wild-type protein. These findings are supported by the spectroscopic data that indicate the predominant presence of the less reactive low-spin species in the reconstituted protein. In contrast, the product analysis suggests that the hydroxylation of *d*-camphor only occurs at the C-5 position as seen in the wild-type protein. The reaction remains well coupled with oxidation of NADH as evidenced by the observation that 87 ± 2 % of NADH was oxidized to produce the product. These results indicate that the removal of the 7-propionate side chain exerts an influence on the electron transfer step occurring subsequent to the conversion of low-spin heme to high-spin heme upon binding of *d*-camphor.

Crystal structure of the reconstituted P450cam with one-legged heme. The X-ray structure of the ferric rP450cam(**2**) at a resolution of 1.8 Å reveals that the asymmetric one-legged heme is incorporated into the heme pocket in the same plane and in essentially the same conformation as the heme of the wild-type protein (Figure 4-14(A)). These observations suggest that the lack of the 7-propionate side chain does not exert an influence on the structure and electronic properties of the heme in agreement with the spectroscopic data of P450cam. The polypeptide Cα atoms of both proteins are superimposable with a root-mean-square deviation of 0.507 Å. One notable difference is observed for Asp297, which is evidently deviated from its counterpart in the native structure. In addition, *d*-camphor binds to the substrate binding site with nearly the same conformation with that of the wild-type protein forming a characteristic hydrogen bond with Tyr96 and the C-5 atom faces toward the heme iron, consistent with the regiospecific hydroxylation of *d*-camphor. However, *d*-camphor does not fully bind in the substrate binding site (vide infra).

The $F_o - F_c$ map focusing on the substrate binding site clearly shows electron densities that fit to a camphor molecule and two water molecules with occupancies of 0.25 and 0.75, respectively (Figure 4-14(B)). This indicates coexistence of two substrate binding site structures; the camphor-bound form and the camphor-free water-bound structure (their protein structures are crystallographically indistinguishable to each other). In the *d*-camphor-free structure, at least two distinct water molecules are located within the substrate binding site; WAT1028 is coordinated to the heme iron at a distance of 2.54 Å, while the other water molecule, WAT1033, is located within a hydrogen-bonding distance from WAT1028 (Figure 4-14(B) and Figure 4-15). These crystal data also indicate that the lack of the 7-propionate side chain obviously decreases the substrate affinity of the protein. It is also supported the fact that the occupancies depend on the duration of soaking of the crystals in *d*-camphor saturated solution (data not shown here).

Relative to the camphor-bound and camphor-free forms of the wild-type protein, two additional water molecules (WAT1030 and 1031) are identified near Tyr96 and Asp297 of the reconstituted P450cam. Furthermore, a single water molecule (WAT1117) occupies the position of the 7-propionate carboxylate. As a result, a unique array of water molecules extending from the Tyr96 residue to the outside of the protein is observed in the crystal structure (Figure 4-14(C)). This water array appears to prevent the exclusion of the inside water molecules from the substrate binding site, thereby decreasing the *d*-camphor binding affinity of the reconstituted P450cam. In the reconstituted protein, it is noted that the Asp297 residue is remarkably flipped and its side chain Oγ1 and Oγ2 atoms are located at the hydrogen bonding distance from WAT1030 and WAT1117 (Figure 4-16). This structural evidence suggests that the Asp297 residue may be capable of undergoing a large conformational change in the protein matrix and influenced to deviate from its native position by the influence of the water molecule array.

Mechanism of the substrate-induced P450 activation. In the wild-type P450cam, the water molecules in the substrate binding site is efficiently expelled to the outside of the protein upon binding of *d*-camphor. The X-ray structure of the rP450cam(**2**) suggests the following mechanism for the water exclusion in the wild-type protein (Figure 4-22): (i) The 7-propionate side chain forms a triad with Arg299 and Asp297 residues by the hydrogen-bonding network. The triad structure prevents the water exclusion and inclusion (closed gate). (ii) Upon binding of the *d*-camphor, the water molecules in the active site shift toward Tyr96 located over the heme edge and the 7-propionate side chain and partly form a water array similar to that observed in the crystal structure (Figure 4-14(C)). The transiently formed water array brings about the conformational change of Asp297 by thermodynamically favored interaction between Asp297 and water. The Asp297 deviation disrupts the triad including the 7-propionate–Arg299 salt-bridge (gate opening). (iii) The water molecules then flow out to the bulk solvent through the opened gate due to the partially malfunctioned triad. (iv) After the exclusion of the water molecules, the carboxylate group of Asp297 flips back to the initial position, thereby re-forming the triad salt bridge (gate closing). Conversely, the conformational change of Asp297 which assists in displacement of the water molecules triggers the opening of the gate.

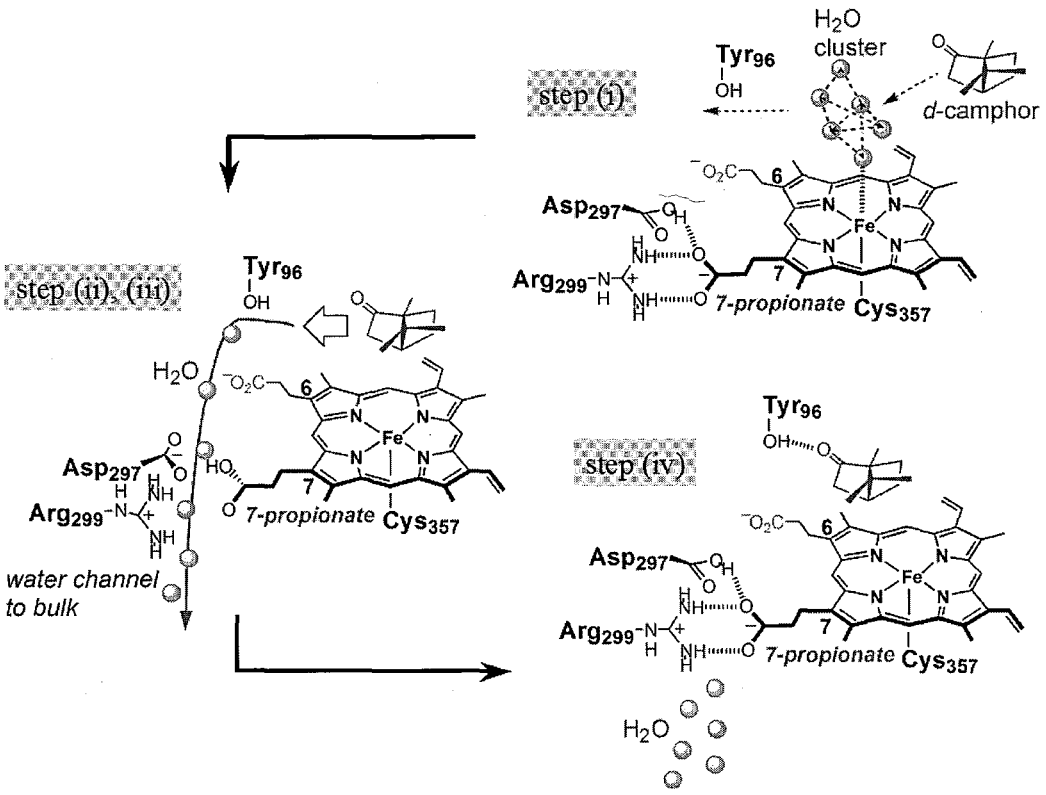

Figure 4-22. Proposed mechanism of the substrate-induced P450cam activation.

4-5. Summary

The present findings strongly suggest that the 7-propionate side chain functions as a water gate to exclude waters upon binding of the substrate and prevent water inclusion to facilitate the high *d*-camphor binding affinity in P450cam. Thus, the 7-propionate side chain is essential not only to anchoring of the heme to the protein matrix but also to the formation of the active species of the high-spin heme.

References

1. Gunsalus, I. C., Meeks, J. R., Lipscomb, J. D., Debrunner, P., and Munck, E. (1974) *in Molecular Mechanism of Oxygen Activation* (Hayaishi, O., Eds.) pp 559–613, Academic Press, New York.
2. Goldfarb, D., Bernardo, M., Thomann, H., Kroneck, P. M. H., and Ullrich, V. (1996) Study of water binding to low-spin Fe(III) in cytochrome P450 by pulse ENDOR and four-pulse ESEEM spectroscopies, *J. Am. Chem. Soc. 118*, 2686–2693.
3. Poulos, T. L., Finzel, B. C., and Howard, A. J. (1986) Crystal structure of substrate-free *Pseudomonas putida* cytochrome P-450, *Biochemistry 25*, 5314–5322.
4. Poulos, T. L., Finzel, B. C., and Howard, A. J. (1987) High-resolution crystal structure of cytochrome P450cam, *J. Mol. Biol. 195*, 687–700.
5. Schlichting, I., Berendzen, J., Chu, K., Stock, A. M., Maves, S. A., Benson, D. E., Sweet, R. M., Ringe, D., Petsko, G. A., and Sligar, S. G. (2000) The catalytic pathway of cytochrome P450cam at atomic resolution, *Science 287*, 1615–1622.
6. (a) Lüdemann, S. K., Lounnas, V., and Wade, R. C. (2000) How do substrates enter and products exit the buried active site of cytochrome P450cam? 1. Random expulsion molecular dynamics investigation of ligand access channels and mechanisms, *J. Mol. Biol. 303*, 797–811. (b) Lüdemann, S. K., Lounnas, V., and Wade, R. C. (2000) How do substrates enter and products exit the buried active site of cytochrome P450cam? 2. Steered molecular dynamics and adiabatic mapping of substrate pathways, *J. Mol. Biol. 303*, 813–830. (c) Dunn, A. R., Dmochowski, I. J., Bilwes, A. M., Gray, H. B., and Crane, B. R. (2001) Probing the open state of cytochrome P450cam with ruthenium-linker substrates, *Proc. Natl. Acad. Sci. USA 98*, 12420–12425. (d) Hays, A.-M. A., Dunn, A. R., Chiu, R., Gray, H. B., Stout, C. D., and Goodin, D. B. (2004) Conformational states of cytochrome P450cam revealed by trapping of synthetic molecular wires, *J. Mol. Biol. 344*, 455–469. (e) Wade, R. C., Winn, P. J., Schlichting, I., and Sudarko (2004) A survey of active site access channels in cytochromes P450, *J. Inorg. Biochem. 98*, 1175–1182.
7. Oprea, T. I., Hummer, G., and García, A. E. (1997) Identification of a functional water channel in cytochrome P450 enzymes, *Proc. Natl. Acad. Sci. USA 94*, 2133–2138.
8. Schneider, S., Marles-Wright, J., Sharp, K. H., Paoli, M. (2007) Diversity and conservation of interactions for binding heme in b-type heme protein, *Nat. Prod. Rep. 24*, 621–630.
9. Smith, K. M., and Craig, G. W. (1983) Porphyrin synthesis through tripyrrins: An alternate approach, *J. Org. Chem. 48*, 4302–4306.
10. Imai, M., Shimada, H., Watanabe, Y., Matsushima-Hibiya, Y., Makino, R., Koga, H., Horiuchi, T., and Ishimura, Y. (1989) Uncoupling of the cytochrome P-450cam monooxygenase reaction by a single mutation, threonine-252 to alanine or valine: A possible role of the hydroxy animo acid in oxygen activation, *Proc. Natl. Acad. Sci. USA 86*, 7823–7827.
11. Otwinowsky, A., and Minor, W. (1997) Processing of X-ray diffraction data collected in oscillation mode, *Methods Enzymol. 276*, 307–326.
12. Vagin, A., and Teplyakov, A. (1997) *MOLREP*: an automated program for molecular replacement, *J. Appl. Cryst. 30*, 1022–1025.

13. Collaborative Computational Project, Number 4 (1994) The CCP4 Suite: Programs for Protein Crystallography, *Acta Cryst. D50*, 760–763.
14. Brünger, A. T. (1992) Free R value: A novel statistical quantity for assessing the accuracy of crystal structures, *Nature 355*, 472–475.
15. Emsley, P., and Cowtan, K. (2004) *Coot*: Model-building tools for molecular graphics, *Acta Cryst. D60*, 2126–2132.
16. (a) Murshudov, G., Vagin, A., and Dodson, E. (2004) in the Refinement of Protein structures, Proceedings of Daresbury Study Weekend. (b) Murshudov, G. N., Vagin, A. A. and Dodson, E. J. (1997) Refinement of macromolecular structures by the maximum-likelihood method, *Acta Cryst. D53*, 240–255. (c) Pannu, N. S., Murshudov, G. N., Dodson, E. J., and Read, R. J. (1998) Incorporation of prior phase information strengthens maximum-likelihood structure refinement, *Acta Cryst. D54*, 1285–1294. (d) Murshudov, G. N., Vagin, A. A., Lebedev, A., Wilson, K. S., and Dodson, E. J. (1999) Efficient anisotropic refinement of macromolecular structures using FFT, *Acta Cryst. D55*, 247–255. (e) Winn, M. D., Isupov, M. N., and Murshudov, G. N. (2001) Use of TLS parameters to model anisotropic displacements in macromolecular refinement, *Acta Cryst. D57*, 122–133.
17. DeLano, W. L. (2002) *The PyMOL Molecular Graphics System*, DeLano Scientific, San Carlos, CA.
18. (a) Brünger, A. T. (1992) X-PLOR, Version 3.1: A system for x-ray crystallography and NMR (Yale University Press, New Haven) (b) Shimokata, K., Katayama, Y., Murayama, H., Suematsu, M., Tsukihara, T., Muramoto, K., Aoyama, H., Yoshikawa, S., and Shimada, H. (2007) The proton pumping pathway of bovine heart cytochrome *c* oxidase, *Proc. Natl. Acad. Sci USA 104*, 4200–4205.
19 (a) Westlake, A. C. G., Harford-Cross, C. F., Donovan, J., and Wong, L.-L. (1999) Mutations of glutamate-84 at the putative potassium-binding site affect camphor binding and oxidation by cytochrome $P450_{cam}$, *Eur. J. Biochem. 265*, 929–935. (b) Peterson, J. A. (1971) Camphor binding by *Pseudomonas putida* cytochrome P-450, *Arch. Biochem. Biophys. 144*, 678–693.
20. Gunsalus, I. C., and Wagner, G. C. (1978) Bacterial $P\text{-}450_{cam}$ methylene monooxygenase components: cytochrome *m*, putidaredoxin, and putidaredoxin reductase, *Methods Enzymol. 52*, 166–188.
21. Wells, A. V., Li, P., Champion, P. M., Martinis, S. A., and Sligar, S. G. (1992) Resonance Raman investigations of *Escherichia coli*-expressed *Pseudomonas putida* cytochrome P450 and P420, *Biochemistry 31*, 4384–4393.
22. Kincaid, J. R. (2000) in *The Porphyrin Handbook* (Kadish, K. M., Smith, K., and Guilard, K. S., Eds.) Vol. 7, pp 225–291, Academic Press, San Diego.
23. (a) Mouro, C., Bondon, A., Jung, C., De Certaines, J. D., and Simonneaux, G. (2000) Assignment of heme methyl ^{1}H-NMR resonances of high-spin and low-spin ferric complexes of cytochrome P450cam using one-dimensional and two-dimensional paramagnetic signals enhancement (PASE) magnetization transfer experiments, *Eur. J. Biochem. 267*, 216–221. (b) Banci, L.; Bertini, I.; Marconi, S.; Pierattelli, R.; Sligar, S. G. (1994) Cytochrome P450 and aromatic bases: A ^{1}H NMR study, *J. Am. Chem. Soc. 116*, 4866–4873. (c) Wakasugi, K.; Ishimori, K.; Morishima, I. (1996) NMR studies of recombinant cytochrome P450cam mutants, *Biochimie 78*, 763–770.
24. Hintz, M. J., and Peterson, J. A. (1981) The kinetics of reduction of cytochrome $P\text{-}450_{cam}$ by reduced

putidaredoxin, *J. Biol. Chem. 256*, 6721–6728.

25. Wagner, G. C., Perez, M., Toscano, W. A., Jr., and Gunsalus, I. C. (1981) Apoprotein formation and heme reconstitution of cytochrome P-450_{cam}, *J. Biol. Chem. 256*, 6262–6265.

Chapter 5

Conclusion

Many hemoproteins have protoheme IX as a prosthetic group. The heme bears two unique propionate side chains at 6- and 7-positions of β-pyrrolic carbons. According to a series of 3D structures of hemoproteins, the propionate side chains interact with polar amino acid residues in the protein matrix, so it has been known that the side chains play a role on the fixation of the prosthetic group in the heme pocket. However, the author has recently thought that the roles of the two propionate side chains are not only the fixation of heme but also the direct contribution to the regulation of the hemoprotein function. Based on this viewpoint, the author has prepared one-legged hemes, 6-depropionated-6-methylated protoheme IX **1** and 7-depropionated-7-methylated protoheme IX **2**. Furthermore, the hemins were incorporated into apohemoprotein by conventional method to understand each role of the defective propionate side chain.

In the case of sperm whale myoglobin, 6- and 7-propionate side chains interact with Arg45 and Ser92 via hydrogen bonding, respectively. The reconstituted myoglobins with the two monodepropionated hemins, rMb(**1**) and rMb(**2**), were characterized by UV–vis, ESI-MS, ^{1}H NMR spectroscopic methods. It has been revealed that two heme-propionate side chains contribute a factor of 10–15% to the overall binding affinity of the native hemin for the protein matrix of myoglobin. Furthermore, it was found that the one-legged hemins were maintained stably in the protein matrix as in the case of native hemin **3** under a physiological pH. The dissociation of O_2 from oxymyoglobin with **1** was accelerated about three times as that of the oxymyoglobin with the native heme. Furthermore, the autoxidation rate of oxymyoglobin with **1** was approximately six times faster than that of oxymyoglobin with native heme. These results indicate that the 6-propionate side chain plays an important role on the stabilization of oxymyoglobin. In contrast, the acceleration of the CO binding rate, deceleration of the CO dissociation, and strengthening of the Fe–His93 bond were observed for myoglobin with **2**, suggesting that the 7-propionate side chain regulates the His93–heme iron coordination in the proximal site.

Cytochrome P450cam (P450cam) from *Pseudomonas putida* is a heme-containing monooxygenase that catalyzes the regio- and stereo-specific hydroxylation of *d*-camphor by using molecular oxygen and accepting two electrons from NADH. The 3D structure of P450cam suggests that the two propionate side chains will play a crucial role on the regulation of the initial stage of the catalytic reaction. The interaction between 7-propionate side chain and Arg299 seems to act as a gate of aqueduct, and the 6-propionate side chain is linked with Arg112 which is a binding site for putidaredoxin as an electron donor protein. The author has prepared two reconstituted P450cams with **1** and **2**, respectively. The spectroscopic data and the enzymatic activities reveal that the removal of the 6-propionate has no clear influence on the enzyme property. The rate of electron transfer from putidaredoxin (Pdx), a natural redox partner, to P450cam was not significantly changed, whereas, the removal of the 6-propionate decreased the affinity of Pdx by 3.5-fold supporting the proposed role of Arg112 as the essential constituent of the Pdx binding site. Resonance Raman experiments indicate that removal of the 6-propionate weakens the Fe–S

bond strength. The X-ray structure of the reconstituted protein at 1.55 Å resolution is highly superimposable with that of the wild-type protein, whereas the thiolate of the Cys357 heme ligand in the reconstituted protein is visible from the protein surface owing to the lack of the 6-propionate. Lengthening of the Fe–S bond and the water accessibility could facilitate protonation of thiolate anion to thiol, explaining the observed formation of the inactive P420 species under the mild conditions. Therefore, the *d*-camphor hydroxylation reaction requires a 6-propionate–protein matrix interaction to maintain an active P450 species.

Water must be expelled from the active site of monooxygenase cytochrome P450cam to allow the substrate (*d*-camphor) binding induced enzyme activation. To understand this mechanism, the author reconstituted the enzyme with an artificial one-legged heme **2** where the heme-7-propionate is replaced with a methyl group. Although the reconstituted enzyme exhibited a normal ferrous-CO UV–vis spectrum, the monooxygenase activity decreased dramatically due to slow electron transfer from reduced putidaredoxin to the ferric enzyme. The ferric form of the reconstituted enzyme was found to predominantly remain in the 6-coordinated low-spin state in the presence of *d*-camphor, because *d*-camphor binding affinity decreased by a thousand-fold relative to that of the wild-type enzyme. X-ray structural analysis of the reconstituted enzyme at a 1.8 Å resolution revealed two structures, *d*-camphor-bound and unbound structures, with a novel water array extending from the active site to bulk water through the position occupied by the 7-propionate with a minimum change in the protein structure except for Asp297, which undergoes significant conformational changes to interact with the water array via hydrogen bond. The water array appears to prevent displacement of waters bound to the *d*-camphor binding site, thereby inhibiting *d*-camphor binding. The present findings suggests a water exclusion mechanism in the wild-type enzyme whereby 7-propionate side chain forms a gate with Arg299 and Asp297 residues through which water is expelled upon disruption of 7-propionate-Arg299 bond (gate opening) by transient flipping of Asp297 side chain driven by water displacement upon *d*-camphor binding.

It has been proved that the roles of the two propionate side chains are not only the fixation of heme but also the direct contribution to the regulation of the hemoprotein (myoglobin and cytochrome P450cam) function by the author's research. It is possible to apply the method utilizing one-legged hemes to elucidate roles of each heme propionate side chains to other hemoproteins than myoglobin and cytochrome P450cam. Furthermore, it is expected that the relationship between heme-protein interactions and the functions of hemoproteins will be clarified by this method.

Publications for this Thesis

1. Chemical Properties of Sperm Whale Myoglobins Reconstituted with Monopropionate Hemins
   Takashi Hayashi, Tomoyuki Nakagawa, Katsuyoshi Harada, Takashi Matsuo, Yutaka Hitomi, and Yoshio Hisaeda
   Chem. Lett. **2004**, *33*, 1512–1513.
2. Structure and Ligand Binding Properties of Myoglobins Reconstituted with Monodepropionated Heme: Functional Role of Each Heme Propionate Side Chain
   Katsuyoshi Harada, Masatomo Makino, Hiroshi Sugimoto, Shun Hirota, Takashi Matsuo, Yoshitsugu Shiro, Yoshio Hisaeda, and Takashi Hayashi
   Biochemistry **2007**, *46*, 9406–9416.
3. Evaluation of the Functional Role of the Heme-6-propionate Side Chain in Cytochrome P450cam
   Katsuyoshi Harada, Keisuke Sakurai, Kenichiro Ikemura, Takashi Ogura, Shun Hirota, Hideo Shimada, and Takashi Hayashi
   J. Am. Chem. Soc. **2008**, *130*, 432–433.
4. Heme-7-Propionate Side Chain is a Water Gate Essential to Substrate-Induced Cytochrome P450cam Activation
   Takashi Hayashi, Katsuyoshi Harada, Keisuke Sakurai, Shun Hirota, and Hideo Shimada
   submitted for publications

Other Publications

1. Physicochemical properties of reconstituted hemoproteins having monopropionated hemin
   Katsuyoshi Harada and Takashi Hayashi
   J. Porphyrins Phthalocyanines **2006**, *10*, 656.
2. Role of Heme-Propionate Side Chains in Myoglobin Function
   Takashi Hayashi, Takashi Matsuo, Katsuyoshi Harada, Yoshio Hisaeda, Shun Hirota, and Noriaki Funasaki
   J. Inorg. Biochem. **2003**, *96*, 50.
3. Pathway of Information Transmission from Heme to Protein upon Ligand Binding/Dissociation in Myoglobin Revealed by UV Resonance Raman Spectroscopy
   Ying Gao, Samir F. El-Mashtoly, Biswajit Pal, Takashi Hayashi, Katsuyoshi Harada, and Teizo Kitagawa
   J. Biol. Chem. **2006**, *281*, 24637–24646.
4. Time-resolved Raman evidence for energy 'funneling' through propionate side chains in heme 'cooling' upon photolysis of carbonmonoxy myoglobin
   Ying Gao. Mai Koyama, Samir F. El-Mashtoly, Takashi Hayashi, Katsuyoshi Harada, Yasuhisa Mizutani, and Teizo Kitagawa
   Chem. Phys. Lett. **2006**, *429*, 239–243.

Acknowledgments

The study presented in this thesis has been carried out at the Department of Chemistry and Biochemistry, Graduate School of Engineering, Kyushu University from April 2002 to March 2005 and at the Department of Applied Chemistry, Graduate School of Engineering, Osaka University from April 2005 to December 2007. The author would like to express my deep gratitude to the supervisor, Professor Dr. Takashi Hayashi, for his helpful suggestions, constant discussions and warm encouragement throughout this research. The author would like to express my sincere gratitude to Professor Dr. Yoshio Hisaeda, Department of Chemistry and Biochemistry, Graduate School of Engineering, Kyushu University, for his appropriate guidance, valuable suggestions, and warm encouragement. The author would like to deeply thank Dr. Takashi Matsuo for his valuable suggestions, discussions and the support of smooth proceeding of this research. The author would like to deeply thank Dr. Hideaki Sato, Department of Medical Biochemistry, Kurume University School of Medicine, for his valuable suggestions, discussions, warm encouragement and the support of smooth proceeding of this research. The author would like to express my gratitude to Dr. Hisashi Shimakoshi, Department of Chemistry and Biochemistry, Graduate School of Engineering, Kyushu University, for his helpful suggestions.

The author also acknowledges Professor Dr. Susumu Kuwabata and Professor Dr. Hiroshi Uyama for reviewing this thesis and valuable discussions.

The author expresses great gratitude to Professor Dr. Hideo Shimada, Department of Biochemistry, School of Medicine, Keio University, for his helpful suggestions and discussions. The author expresses great gratitude to Professor Dr. Tomitake Tsukihara, Institute for Protein Research, Osaka University, for his valuable suggestions and help in carrying out the X-ray structure analysis of cytochrome P450cam. The author also expresses great gratitude to Mr. Keisuke Sakurai, Institute for Protein Research, Osaka University, for analysis of the crystal structures of cytochrome P450cam and valuable discussions. The author expresses great gratitude to Professor Dr. Yoshitsugu Shiro and Dr. Hiroshi Sugimoto, RIKEN SPring-8 Center, Harima Institute, and Mr. Masatomo Makino, Graduate School of Life Science, University Hyogo, for analysis of the crystal structures of myoglobin. The author expresses great gratitude to Professor Dr. Shun Hirota, Graduate School of Materials Science, Nara Institute of Science and Technology, and Professor Dr. Takashi Ogura and Mr. Kenichiro Ikemura, Graduate School of Life Science, University Hyogo, for measurements of resonance Raman spectra and valuable discussion. The author also thanks Professor Dr. Teizo Kitagawa for the use of the resonance Raman equipment at the Okazaki Institute for Integrative Bioscience. The author expresses great gratitude to Professor Dr. Yasuhiko Yamamoto, Mr. Shin-ichi J. Takayama, and Mr. Satoshi Nagao, Department of Chemistry, University of Tsukuba, for measurements of ^{1}H NMR spectra of P450cam and valuable discussion.

The author would like to thank Mr. Takahiro Masuko, Department of Chemistry and Biochemistry, Graduate School of Engineering, Kyushu University, for his kind advices. The author would like to deeply thank Dr. Hiroaki Kitagishi for his valuable suggestions, discussions and warm encouragement.

The author would like to thank Professor Dr. Araki Masuyama, Osaka Institute of Technology, and

Professor Dr. Manabu Abe, Department of Chemistry, Graduate School of Science, Hiroshima University, for their helpful discussions from various points of view.

Acknowledgment is also made to all members of Professor Dr. Yoshio Hisaeda's group and Professor Dr. Takashi Hayashi's group for their encouragements and friendship in the laboratory.

The author would like to express great gratitude to his parents and family for their constant assistance and warm encouragement.

Finally, the author is grateful for the financial support by the Japan Society of the Promotion of Science (JSPS) for 3 years.

Katsuyoshi Harada

January 2008